The history, hydraulics, and geomorphic impact of outburst floods in the eastern Himalaya

Michael D. Turzewski

A dissertation

submitted in partial fulfillment of the

requirements for the degree of

Doctor of Philosophy

University of Washington

2019

Reading Committee:

Katharine W. Huntington, Chair

Alison R. Duvall

David R. Montgomery

Program Authorized to Offer Degree:

Earth and Space Sciences

University of Washington

Abstract

The history, hydraulics, and geomorphic impact of outburst floods in the eastern Himalaya

Michael D. Turzewski

Chair of the Supervisory Committee:
Dr. Katharine W. Huntington
Earth and Space Sciences

Outburst floods have shaped many landscapes on Earth and represent a significant geologic hazard, but they are relatively infrequent, and we must rely on the sedimentary record to study the most extreme events that have occurred. The eastern Himalaya has a record of various magnitude outburst flood events, including landslide-dam outburst floods (>10^5 m^3/s) and ancient glacial-outburst megafloods (>10^6 m^3/s) that have done substantial amounts of geomorphic work on the landscape throughout the Quaternary. This dissertation investigates outburst floods in the eastern Himalaya with a combination of fieldwork, remote sensing, numerical flood modeling, and geochronology to study the timing, hydraulics, and net erosional impact of these events. Numerical flood simulations of the year 2000 Yigong River outburst flood help characterize flood hazard in the Siang River valley, India, and are used to examine the relationship between outburst flood hydraulics and geomorphic change observed along the >450 km rugged flood pathway that cuts through the >2 km deep Tsangpo Gorge. Simulated outburst flood hydraulics differ from non-flood flows and show that valley topography exerts a strong control on the distribution of shear stress and the patterns of erosion and deposition produced from the flood. Zircons collected from ancient slackwater flood deposits in the region characterize the age of rocks eroded from flood source terrains in Tibet and from the Tsangpo Gorge. Statistical analyses of these data support the previous hypothesis that megafloods erode more rock from Gorge compared to smaller flows, but also show substantial variability among different megaflood deposit samples. These data suggest that megafloods rework sediments from previous events, which is a result supported by luminescence age data from megaflood deposits that influences the interpretation of detrital outburst flood samples. Radiocarbon and luminescence dating methods constrain the timing of at least 9 megaflood events over the last 42 ka, showing the potential for repeated megaflood events from glacial-lake sources in Tibet. The work presented here advances our knowledge about hydraulics during outburst floods, patterns of preferential erosion, chronology of megafloods, and processes of sediment reworking, altogether improving our understanding of the impact of extreme outburst floods in the region.

TABLE OF CONTENTS

LIST OF FIGURES

LIST OF TABLES

ACKNOWLEDGEMENTS

This dissertation would not have been possible without the support of my family, friends, and colleagues. I would like to thank several specific people that were particularly important to the development of my thesis and to my own personal growth throughout graduate school. I thank my advisor Katharine W. Huntington who has been my primary mentor as a scientist and has also supported me throughout difficult personal challenges I faced in the last several years. I thank the rest of my PhD committee, Alison, Dave, Jim, and Randy, for dedicating significant time and effort to help me develop the research in these chapters. I also thank the many colleagues who have reviewed and helped me improve my writing. I offer thanks to the Quaternary Research Center and the National Science Foundation for providing funding to pursue these research questions.
I was fortunate to develop a large network of people here at the University of Washington that have contributed to my success in graduate school including:

Karl Lang, Landon Burgener, Devin Bedard, Shelley Chestler, Sarah Schanz, Alison Duvall, Joanne Bourgeois, Jim O'Connor, David George, Julia Kelson, Kelly Hillbun, Matt Koehler, Adam Campbell, Megan Mueller, Trevor Hillebrand, Max Stevens, Jon Bapst, Jill Schleicher, Keith Hodson, Max Needle, Erik Goosmann, Camille Collett, Nick Pollack, Zorro the cat, and of course—the fastest dog in Seattle, Harper.

A very special thanks to my partner Susannah Morey who kept me sane while finishing this thesis and for the endless support from my family: Dave, Kathy, Elisa, Shelley, and Mackie.

DEDICATION

This work is dedicated to Harper Chestler.

INTRODUCTION

Outburst floods do more geomorphic work on the landscape compared to typical river flows, so they are important events to consider when studying the long-term evolution of river basins. They are also a growing risk to people living near rivers in mountainous environments with receding glaciers (e.g., Dussaillant et al., 2010, Allen et al., 2016, Carrivick and Tweed, 2016), but it can be difficult to constrain hazard from the events because they are infrequent. Occasionally, opportunities arise that enable direct observations of extreme outburst floods like the 2002 outburst flood that carved up to 7 m of vertical incision to form Canyon Lake Gorge in Texas (Lamb and Fonstad, 2010), or the 2016 glacial-lake outburst flood on the Bhotekoshi/Sunkoshi River recorded by seismic stations in central Nepal (Cook et al., 2018). However, to study the largest ancient outburst megafloods that have occurred on Earth ($>10^6$ m^3/s) like megafloods sourced from glacial-lake Missoula in Montana (Baker, 1973; O'Connor and Baker, 1992; Alho et al., 2010; Waitt, 2016), we must rely on the sedimentary record and tools like numerical flood simulation (e.g., Denlinger and O'Connell, 2009; Alho et al., 2010; Bohorquez et al., 2015; Larsen and Lamb, 2016) or zircon geochronology (Lang et al., 2013).

The extreme topography of the eastern Himalaya has been shaped by historical outburst floods (e.g. Shang et al., 2003; Evans and Delaney, 2011; Delaney and Evans, 2015) and ancient megafloods throughout the Holocene and late-Pleistocene (e.g. Montgomery et al., 2004; Korup and Montgomery, 2008; Hu et al., 2018). These events have left behind an extensive sedimentary record observed across the Yarlung-Siang-Brahmaputra River basin, including lacustrine sediments from glacially-impounded lakes in Tibet (e.g., Montgomery et al., 2004; Liu et al., 2006; Kaiser et al., 2010; Guangxiang and Qingli, 2012; Liu et al., 2015; Hu et al., 2018) and slackwater flood deposits located in the Siang River valley (Lang et al., 2013). Slackwater deposits have been analyzed to study spatial patterns of erosion to show that megaflood events preferentially erode the Tsangpo Gorge compared to historical outburst flood events and modern river flows (Lang et al., 2013). Despite this important connection between megafloods and erosion, only four megaflood deposits have been analyzed with zircon geochronology and four other megaflood deposits have been dated with luminescence dating, so the chronology and net impact of these events is still unknown. Furthermore, the mechanics of bedrock erosion during outburst floods like the year 2000 Yigong outburst flood (Shang et al., 2003; Evans and Delaney, 2011; Delaney and Evans, 2015) are poorly constrained, particularly in mountainous rivers. Relationships between outburst floods and lateral bedrock erosion are not well understood (Turowski et al., 2008; Larsen and Montgomery, 2012; Beer et al., 2017; Langston and Tucker, 2018), so numerical simulation of outburst floods in the eastern Himalaya is necessary to apply and test these theories.

This dissertation examines the history, hydraulics, and geomorphic impact of outburst floods in the eastern Himalayan syntaxis using a combination of fieldwork, remote sensing, numerical flood modeling, and geochronology. The first chapter presents insight into the mechanics of outburst floods in the region from simulations of the historical Yigong River landslide-dam outburst flood, work published in April 2019 in the *Journal of Geophysical Research – Earth Surface*. A study of sediment provenance and patterns of erosion is presented in the second chapter using statistics from a large (n>1500) zircon dataset developed from seven new slackwater megaflood deposits sampled in the Siang River valley—a manuscript in preparation that will be submitted to *Earth and Planetary Science Letters*. Finally, the third chapter constrains the chronology of megaflood events in the region using radiocarbon and luminescence techniques, a manuscript that is in preparation for submission to *Quaternary Research*.

Chapter 1. **INTEGRATING OBSERVATIONS AND NUMERICAL SIMULATIONS OF THE 2000 YIGONG FLOOD**

Outburst floods in mountainous landscapes traverse complex topography and interact with the channel and valley walls, producing intense flow hydraulics that drive geomorphic change and impact people and infrastructure. Evidence of modern and ancient outburst floods is scattered around the eastern Himalaya, but hydraulics related to these geomorphic features are uncharacterized, limiting our understanding of the role of large floods in long-term evolution of the region. Here we combine remote and field observations of the 2000 Yigong River landslide-dam outburst flood with 2D numerical flood simulations using the software GeoClaw. Modeling results agree with field evidence to the extent that we judge the simulated hydraulics to be relevant to flood hazard and geomorphic investigations. Results show that the hydraulics of outburst floods through rugged topography differ from those expected for non-flood flows, in magnitude and in the spatial patterns of flow speed, direction and shear stress. The flood produced sustained high bed shear stresses capable of plucking meter-scale blocks immediately downstream of breach, in the steep Tsangpo Gorge, and in isolated locations associated with valley constrictions. Simulated shear stresses suggest that outburst floods deposited numerous kilometer-scale boulder bars observed along the flood pathway, armoring the bed, increasing channel roughness, and inhibiting incision in locations that would not be predicted for non-flood flows. Our findings highlight the potential for different magnitude flows to promote not only different amounts, but different patterns of bedrock erosion, with implications for the role of prehistoric megafloods in the topographic evolution of the eastern Himalaya.

1.1 INTRODUCTION

High-magnitude (>10^5 m^3/s) lake outburst floods can dramatically alter landscapes and greatly impact human lives and infrastructure. Yet links between spatial patterns of flood hydraulics and geomorphic observations are lacking for some of the largest, most devastating historical outburst floods (e.g., Hewitt, 1968; O'Connor et al., 2013), and for many of the largest ancient outburst megafloods (>10^6 m^3/s) that have occurred on Earth (e.g., Bretz, 1923; Malde, 1968; Baker, 1973; O'Connor, 1993; Carling, 1996a,b; Herget and Agatz, 2003; Montgomery et al., 2004; Lamb et al., 2008b; Baynes et al., 2015) and on Mars (Baker and Milton, 1974; Baker, 2001; Chapman et al., 2003; Goudge and Fassett, 2018). Opportunities are rare to study outburst floods and their geomorphic consequences (Lamb and Fonstad, 2010; Cook et al., 2018). As a result, questions remain regarding the net impact of outburst floods on landscapes, particularly in mountainous settings where the interaction of flood hydraulics with valley topography is complex.

In the eastern Himalaya, abundant evidence for valley blockage by glacial and landslide dams (Zhu and Li, 2001; Guangxiang and Xitao, 2007; Montgomery et al., 2008; Chen et al., 2008; Korup and Montgomery, 2008; Korup et al., 2010; Guangxiang and Qingli, 2012; Huang, 2014; Hu et al., 2018)—some with downstream evidence of flooding—suggests that catastrophic outburst floods may have been common throughout the Quaternary. Such evidence has led workers to propose a variety of models for the role of outburst floods in deposition and channel incision, particularly in the steep and rapidly eroding Tsangpo Gorge region within the Yarlung-

Siang-Brahmaputra River drainage (**Figure 1.1a, b**). It has been proposed that Quaternary glacial dams impeded bedrock river incision into the Tibetan plateau (**Figure 1.1b**; Korup and Montgomery, 2008; Korup et al., 2010), and that catastrophic glacial outburst megafloods focused erosion in the Tsangpo Gorge (Montgomery et al., 2004; Finnegan et al., 2008; Korup and Montgomery, 2008; Korup et al., 2010; Lang et al., 2013). Historical outburst floods caused by the failure of natural landslide dams have also been documented in the Gorge region (Zhu et al., 2001; Shang et al., 2003; Zhu et al., 2003; Evans and Delaney, 2011; Delaney and Evans, 2015). Such events have been linked both to lateral channel scour as a driver of landslide erosion (Larsen and Montgomery, 2012) and to sediment delivery effects on river transport capacity (Finnegan et al., 2008). These and other studies point to the potentially strong influence of outburst floods on the evolution of mountainous landscapes. Improved understanding of flood hydraulics should enable better understanding of the processes by which outburst floods erode and impact river morphology, and the extent to which they might differ fundamentally from the processes at work during background flows.

This study examines the hydraulics and geomorphic effects of the second largest historical landslide-dam outburst flood on record, the June 2000 Yigong River outburst flood (Zhu and Li, 2001; Shang et al., 2003; Zhu et al., 2003). This flood coursed down a >450 km stretch of river through the rugged topography of the Tsangpo Gorge region before exiting the Himalayan rangefront (**Figure 1.1**). We numerically simulate the flood using the depth-averaged (two dimensional, 2D) shallow water equations for flow over three-dimensional topography. Well-balanced finite-volume methods and block-structured adaptive mesh refinement (AMR) are implemented in the open-source software GeoClaw (Berger et al., 2011; LeVeque et al., 2011) to enable efficient simulation of the advancing flood wave over the large (>2.1 x10^4 km^2) spatial extent and multi-day duration of the event. We compare simulation results to flood observations, discharge estimates, and new field-surveyed high-water marks and slackwater flood deposits to determine the applicability of the model for hazard assessment and geomorphic investigations in steep, rapidly incising landscapes. Spatial and temporal variations in flow depth, direction and speed in the context of remote sensing observations enable us to investigate (1) spatial and temporal patterns of bed shear stress driven by the interaction of the flow with valley topography, (2) the size of blocks that can be plucked to incise bedrock, and (3) the potential effects of flood-related boulder bar formation on bed armoring and channel roughness relevant to long-term evolution of the Tsangpo Gorge.

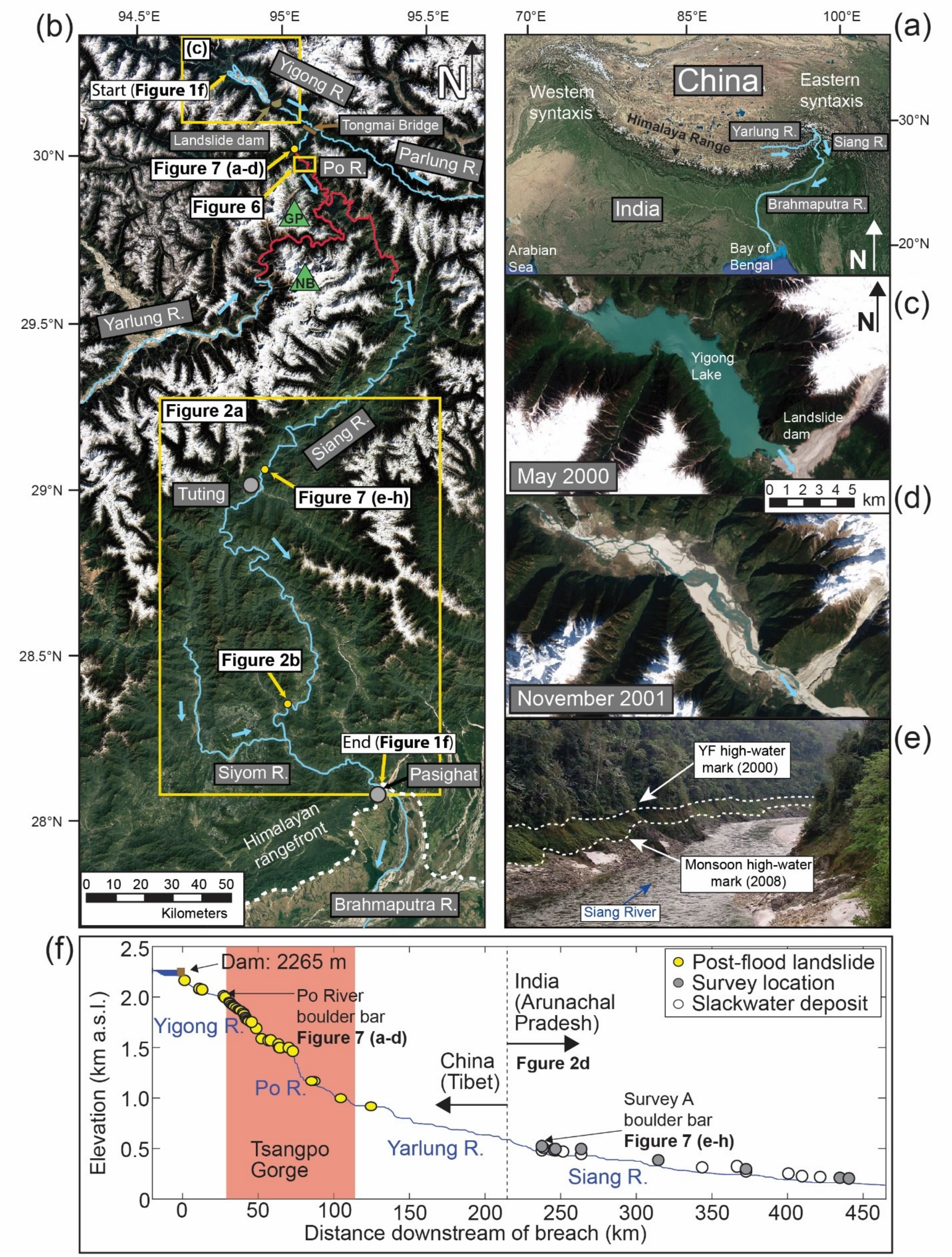

Figure 1.1. Location map of study area.

Google Earth image of the study area (a,b), with Tsangpo Gorge in red. The image in (b) shows the flood source, dam, and a close-up of the flood pathway. Landsat-7 imagery shows (c) the Yigong River impoundment and (d) the post-flood landscape. Photograph (e) shows mapped high-water marks of the year 2000 Yigong landslide-dam outburst flood (labeled YF) and the 2008 monsoon. The longitudinal river profile in (f) shows geomorphic features from the flood.

1.2 BACKGROUND

1.2.1 *Geomorphic setting and outburst floods of the Tsangpo Gorge region*

The eastern Himalaya is one of the most rapidly uplifting and eroding regions on Earth, characterized by extreme topographic relief and powerful rivers of the Yarlung-Siang-Brahmaputra River drainage (**Figure 1.1a**). Here, collision between India and Asia has produced mountains with >7 km peaks and long-term exhumation rates that exceed 5 km/My (Burg et al., 1998; Ding et al., 2001; Malloy, 2004; Seward and Burg, 2008; Booth et al., 2009; Zeitler et al., 2014; Bracciali et al., 2016; Lang et al., 2016). The Yarlung-Siang-Brahmaputra River slices through these high mountains of the Himalaya in Tibet and India, carving the Tsangpo Gorge in a knickzone where the river drops more than 2 km of elevation over a distance of <100 km. The river's high stream power and sediment transport capacity (Finnegan et al., 2008) through the Gorge have enabled it to cut a tortuous channel into bedrock between steep, rapidly eroding hillslopes at the threshold of failure (Larsen and Montgomery, 2012).

The high elevation, high relief and rapid erosion set the stage for river damming and outburst floods. Sedimentary and geomorphic evidence from Tibet shows that outburst megafloods have occurred repeatedly over the last 50 ka, sourced from glacially-impounded lakes in Tibet; failure of lakes as large as 835 Gm^3 unleashed peak discharges up to 5×10^6 m^3/s (Montgomery et al., 2004; Liu et al., 2006; Guangxiang and Xitao, 2007; Korup and Montgomery, 2008; Kaiser et al., 2010; Guangxiang and Qingli, 2012; Zhu et al., 2013; Zhu et al., 2014; Huang, 2014; Liu et al., 2015; Chen et al., 2016; Hu et al., 2018; Liu et al., 2018).

Historical outburst floods include those in 1900 and 2000 from landslide-dam impoundments on the Yigong River. These involved total flood volumes >2 Gm^3 and peak discharge >10^5 m^3/s (e.g. Evans and Delaney, 2015). Both historic and Quaternary outburst floods are recoded by sedimentary deposits documented downstream of the Tsangpo Gorge along the Siang River (Lang et al., 2013).

The most recent and best recorded is the June 2000 Yigong flood (Zhu et al., 2001; Shang et al., 2003; Zhu et al., 2003; Evans and Delaney, 2011). Delaney and Evans (2015) reconciled discrepancies among previous accounts of the dam, breach, and flood, summarized as follows: In April 2000, a rockslide dammed the Yigong River (**Figure 1.1c, d**) at the same location as the landslide-dam impoundment that produced the 1900 outburst flood (Shang et al. 2003). The landslide dam was stable for 62 days and a spillway was excavated before the dam failed catastrophically at ca. 21:30 on 10 June 2000 (Han, 2003; Shang et al., 2003). The spillway had reduced the impounded lake elevation by 18 m (Yang et al., 2010), decreasing the flood volume released into the Yarlung-Siang-Brahmaputra River system by 1.0 Gm^3. The >2.0 Gm^3 flood was the second largest landslide-dam outburst flood in recorded history, second only to the Great Indus River flood in 1841 of about 6.5 Gm^3 (Evans and Delaney, 2011).

Dynamics of the 2000 Yigong flood (hereafter referred to as “the flood”) are constrained by limited direct observations and discharge estimates. At the breach, estimates of peak discharge based on empirical relations between impounded lake volume and discharge range from 6.1x10^4 m^3/s (Delaney and Evans, 2015, using the relation of Evans, 1986) to 1.3x10^5 m^3/s (Shang et al., 2003, using the relation of Costa and Schuster, 1988). Where the flood destroyed a highway bridge (Tongmai Bridge) 17 km downstream (**Figure 1.1b; A1**), peak discharge of 1.2x10^5 m^3/s was proposed by Shang et al. (2003) (based on observations of peak stage) to have occurred 5 hours and 50 minutes after breach initiation; however, Delaney and Evans (2015) argue that peak discharge likely occurred much earlier given that the entire lake drained in ~6 hours (Zhu et al., 2003). Delaney and Evans (2015) simulated the first 50 km of the flood numerically using FLO-2D software and a 90-m digital elevation model. They initiated the simulation with a synthetic hydrograph scaled to their estimated peak breach discharge of 61,461 m^3/s, producing maximum discharge, water depth and velocity estimates at Tongmai Bridge of $1.1x10^5$ m^3/s, 54.9 m, and 14.57 m/s, respectively (**Figure 1.1b; A1**). The initial flood wave was first recorded at a river gauge approximately 462 km downstream from the breach in the town of Pasighat, India, on 11 June at 18:00, an estimated 17 hours and 50 minutes after the breach initiated. Maximum rise in stage here was 5.54 m, and peak discharge was $4.4x10^4$ m^3/s (4 times the background discharge of 1.1 $x10^4$ m^3/s), measured 5 hours after the initial rise in the water level (Tewari, 2004). Tewari et al. (2004) estimate that peak discharge at Pasighat occurred 22 hours and 50 minutes after the breach; the absolute time of flood arrival and peak discharge near Pasighat are known, but Tewari et al. (2004) do not report the precise location of the Pasighat river gauge, and Evans and Delaney (2011) estimate an uncertainty in the breach timing of 30 minutes, which together contribute uncertainty to this travel time estimate.

The flood caused life and property losses, erosion and sedimentation. In China it destroyed at least six bridges and damaged the highway system (Delaney and Evans, 2015). Many bridges were destroyed in Northern India, where the flood killed at least 94 people (Han, 2003). The flood also triggered significant landslide erosion (Larsen and Montgomery, 2012). No direct observations of bedload transport or channel incision are available. However, Lang et al. (2013) used an empirical estimate of peak breach discharge ($6.1x10^4$ m^3/s) and equations for bed shear stress and incipient motion to estimate that the flood could move blocks up to 3 m in size in the Tsangpo Gorge. The flood also produced alluviation along the Yigong River (Finnegan et al., 2008) and extensive slackwater sand deposits along the Siang River (Lang et al., 2013).

1.2.2 *Numerical simulation of outburst floods*

Various numerical models have been used to implement the shallow-water equations in simulations of outburst flood inundation and dynamics for hazard assessment, infrastructure planning, and geomorphic studies (e.g., Cook et al., 2009; Salvatore et al., 2013; Larsen and Lamb, 2016; Zin et al., 2018), but few models are well-suited to investigations of spatial and temporal variations in flow characteristics over large areas of rugged topography. One-dimensional models like HEC-RAS (U.S. Army Corps of Engineers) perform poorly when applied to rugged mountainous terrain (Horritt and Baits, 2002; Alho and Aaltonen, 2008; Denlinger and O'Connell, 2010) and are not useful for characterizing rapidly varying flow direction or lateral stresses along valley walls. Full three-dimensional modeling (using the Navier-Stokes equations with a free surface) might be necessary to capture the details of turbulent flows, but remains computationally infeasible for modeling the full extent of an outburst flood. Outburst flood simulation using 2D models such as TELEMAC-2D (Galland et al., 1991), LISFLOOD-FP (Bates and De Roo, 2000), SOBEK (Carrivick, 2006), TUFLOW 2D (Alho et al., 2010), and ANUGA (Roberts et al, 2015) is feasible, and such models have been used successfully to study megaflood processes (Miyamoto et al., 2006; Komatsu et al., 2009; Alho et al., 2010; Denlinger and O'Connell, 2010; Larsen and Lamb, 2016)

However, even accounting for only two spatial dimensions, 2D simulations that use a fixed computational grid (mesh) are computationally demanding—particularly when resolving flow characteristics at useful resolution (e.g., 30-250 m) over a large spatial domain. Simulations of outburst floods from Pleistocene Glacial Lake Missoula, Montana, USA, required up to 250 days of CPU time for a complete flood simulation using a fixed grid with 250 m resolution (Denlinger and O'Connell, 2009). Recent simulations of Missoula floods achieved finer resolution (~30 m), but for a much smaller spatial extent in a limited area of interest, and for short flow durations (<3 hours; Larsen and Lamb, 2012). Such fixed grids remain inefficient for a rugged mountain river over a large area because only a small proportion of the cells are inundated at a time.

For our analysis, we used GeoClaw, part of the open-source software package Clawpack (Clawpack Development Team, 2016; Mandli et al., 2016). GeoClaw incorporates a high-resolution wave-propagation algorithm to solve the depth-averaged 2D shallow-water equations (equations 1-2 in the supporting information). A chief advantage of this model is that it uses an adaptive mesh refinement (AMR), which clusters high-resolution rectangular computational cells in regions of interest along the flood pathway, automatically adjusting the region of refinement as the flow progresses (Berger et al., 2011; LeVeque et al., 2011). In this way, AMR enables efficient hydrodynamic simulation over large model domains. Similar to other models, outburst flood simulation in GeoClaw requires the user to define topography; dam location, height, and timing of dam removal; and roughness parameter, in addition to defining maximum grid resolution and setting the criterion for mesh and time-step refinement (described in Methods).

GeoClaw has been used extensively in tsunami modeling (e.g., MacInnes et al., 2013; Arcos and LeVeque, 2015), and has been formally validated for outburst floods with simulations of the Malpasset, France, 1959 dam-break flood (George, 2011). Recently, GeoClaw was used to simulate an ancient catastrophic glacial-lake drainage event in the Altai Mountains, central Asia, with the goal of linking flow characteristics to lake-bed sediment entrainment and bedform deposition (Bohorquez et al., 2015). Our study investigates a much larger magnitude outburst flood than the validation study of George (2011), and is the first to apply GeoClaw to simulate a modern landslide-dam outburst flood for which results can be compared to timing and maximum-stage observations of the flood for over >400 km downstream from the breach.

1.3 METHODS

1.3.1 *Field and remote sensing surveys of flood high-water marks, slackwater deposits and boulder bars*

We complemented sparse direct observations of flood hydraulics with field surveyed high-water marks >200-400 km downstream of the breach along the Siang River. Flood inundation (trim line), indicated by the clear change from mixed vegetation in areas that were not inundated to rapid-growth vegetation (primarily banana trees) that colonized river banks scoured by the flood, was surveyed at eight locations (A-H) (**Figure 1.1, Figure 1.2; Table A1**). High-water marks were surveyed with a handheld GPS, laser range finder, clinometer and/or tape measure in March 2008, before the start of the rainy season (March-September). At locations A-H we also surveyed the high-water mark of the monsoon river flow, indicated by the transition from bare bedrock to vegetated riverbank (**Figure 1.1e, Figure 1.2**).

Twelve slackwater deposits from the flood were identified and sampled (**Figure 1.1f; Figure 1.2a, d; Table A2**) during field seasons in March 2008 and January 2013, four of which were reported previously by Lang et al. (2013). Flood slackwater deposits along the banks of the Siang River and its tributaries were unambiguously identified in the field based on their composition, sedimentary character and grain size, position on the landscape, level of vegetation and lack of soil development, following the methods of Lang et al. (2013) (**Text A1, Figure A2**). All deposit positions were recorded with handheld GPS devices, and their elevations were derived from the digital elevation model (DEM) described in section 3.3 using the GPS positions. The vertical positions of seven of these deposits (#2-4, 7, 9-11) were also surveyed with respect to the river stage (near low flow at the time of all surveys) and monsoon high-water mark using a laser range finder and clinometer (**Table A2**). Some of these deposits (#1, 3, 4, 6, 9) were surveyed in locations where high-water marks were also identified and surveyed (locations A, B, C, D, and F) so that a direct comparison of relative elevation is possible. Grain size distributions for flood deposits were determined using a CamSizer L digital image processing particle and shape analyzer by Retsch Technology (**Table A2**).

Boulder bars were observed in the field and using Google Earth imagery from after the flood. We recorded the locations of all boulder bars that were resolvable on the imagery (i.e., >100-meter scale features) that were not associated with point bar deposition at the inside of meander bends. The location of the largest boulder bar in the model domain (>1.5 km in length), which does occur near the inside of a meander bend, was also recorded. Particle size counts were conducted on two boulder bars, using Google Earth tools to measure intermediate axis lengths on all boulders that were well resolved in the imagery.

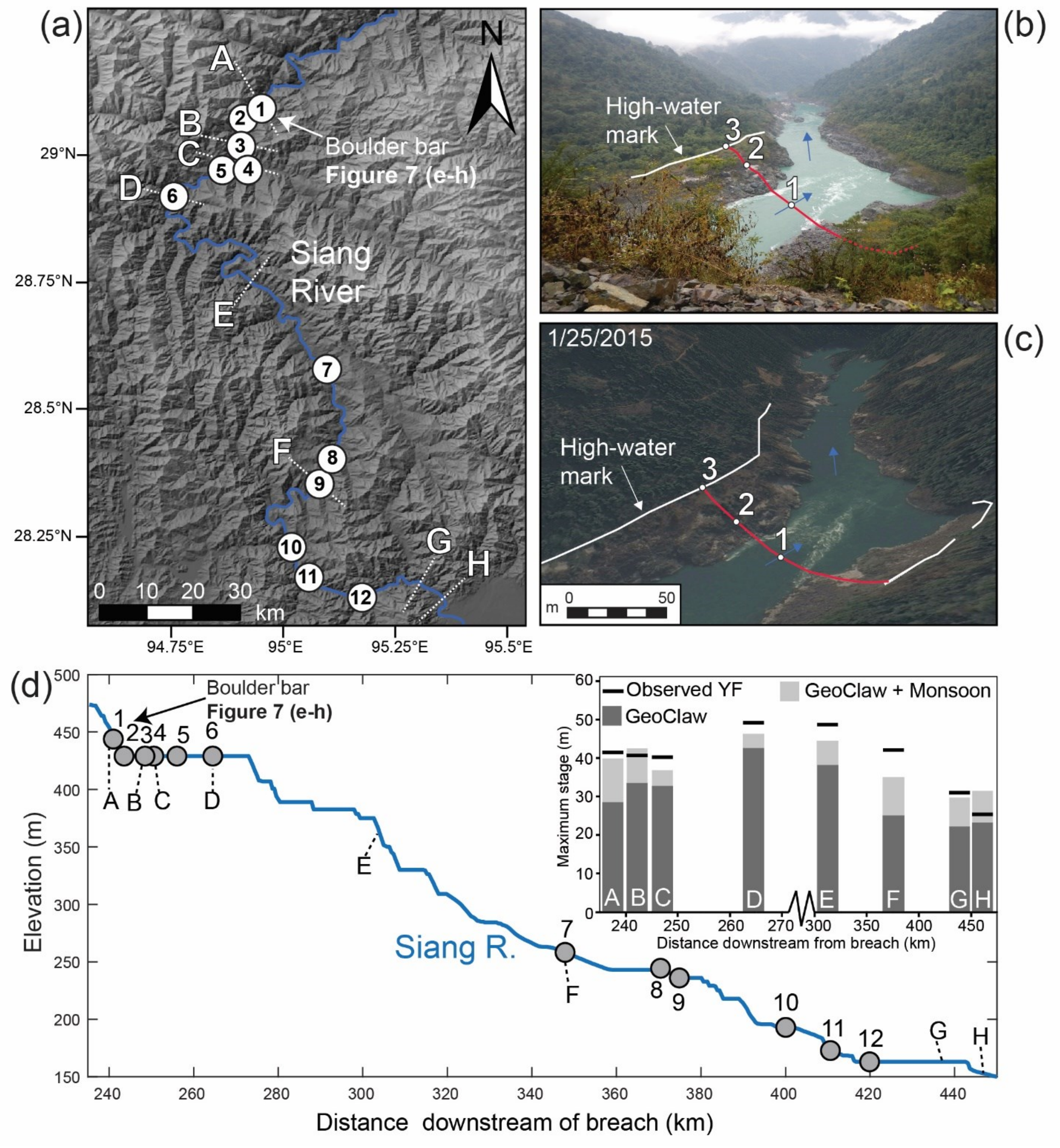

Figure 1.2. Map of deposits observed on the Siang River, northeastern India.

(a) Shaded DEM shows locations of surveyed cross-sections with high-water marks A-H and observed slackwater deposits 1-12. Field photograph taken in January 2013 (b) and Google Earth image downstream of survey C (28.3426° N, 94.9898°E) showing the low-flow water surface (1), monsoon stage (2), and flood high-water mark (3). (d) Longitudinal profile of the Siang River with survey stations and observed deposits; inset shows simulated and observed stage of the flood (labeled YF).

1.3.2 *Numerical simulations of the flood using instantaneous dam failure*

The flood was simulated in GeoClaw (version 5.4.1) on the basis of the landslide-dam height inferred by Delaney and Evans (2015) and assuming instantaneous dam failure at the breach. We modified the initialization routine in the GeoClaw code to emplace the lake volume behind a landslide dam before the simulation begins; the dam was then instantaneously removed at the start of the simulation. The modified Python routine is available, along with the GeoClaw code and scripts used for flood simulation, on GitHub (see supporting information). Our methods to develop the DEM, tune the desired AMR configuration, and tune Manning's roughness coefficient, *n,* are summarized below. User-controlled variables in the run-file include parameters to adjust time steps, solver method, boundary conditions, and physical variables like gravity and are listed in **Table A3** (see documentation on GeoClaw website: Clawpack Development Team, 2016).

1.3.3 *Topographic data and GeoClaw adaptive mesh refinement (AMR)*

The flood was simulated on a digital elevation model (DEM) spanning 21,554 km^2. The DEM is a combination of two data sources: the SRTM 3 arc-second (~90 m cells) DEM with voids filled using topographic contour data (de Ferranti, 2014), and a higher-resolution SRTM 1 arc-second (~30 m cells) DEM (SRTM data acquired February 2000). The 30 m SRTM1 dataset is used in the Yigong River and Po River reaches encompassing the first 47 km of the flood pathway (distance measured along the middle of the channel downstream of the dam breach), and in the Siang River from ~124 km to 465 km along the pathway. The 90 m SRTM3 dataset is used for the 77 km between these two segments (5.7% of the total area of the SRTM1 DEM) because of poor coverage by the 30-m SRTM1 dataset in this area. All geomorphic observations and analyses were made in the area covered by the higher-resolution SRTM1 dataset. Flood simulations (1) assume that the topographic boundary for the flood is the water surface (and valley walls) from SRTM1 data acquired prior to the flood in February 2000, not the actual channel bed, and (2) ignore any topographic changes that may have occurred during the course of the flood.

The AMR capability in GeoClaw efficiently simulates the flood by adaptively concentrating computational grid cells in a narrow band where water is present around the channel. A coarse level-1 rectangular grid with resolution of ~1 km covers the entire computational domain, a rectangle of size 86 x 244 km or nearly 2.1 x 10^4 km^2. Four more levels of refinement are used for the flood simulation that refine in space and time by successive factors of 4, 2, 2, and 2 respectively, so that level-5 has 30 m resolution. The time steps on each level are varied based on the Courant-Friedrichs-Lewy (CFL) condition (Berger et al., 2011). Initially, we force level-4 grid patches (60 m resolution) covering the region around the impounded lake. As water begins to flow into the channel following the breach, higher levels of refinement are automatically applied only around the flowing water. Different criteria can be used to flag cells for refinement, but the default AMR criterion based on water depth was used for these simulations, ensuring that almost all of the flow is simulated at the highest level of AMR (level-5; 30 m cells). By regridding every few time steps it is possible to automatically expand the portion of the valley that is refined as the flood progresses and resolve the wet-dry boundary of the flow through time on the DEM.

For the simulations reported here, we set the refinement criteria to ensure that the majority of flow computations are performed on the highest-level grid (level-5), which corresponds to a maximum grid-resolution of 30-m. The 30-m grid-resolution matches the resolution of our DEM except in the middle of the flood pathway where the resolution is 90 m.

In order to perform 30-m grid resolution simulations in the areas covered by the 90-m DEM, the software constructs a piecewise bilinear surface that is then integrated over each finite volume grid cell to determine the average topography value used in that cell. Using this method it is possible to simulate the flow at extremely high-resolution (e.g., <5 m) AMR levels even on relatively coarse topographic data. We focus on examining 30-m-resolution simulated hydraulics in areas where we use the SRTM1 30-m DEM, so that the highest level of the simulated topographic surface matches the resolution of the DEM. Additional simulations, reported in the supporting information, were performed to test the sensitivity of the computed solution to the grid resolution with maximum grid resolutions that range from 15 to 60 m.

1.3.4 *Selection of spatially and temporally uniform Manning's n*

Manning's roughness parameter (n) in the friction term of the shallow-water equations (supporting information, equation 2) was 0.04 for most simulations presented in the main text of this paper, but we also compared results from simulations using n=0.02 and n=0.06 (see supporting information). For all simulations, n is spatially uniform and does not vary with time, following previous outburst flood studies (e.g., O'Connor and Baker, 1992; O'Connor, 1993; Clarke et al. 2004; Miyamoto et al. 2006; Alho et al. 2010; Denlinger and O'Connell, 2010; Bohorquez et al., 2016).

The range of n values applied here is similar to the ranges tested in previous 1D and 2D simulations of ancient megafloods (n=0.025 to 0.075), for which simulated discharges varied minimally as a function of the roughness parameter (Carling et al., 2010). The GeoClaw outburst flood simulations of Bohorquez et al. (2015) used n=0.05 based on a gravel grain size reference value of 0.035 m consistent with Carling (1996a,b). Several other megaflood modeling studies estimated the bed roughness scale, k_s, to calculate n with the Manning equation (Manning, 1891;

Henderson, 1966). For example, researchers simulating Missoula floods characterized the average height of the surface roughness in the full domain of the model (0.17-0.81 m) and used these values and the Manning equation to calculate a range of n=0.031-0.04 (Denlinger and O'Connell, 2009). Denlinger and O'Connell (2009) chose the n=0.031 value for flood simulations, which is close to the value used in similar bedrock channels (n=0.038) for flood simulation in the Verde River, Arizona, USA (Denlinger et al., 2002). More recent simulations of Missoula floods have estimated k_s using a model in which n scales with the standard deviation of bedrock elevations of the channel (Larsen and Lamb, 2016), producing an n value of 0.065 that is higher than the values used in most other flood simulations.

Channel roughness likely varies in different segments of the flood pathway on the Yigong, Po, and Siang River. For instance, we expect higher natural roughness (n=0.06) along the Po River (Tsangpo Gorge) because of the rugged channel morphology and large roughness elements, including boulders locally larger than 10 m. Sediment input from numerous landslides here may also lead to higher roughness during the flood. Further downstream (>200-400 km) in the Siang River, exposed bedrock in the valley is smoother and channel roughness elements are generally smaller than in the Po River, suggesting a lower value (n=0.02). We discuss results of n=0.02-0.06 simulations, but focus on simulations with spatially uniform n=0.04 that is more typical of most previous flood modeling studies. Equating the Manning-Strickler relation and Manning equation, and using an estimated bed roughness length-scale, ks, of 1 m, we calculate a value of n=0.039, further supporting our choice of n=0.04 for simulations (see supporting information).

1.4 RESULTS

1.4.1 *Observations of flood high-water marks, slackwater and boulder deposits*

The positions of 12 slackwater deposits and 8 high-water marks from the Yigong flood are shown on the river profiles in **Figure 1.1f** and **Figure 1.2d**. Additional information about the deposits is in **Table A2**. Observed median grain sizes (D_{50}) in the range of 0.115-0.355 mm confirm the deposits are very-fine to medium sand (**Table A2**). High-water marks mapped in the field range from 22 to 48 m above the low-flow water surface at the time of the survey. These flood stages are on the order of 13-36 m above the typical annual monsoon high-water level (**Table A1**). Monsoon stage at these locations ranges from 8-14 m and averages 12 m above low flow (**Table A1**). Flood stage measured with respect to the monsoon high-water mark is the most relevant measurement of the rise in flood stage because the flood occurred in June, when hydrographs along the Siang River typically begin to reach monsoon levels (Datta and Singh, 2004).

A total of 76 greater-than-100-meter scale boulder bars that were not located at the inside of meander bends were mapped along the flood pathway; their locations, as well as that of the largest boulder bar in the model domain, which does occur near the inside of a meander bend, are presented in the supporting information (BoulderBar.kmz). Sixty-nine of the mapped boulder bars are within 320 km of the breach; downstream of this point, boulder bars are less frequent. Particle size counts for the largest boulder bar, located 26 km downstream of the breach in the steepest part of the flood pathway on the Po River, and for a characteristic non-point-bar boulder bar on the Siang River near survey location A and deposit 1 are also reported (**Table A4**). The median intermediate axis length on the largest Po River boulder bar and Siang River boulder bar near location A are 5 m and 3 m, respectively. Grain size decreases downstream and intermediate axis length becomes difficult to resolve with Google Earth imagery for the 8 bars located >320 km downstream of the breach.

1.4.2 *Simulations of flood hydraulics*

Results from the full range of simulated grid resolutions and roughness values are reported in the supplementary information, including animations of model output from n=0.04 simulations showing flow depth, calculated shear stress and Froude number (**Figure A3, A4; Table A5, A6, A7; Videos A1-A8**). Simulations with maximum grid resolution of 15 m encountered instabilities in flat-lying areas of topography generated from the SRTM1 30-m dataset that made it difficult to accurately map inundation. Therefore, we restrict discussion here to a summary of results of 30, 45, and 60-m simulations.

Near the breach, simulated flow depths (stages) are relatively insensitive to the choice of grid resolution and n. For simulations with 30-m maximum grid resolution and n=0.04, the peak breach discharge (1.73×10^5 m^3/s) occurred 0.12 hours after the breach (**Figure 1.3a**). The peak breach discharge and arrival time in the n=0.02 and 0.06 simulations differ from these values by up to 3.7% and 6.2%, respectively (**Table A6**). At 17 km downstream of the breach at Tongmai Bridge, the shapes of simulated hydrographs are nearly identical for n=0.02, 0.04 and 0.06 simulations; the time of flood wave arrival for these roughness values ranges from 12 to 24 minutes (**Figure 1.3b**; **Table A6**). Simulations using n=0.02 and grid-resolutions of 30-60 m also produce similar hydrographs, with peak discharge on the order of 1.39×10^5 m^3/s (**Figure A3**). Simulated maximum flow depths at this location range from 76 to 79 m (i.e., <4% difference) using various combinations of n and grid resolution, and occur at 1.2-1.7 hours after the breach (supplementary information **Table A6**).

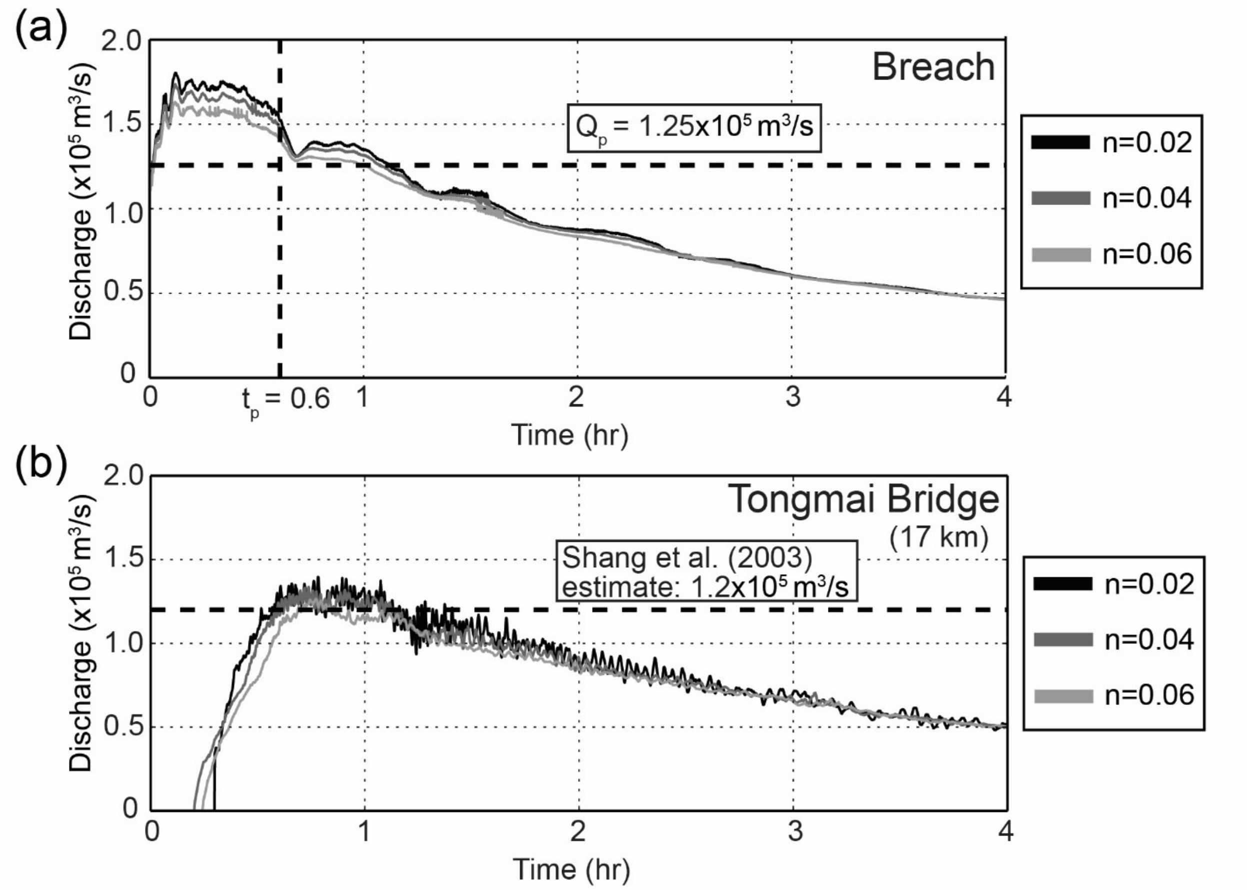

Figure 1.3. Simulated discharge at the breach and Tongmai Bridge.

(a) Discharge recorded at the breach from simulations with *n*=0.02, 0.04 and 0.06 over the first four hours of the flood. Q_p is the estimated peak discharge using predictive equations from Walder and O'Connor (1997), and t_p is the time of peak discharge estimated using a rapid natural landslide-dam failure rate. (b) Hydrographs from the same simulations at Tongami Bridge that show little sensitivity to *n*.

Maximum flow depth and speed vary spatially along the flood pathway as a function of valley shape (e.g., **Figure S4, S5**). For all *n* and grid-resolution simulations, the highest flow depths (up to 108 m) and speeds (up to 56 m/s) are observed 28-49 km downstream of the breach along the Po River (**Figure S5**). Here and at other locations, maximum flow depths are higher (and velocities lower) above valley constrictions than immediately downstream (**Figure 1.4; A5**). At the high-water mark survey and deposit locations, maximum flood stage ranged from 21 to 41 m above the base of the DEM for the 30-m resolution, *n*=0.04 simulations (**Table A1, A2**).

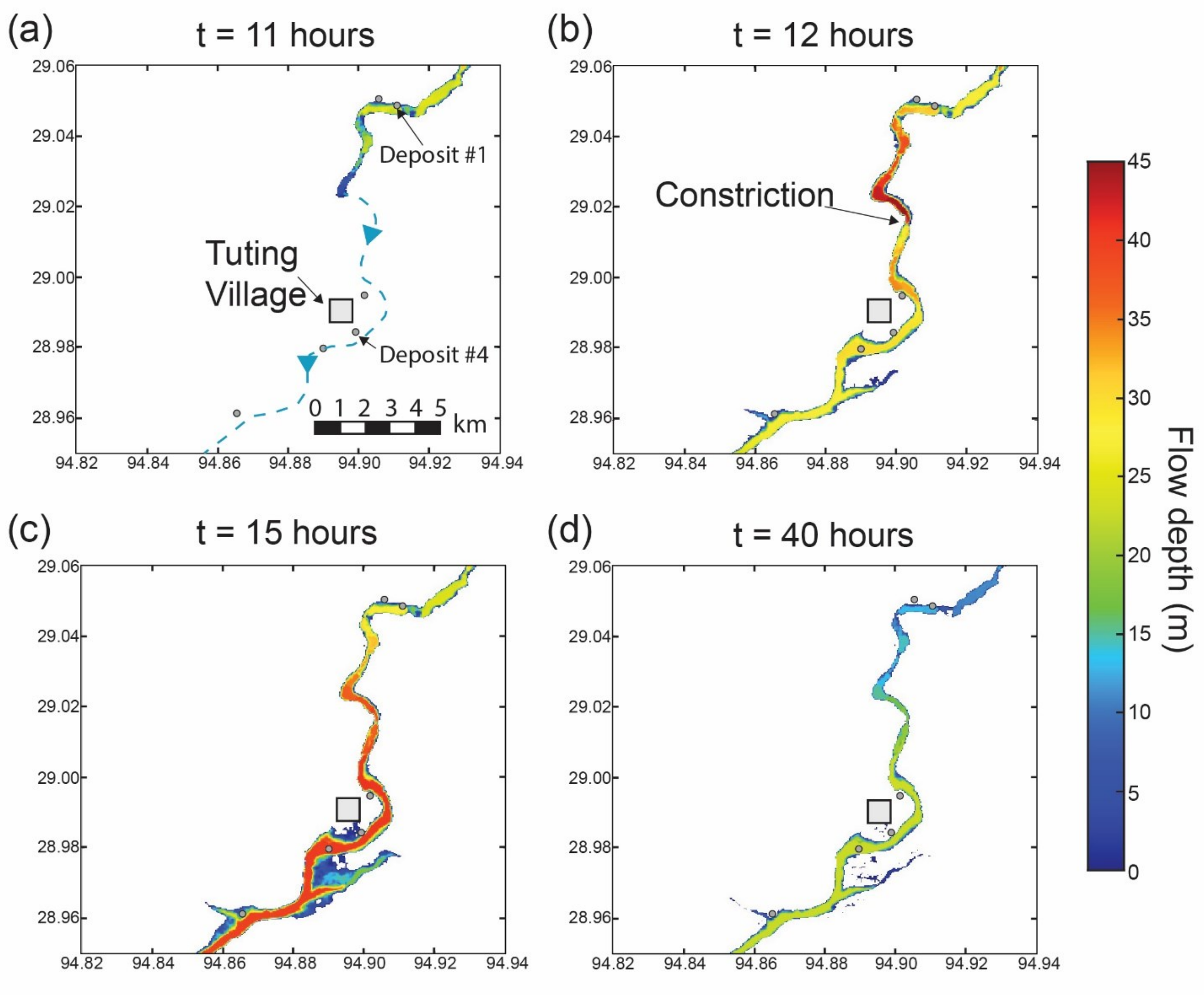

Figure 1.4. Simulated depths around Tuting Village.

Simulated depths for *n*=0.04 simulations around the Tuting village. (a) The flood wave arrives around ~11 hours after the breach. (b) Flow depths up to 45 m occur behind a valley constriction at t=12 hours. (c) Maximum inundation occurs at t=15 hours. (d) Flow depths at t=40 hours after the breach, by which point flood waters have receded from terraces where slackwater sand deposits were observed; see supplemental videos for additional time steps.

Although spatial patterns of flow speed are relatively insensitive to *n*, the magnitude of flow speed varies substantially with *n*, affecting local flow velocity and downstream flood translation. As a result, the timing of flood wave arrival is increasingly sensitive to the choice of roughness parameter with distance downstream (**Table A6**). At location A, 238 km downstream of the breach, arrival time for the 30-m grid resolution simulations varies by up to 15% (1.9

hours) between *n*=0.02 and 0.06 simulations (**Figure A4**; **Table A6**). At the farthest extent of the flood simulation 462 km downstream of the breach, the timing of the flood wave arrival varies by 25% (25.3 to 31.7 hours) for 30-m simulations with different *n* values (**Table A6**). Simulated flood travel times from the breach to Pasighat for the *n*=0.02 and *n*=0.04 simulations are ~10% and 25% greater than the travel time reported by Tewari et al. (2004), respectively.

Simulated flow depths at deposit and survey locations up to 373 km downstream of the breach (locations A-F) are relatively insensitive to the choice of roughness parameter (**Figure A4**), but flow depths between different *n* simulations vary by up to a factor of two further downstream where the valley is wider. Maximum simulated flow depths for 30-m simulations vary by only 1-7% (0.4 to 1.7 m) as a function of roughness parameter at locations A-F. In the distal part of the flood simulation, 435-440 km downstream of the breach at locations G and H, maximum flow depths vary by 78.5% (16.3 m) and 102% (22.6 m) between the *n*=0.02 and *n*=0.06 simulations, respectively (**Table A6**).

1.5 EVALUATION OF FLOOD SIMULATION RESULTS

Here we compare simulations and observations of the flood to evaluate the major assumptions in our modeling approach, including instantaneous dam failure and topographic boundary conditions.

1.5.1 *Sensitivity of model results to the assumption of instantaneous dam failure*

The assumption of instantaneous dam failure in our simulations leads to higher peak discharges and shorter time to peak discharge than would be expected based on empirical estimates for dam failure (O’Connor and Beebee, 2009). At the breach, simulated peak discharge (1.73×10^5 m^3/s) exceeds by 32% the discharge (1.25×10^5 m^3/s) estimated using the benchmark predictive equations for natural, constructed, and scale-model dam failures of O'Connor and Beebee (2009) and Walder and O'Connor (1997) (**Figure 1.3a**). More information about the geometry of the Yigong landslide dam would be needed to apply breaching models using sophisticated predictive equations that involve dam dimensions (e.g. Froehlich, 2016). The time to peak discharge, t_p, can be estimated based on the timescale of natural landslide dam failures, which varies over several orders of magnitude depending on the erodability of landslide material and failure mechanism (e.g., Walder and O'Connor; O'Connor and Beebee 2009; Garcia-Castellano and O'Connor, 2018). Many natural landslide dams made of unconsolidated material fail by overtopping in <1 hour (Hewitt, 1968; Costa, 1988; King et al., 1989; Costa and Schuster, 1991; Plaza-Nieto and Zevallos, 1994; Canuti et al., 1994), but dam erosion rates can also be several orders of magnitude slower, thereby producing longer breaching timescales (e.g. O'Connor and Beebee, 2009, and references therein). The unconsolidated Yigong landslide dam failed by overtopping, so we expect a rapid time to peak discharge, potentially on the order of t_p=0.6 hours based on the erosion rate of the natural dam on the Birehi Ganga River in India ($2.5\text{x}10^{-2}$ m/s) (**Figure 1.3a**; O'Connor and Beebee, 2009). Given the variability in flow speed from simulations with different roughness values (**Figure 1.3a**), t_p on the order of one hour or less suggests that the precise timescale of dam failure may have less effect on the timing of flood wave arrival downstream than the magnitude and spatial variability of natural roughness.

At Tongmai Bridge 17 km downstream, our instantaneous dam-breach simulations yield peak discharge and flow depths that are higher than previous model results, but similar to estimates based on field observations of stage. Our simulated maximum discharge and flow depth (76 m) are higher than the $1.1\text{x}10^5$ m^3/s discharge and 54.9 m flow depth estimates produced by the FLO-2D simulations of Delaney and Evans (2015). Much of this difference likely results from the use of an empirically estimated breach discharge (6.1×10^4 m^3/s) in the Delaney and Evans (2015) model, which is much lower than the discharge produced by both our simulations assuming instantaneous dam failure and predictive equations for dam breaching from O'Connor and Beebee (2009). However, it is difficult to compare the simulations directly because Delaney and Evans (2015) simulated the flood using an older DEM (SRTM3) that differs from our DEM (SRTM1) in the first 20 km of flood pathway. It is also difficult to compare simulated flow depth and flood peak arrival time to the field-based estimates of Shang et al. (2003) because of uncertainties in the reference point for measuring flood flow depth with respect to the destroyed bridge height as compared to the simulated flow depth with respect to the DEM surface, and the potential incompatibility of the Shang et al. (2003) timing estimate with other observations of the flood (Zhu et al., 2003). Nevertheless, our simulated peak discharge only exceeds the maximum instantaneous discharge at Tongmai Bridge reported by Shang et al. (2003) by ~10%, which indicates good agreement given the uncertainties.

1.5.2 *Comparison of simulated stage to observed high-water markers and deposits*

We focus on high-water marks mapped in the field as the most robust data available to evaluate simulated flood stages (**Figure 1.1e, Figure 1.2; Table A1**). Some apparent scour features are visible in post-flood Landsat-7 imagery of the first 20 km of the flood (**Figure A1**), but the available cloud-free Landsat 7 scenes immediately postdating the flood (June 2000) do not permit high-water marks to be unambiguously distinguished from slumping and mass failures near the edge of the channel. Clearer imagery was acquired too long after the flood (26 months) to precisely constrain flood-coeval bank erosion as a proxy for maximum inundation.

Simulated inundation should exceed the elevation of all deposits (**Table A2**) and meet all mapped high-water marks (locations A-H**; Table A1**). Simulated stages exceed the level of 9 of the 12 deposits reported in **Table A2**, and of the high-water mark at location H, but do not attain the level of high-water marks along the Siang River at field survey locations A-G (**Table A1**). The mismatch generally increases downstream, ranging from 15-22% of observed flood stage at A-C (238-247 km downstream of the breach) to 27-37% at D-G (264-435 km downstream of the breach) (**Table A1**). High-water mark elevations were surveyed with respect to the river low flow level with sub-meter-scale accuracy; additional error in the relative position of these measurements with respect to the simulation owes to uncertain interpretation of maximum flood stage due to vegetation growth since the flood, which we estimate to be on the order of 0.5 m, and also to uncertainties in the DEM itself. The magnitude of the discrepancies indicates that measurement error alone cannot explain these results at most locations. The mismatch cannot be explained by instantaneous dam failure, which results in flow depth overestimates rather than underestimates.

The flood occurred during monsoon flow conditions, but we do not explicitly model monsoon discharge; therefore, some of the discrepancy between simulated and observed stage may arise because the DEM representing the position of the water surface and valley walls is based on elevation data acquired at low flow. Ideally, we would test this hypothesis by comparing discharges from the flood simulations to estimates of monsoon and flood discharges at each survey location. Discharge (*Q*) can be estimated as the product of the flow cross-sectional area (*A*) and velocity (*V*) estimated from Manning's equation:

$$V = \frac{1}{n}\left(\frac{A}{P}\right)^{\frac{2}{3}} S^{\frac{1}{2}} \tag{1.1}$$

Where *P* is the wetted perimeter, and *S* is the channel gradient, which is assumed to be the water surface slope. Our field measurements of monsoon and flood high-water marks combined with

DEM measurements should in theory enable monsoon and flood discharges to be calculated in this way. However, the coarse resolution of the DEM introduces large uncertainties in channel gradient measurements, particularly in Siang River segment of the flood pathway where $S<0.002$. Measurements of A are underestimated based on the DEM due to the lack of bathymetric data for the channel. The choice of n also contributes to uncertainty in velocity and therefore discharge estimates. We suggest such uncertainties make it difficult to estimate discharges within ~50-71% (**Text A6**), making the calculation of limited use for our analysis.

We therefore evaluate the hypothesis that the addition of monsoon flow could account for the discrepancy between simulated and observed flood stages using rough estimates of the amount of water displaced by the monsoon that is not accounted for in the model. Calculating the cross-sectional area of water displaced by the monsoon taking into account valley geometry at all field survey stations (**Figure 1.5**; **A6, A7**) produces stage adjustments of 1-5 m (2-12% of flow depth) for survey locations A-G (**Figure 1.2d**). At survey H (440 km), simulated stage exceeds the observed high-water mark (**Figure A7**) so that the adjustment here is an overestimate of 7 m or 31% of the observed flow depth, which is potentially due to variations in natural roughness that are not accounted for in the model.

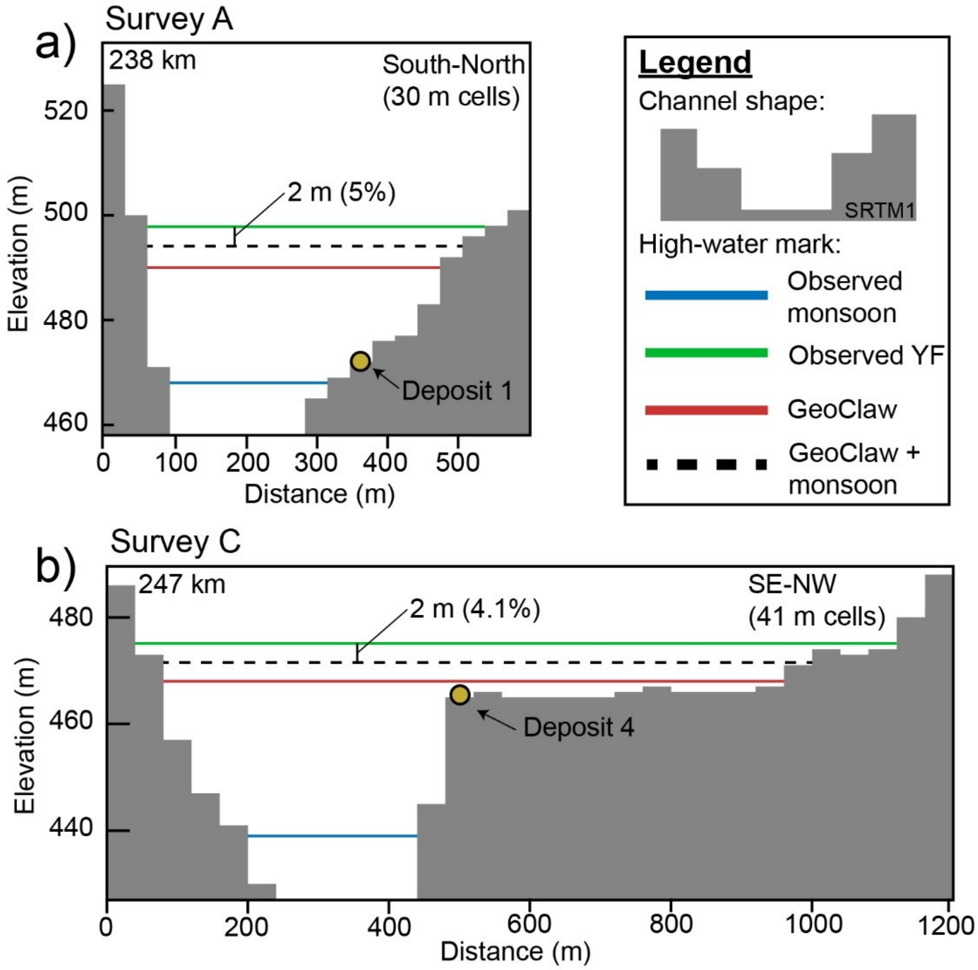

Figure 1.5. Simulated stage mapped onto valley topography cross-sections

Simulated stage mapped onto valley topography represented by the SRTM1 DEM at survey locations A (a) and C (b). The observed monsoon (blue) and flood high-water marks (green) were mapped with respect to the lowest elevation in the DEM cross-section. The dotted line represents the sum of the cross-sectional area of the monsoon and GeoClaw simulation at each location. The cross-sections are oriented downstream and the width of the cells depends on the trend of the cross-section with respect to the DEM. See supporting information for additional plots and details.

We suggest adjustments of this scale would be sufficient to raise flow depths above the three deposits (#2, 8, and 10) that were not inundated in our simulations. Simulated flow depth falls short of inundating deposit #10 by < 1 m and #2 by only 1 m (3% of flow depth), while deposit #8 is 3 m (13% of flow depth) above the maximum simulated flow depth (**Table A2**). Some of the difference at deposit #8 may owe to position uncertainties of 7-15 m from the handheld GPS, resulting in elevation uncertainties of at least 7-15 m compared to the flow depth in these locations.

Although the area-based approach does not explicitly account for discharge, the above calculations nevertheless suggest that the discrepancy between observed and simulated stages may be approximately accounted for by adjusting river base level for monsoon stage at the time of the flood. The magnitude of simulated-observed stage mismatch generally increases downstream (**Table A1**), as does total monsoon discharge, suggesting that geomorphic analyses may be most robust in the first ~250 km of the flood pathway. At the farthest downstream point of our simulation in Pasighat, observed monsoon discharge is on the order of 1.1 x 10^4 m^3/s, or 25% of the total peak discharge during the flood (Tewari et al., 2004). Future work will explicitly simulate monsoon discharge calibrated to these observations in order to rigorously assess the contribution of background discharges to flood stage and hydraulics.

The choice of uniform roughness parameter also likely contributes to the mismatch between observed and simulated stages. The fact that n=0.04 models overestimate the travel time of the flood wave from the breach to Pasighat reported by Tewary et al. (2004) is consistent with our expectation based on the scale of roughness elements observed in the field that a lower roughness value may be more appropriate for the distal portions of the model domain. Failure to account for such spatial (as well as temporal) variations in roughness may also contribute to the divergence of simulated and observed stages in distal portions of the flood pathway, particularly where wider channel/valley morphologies (e.g., **Figure A7**) may contribute to increased sensitivity of the flow to local bed roughness.

1.6 INSIGHTS INTO OUTBURST FLOOD HAZARD AND GEOMORPHIC PROCESSES

The modeling results match field evidence to the extent that we judge the simulated hydraulics to be relevant to flood hazard and geomorphic investigations, despite the assumption of instantaneous dam failure, use of spatially and temporally uniform roughness parameter, and lack of explicitly modeled monsoon river base flow. We therefore consider simulated hydraulics in the context of flood hazard assessment and of valley morphology, erosional features and deposits. Computation is efficient and inundation patterns are relatively insensitive to grid resolution and roughness parameter at the scale of the 30-m DEM, making this a promising modeling approach for hazard assessment in mountainous regions. Flow depth, speed and direction, as well as the magnitude, duration, and spatial distribution of calculated bed shear stress, are strongly influenced by the interaction of the flow through complex valley topography above the modern channel—with implications for fluvial and hillslope erosion, and for sediment transport and deposition in outburst floods.

1.6.1 *Implications for flood hazard assessment in mountainous topography*

Hazard from landslide-dam outburst floods is well known in mountainous landscapes around the world, many of which experience frequent earthquakes that make them especially prone to landslide-damming and subsequent failure (e.g. Korup, 2002; Korup, 2005; Weidinger, et al., 2006; O'Connor et al., 2009; Xu et al., 2009; O'Connor et al., 2013; Ruiz-Villanueva et al., 2017). There is also a growing risk of glacial-outburst floods in the Himalaya and other orogens as glaciers respond to modern climate change and produce moraine-dammed supraglacial and proglacial lake systems (Worni et al., 2013; Westoby et al., 2014). Although typically smaller than the Yigong flood, modern glacial-outburst floods can be just as deadly and damaging to infrastructure (e.g., Richardson and Reynolds, 2000a). Significant hazard is also associated with ongoing and planned hydropower projects around the Himalaya and other mountainous regions (e.g., Ahlers et al., 2014; Schwanghart et al., 2016; Sattar et al., 2018; Schwanghart et al., 2018).

Outburst flood simulation can be a cost-effective tool for hazard assessment and mitigation planning in mountainous terrain (e.g., Bajracharya et al., 2007; Shrestha et al., 2010; Schneider et al., 2014; Allen et al., 2016; Frey et al., 2018; Kougkoulos et al., 2018; Wang et al., 2018). However, most such modeling has been limited to relatively small events (but c.f., Risley et al., 2006). We have illustrated that GeoClaw enables modeling at a scale and resolution not previously possible, efficiently computing hydraulics along a >400-km long stretch of a complex river channel with an effective resolution of 30 m. Our results provide evidence that the shallow water equations, together with the GeoClaw implementation, can be used for such studies to produce results that compare well with observations. This work supplements earlier validation studies for smaller outburst floods based on simulations of the Malpasset, France, 1959 dam-break flood (George, 2011).

In particular, we have shown that the inundation patterns of the simulation results compare reasonably with observed high-water marks when a basic adjustment for monsoon baseflow is taken into account (**Figure 1.2d**), despite inherent uncertainties in the modeling due to the lack of high-resolution topographic data and lack of knowledge of the (spatially varying) surface roughness. Another source of uncertainty is the dam failure mechanism and timing. The assumption of instantaneous dam failure, such as we have made here, may be appropriate for examining flood hazard and hydraulics downstream because it represents a worse-case scenario of breaching and provides maximum estimates for peak discharge and flow depth downstream. However, this treatment of the dam failure could be improved with more sophisticated empirical dam breaching models (e.g., Westoby et al., 2015; Froehlich, 2016), particularly if parameters related to the geometry and composition of the dam are known. The precise timescale of the Yigong dam failure is unclear (Shang et al., 2003; Zhu et al., 2003; Delaney and Evans, 2015) and likely <1 hour, but future simulations could investigate the effects of different breaching rates and dam parameters on downstream flow conditions.

Comparison of GeoClaw results to observations further downstream in populated areas of the Siang River valley suggests that accounting for monsoon baseflow in the drainage may be more important to flood modeling and hazard assessment in this region than the addition of a more sophisticated dam removal scheme. Simulated flow depths that are uncorrected for monsoon stage consistently under predict observed high-water marks in the distal portion of the flood path (**Figure 1.2d; Table A1**). We expect that simulations that explicitly model baseflow on a higher-resolution DEM will produce more detailed inundation patterns that are needed to accurately map flood hazard. The previous GeoClaw modeling study of the Malpasset flood achieved simulation of stage within meters of field observations on topographic data with up to 2 m sized cells (George, 2011). Although DEMs up to 8 m in resolution are now available in some parts of the Himalaya (Shean, 2017), these data do not cover the Tsangpo Gorge or more populated areas like Tuting village. More coverage of this 8 m dataset would be useful to assess hazard from different flood scenarios in the area by enabling better resolution of channel boundaries and the shape of floodplains, which is required for more accurate inundation predictions around low-relief populated areas of the Siang River valley.

Not only the inundation pattern, but also the timing of flood wave arrival is important for planning evacuations of populated areas before a future outburst flood event that is imminent. Our simulated flow depths are relatively insensitive to the choice of roughness parameter up to

373 km downstream of the breach (**Table A1**), but the flow speed and flood wave arrival timing vary significantly as a function of *n* (**Table A6**). Spatially variable, and potentially temporally variable roughness in the model, along with a more sophisticated dam failure scheme, may be necessary to accurately predict the timing of inundation. Uncertainties in the observations of the event timing make it difficult to discriminate the relative importance of these simplifications for the accuracy of flood timing prediction. Nevertheless, simulations with instantaneous dam failure and low roughness (n=0.02) offer timing estimates that could be considered a worst-case scenario (i.e. fast downstream translation) useful for hazard assessment.

1.6.2 *Outburst flood hydraulics, shear stress patterns, and implications for erosion*

Outburst floods can cause significant block plucking and channel incision in jointed bedrock (e.g., Whipple et al., 2000; Lamb and Fonstad, 2010; Larsen and Lamb, 2016). Lateral erosion is also common during large floods in rapidly incising rivers (Hartshorn et al., 2002; Turowski et al., 2008; Barbour et al., 2009; Beer et al., 20172;), and outburst floods including the the Yigong flood and other modern lake-outburst floods are known to have promoted slope failures (e.g., Turowski et al., 2008; Larsen and Montgomery, 2012; Cook et al., 2018). We use simulated flood shear stresses and flow directions to examine the potential for bedrock plucking and channel incision, and the relationship between flow conditions and lateral erosion in the Tsangpo Gorge.

Our simulations enable more precise estimates of the spatial distribution of high bed shear stresses and size of transportable blocks for the flood than previously possible. Lang et al. (2013) used estimates of peak discharge and equations for bed shear stress and incipient motion from Lamb et al. (2008a) to estimate the size of blocks that could be transported by the Yigong flood and by a megaflood for which discharge had been estimated by Montgomery et al. (2004).

However, these calculations relied on gross simplifications of the channel geometry and flow characteristics that poorly approximate flood hydraulics in complex 3D terrain, and provide no information on spatial and temporal variations in transport conditions. For our analysis, we calculated the magnitude, duration, and spatial distribution of bed shear stress as well as Froude number (supporting information equations 4-6) through space and time for the entire flood event; animations of output from the simulation at locations discussed along the flood pathway for flow depth, stress, and Froude number (**Videos A1-A8**) are available in the supporting information. We also combined simulation results at key locations with recently developed theory for calculating the threshold bed shear stress required to pluck a protruding block of a given size via sliding (Lamb et al., 2015; supporting information equations 9-12).

In the steepest part of the flood pathway in the Po River segment of the Tsangpo Gorge, simulated shear stresses up to 5-20 kPa are capable of plucking meter-scale boulders for multiple hours during the flood. Where the highest bed shear stresses in the model domain are observed (location 1, **Figure 1.6**), we explored the potential for the flow to pluck 1-meter boulders (corresponding to k_s for our n=0.04 simulations) and 5-meter boulders (corresponding to the average median axis length on the largest boulder bar observed on the Po River; **Table A4**). Calculated bed shear stresses here exceed the peak bed shear stress estimates of Lang et al. (2013) for the flood, and are sufficient to pluck 1-meter blocks that protrude by 10%, or 5-meter blocks that protrude by 20 % (1 m), for over 9 hours during the flood. If 5-m blocks protrude by 10%, the stresses at this location are high enough to enable plucking via sliding for ~5 hours during the flow. These values are four times greater than shear stresses just half a kilometer downstream (location 2, **Figure 1.6**), highlighting the spatial heterogeneity of shear stresses within the Gorge. Even in lower-stress regions of the Gorge like location 2, flow conditions are sufficient to pluck 1-meter blocks with 10% protrusion for up to 6 hours during the flood.

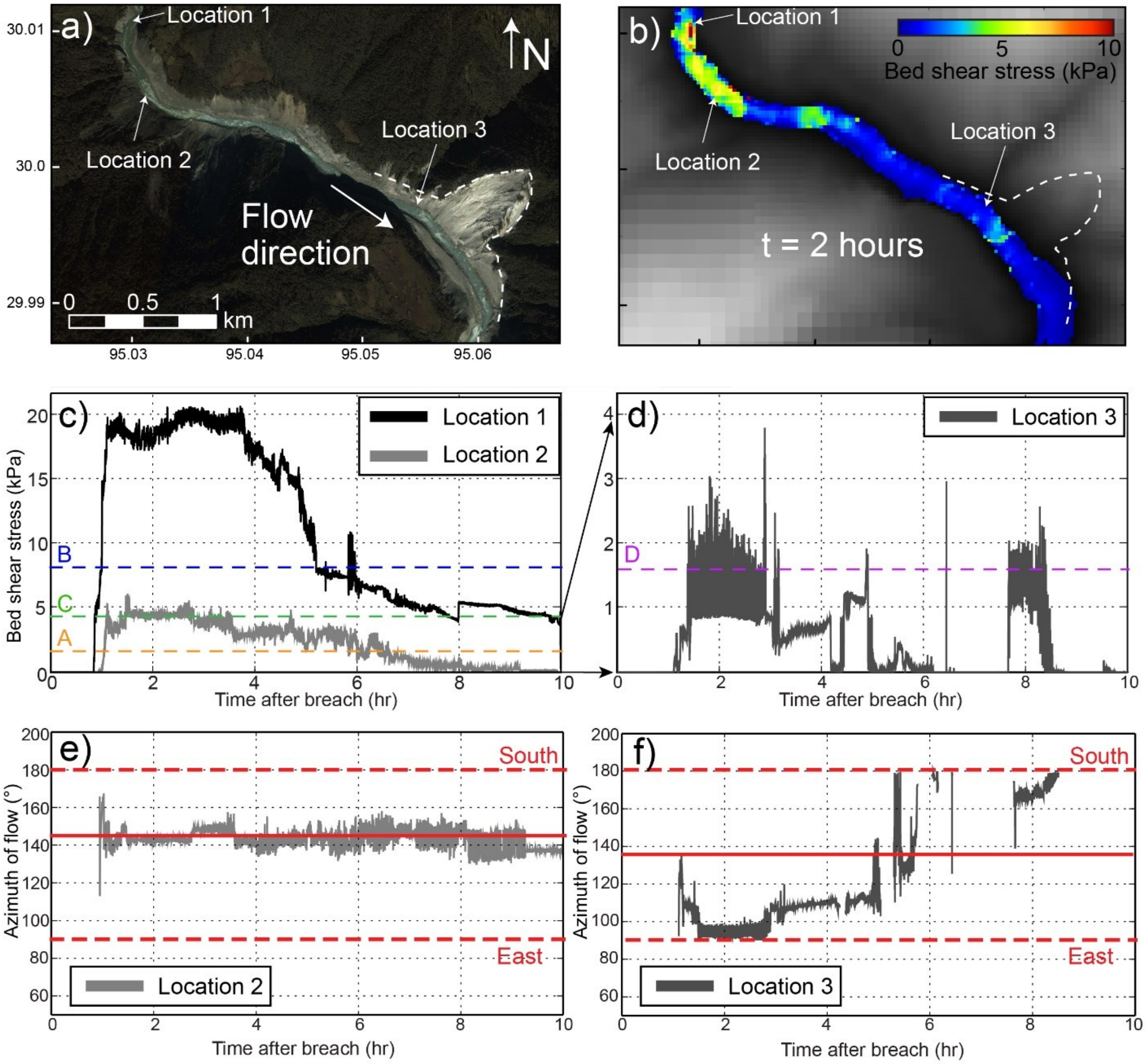

Figure 1.6. Bed shear stress and flow direction in the Tsangpo Gorge

Google Earth image in (a) shows a segment of the Po River with the outline of a large km-scale landslide. Simulated bed shear stress at t=2 hours after the breach is shown in (b). Bed shear stress recorded at locations 1 and 2 is shown in (c) and at location 3 in (d). The orange dotted line A is the threshold bed shear stress for plucking a 1-m block by sliding with 10% protrusion, the blue line B is the threshold stress for plucking a 5-m block by sliding with 10% protrusion, and the green line C is the threshold stress for plucking a 5-m block with 20% protrusion. The purple line in (d) is the threshold stress to pluck a 1-m block with 10% protrusion at location 3 at the toe of the landslide shown in (a). (e, f) Azimuth of the flow direction at locations 2 and 3. The solid red line is the orientation of the channel bank at each location, and the dotted red lines show the directions of due east and due south for reference.

Lang et al. (2013) used the size of transportable blocks to estimate the length-scale of channel bed lowering during a flood. Following this logic, the 1-5 meter length-scale of boulders that we estimate could be plucked during the flood would correspond to order 10^2-10^3-yr of incision given long-term erosion rates of 5-10 km/My. However, even though shear stresses are high throughout this steep, narrow river reach, it is unlikely that blocks could be plucked everywhere along the channel bed because bed erosion during large floods is likely to be transport limited (Lamb et al., 2015). Although sediment supply from block entrainment and hillslope failure likely restricts erosion to distinct sections of the channel, our estimates of sustained high shear stress suggest the potential for outburst floods to contribute substantially to rapid channel incision in some areas.

The flood produced sustained high bed shear stresses not only in the steep Tsangpo Gorge, but immediately downstream of breach, and in isolated locations associated with valley constrictions along the flood pathway. The initial flood wave produces high simulated shear stresses (≥5 kPa) over a significant portion of the first ~17 km of the flood on the Yigong River (**Video A2**); by about an hour into the flood, the highest shear stresses are restricted to the first 40 km downstream of the breach and to isolated zones where rapid flow is focused at valley constrictions (**Video A2**). Two of these high shear stress zones occur at topographic choke points in the Po River segment of the Tsangpo Gorge, 27 km and 31 km downstream of the breach (near locations 1-2 discussed previously). Valley constrictions far downstream on the Siang River also produce zones of high shear stress (**Video A4**), including 242 km downstream of the breach near Tuting (**Figure 1.4.** Simulated depths around Tuting Village.). The channel gradient at Tuting is an order of magnitude lower than in the Tsangpo Gorge (**Figure 1.1f**), yet bed shear stresses at this topographic choke point still exceed 2.5 kPa, which is sufficient to mobilize meter-scale blocks (**Figure 1.7e-h**). These results show the importance of valley morphology in setting up flood hydraulic conditions expected to focus erosion and sediment transport in areas not predicted by patterns of shear stress or stream power for annual flows.

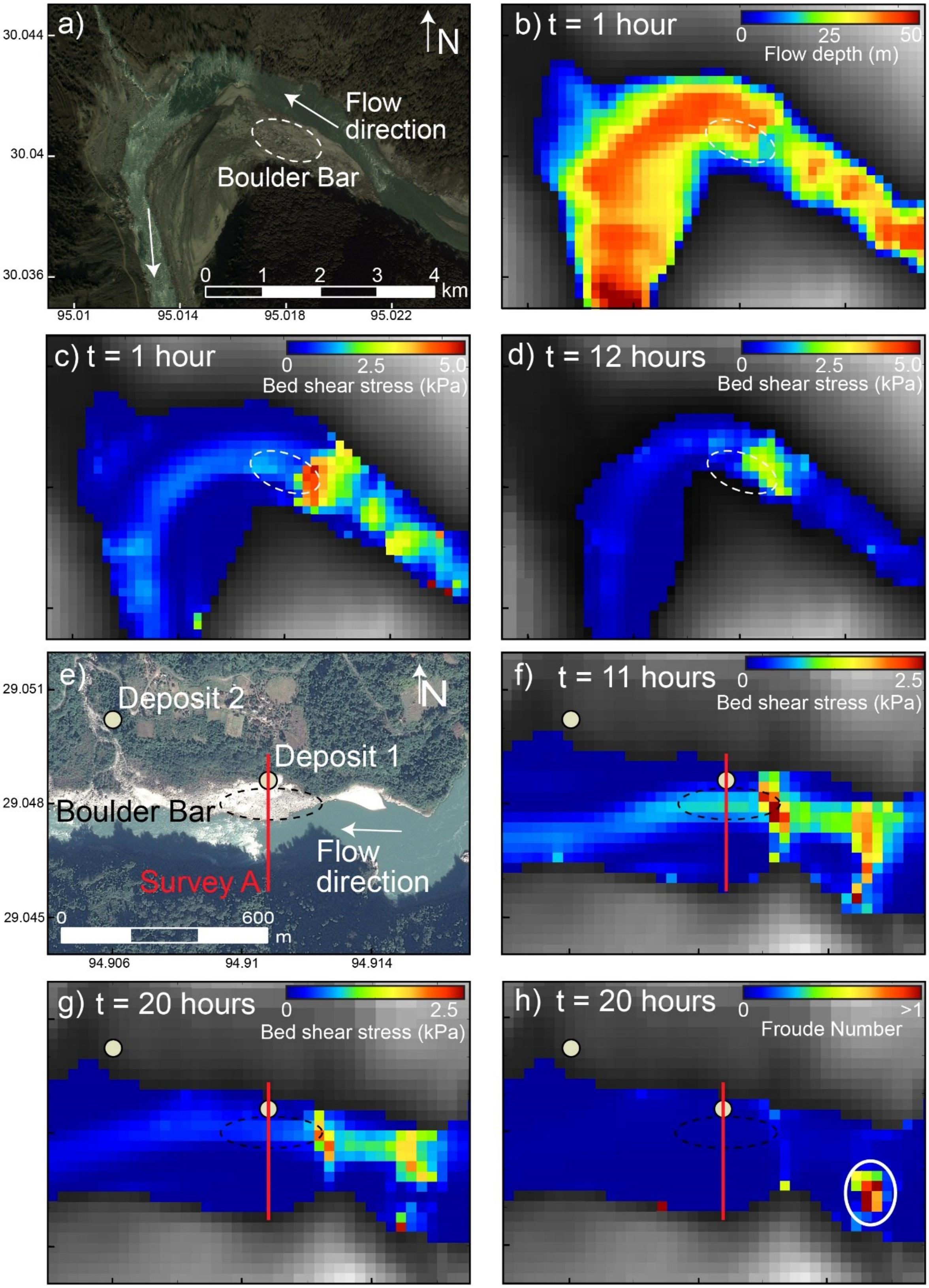

Figure 1.7. Simulated hydraulics at boulder bar locations

(a) Google Earth image (29 April 2006) showing a large meander on the Po River. Dotted oval shows where boulder size measurements were conducted. (b) Snapshot of simulated water depth at the location in (a) at t=1 hour after the breach. (c, d) Calculated bed shear stress from the simulations at t=1 and 12 hours after the breach. (e) Google Earth image (24 December 2014) showing the Siang River near survey A and boulder bar 238 km downstream from the breach. (f, g) Calculated bed shear stress in the location shown in (e) spaced 1 hour apart that show variations in the distribution of stress in the channel. (h) Froude number map at t=20 hours. Red areas indicate supercritical flow and a hydraulic jump. Scale bar for (b-d) and (f-g) is the same as the Google Earth images.

Hydraulic jumps, which are transitions between sub- and super-critical flow (Froude number >1) thought to be related to bedrock erosion (Tinkler and Wohl, 1998; Richardson and Carling, 2006; Wilkinson et al., 2018), occur at some choke points (**Figure 1.7h, Video A8**). Such flow features typically develop late in the flow after stage has waned and may persist for many hours, as illustrated by simulation results at a constriction on the Siang River 238 km downstream of the breach that show supercritical flow for 12 hours during the flood (**Figure 1h**). This hydraulic jump occurs above a ridge that is inundated only at flood stage, and therefore is not a characteristic of monsoon flow. Such simulation results highlight the potential for fast, shallow flow set up by flood-topography interaction to promote bedrock erosion in different zones than would be expected during lower-stage non-flood flows (e.g., Malde, 1968; Baker, 1973).

Finally, we investigated the relationship between simulated flood hydraulics and lateral erosion by examining bed shear stresses adjacent to the 37 large landslides mapped by Larsen and Montgomery (2012) that failed during or shortly after the flood along the Po River segment of the Tsangpo Gorge. The processes of lateral erosion in bedrock rivers are generally not well understood (e.g., Langston and Tucker, 2018). But if plucking was the dominant mechanism for lateral erosion, we might expect slope failures to be focused where high bed shear stresses directed parallel to channel walls act as lever arm to remove blocks. Flow patterns adjacent to over half of the mapped landslides (e.g., location 2, **Figure 1.6e**) show high bed shear stresses oriented at a relatively low angle to the channel wall for hours (**Table A8**), which may facilitate plucking. However, flow at some landslides—including the largest flood-related landslide in the region (location 3, **Figure 1.6f**)—is oriented at higher angles to the wall, which may inhibit plucking under high shear stress conditions and potentially facilitate abrasion via impacted particles from upstream.

At the scale of our simulations, 2D hydraulics vary significantly at the positions of these slope failures, making it difficult to draw conclusions about lateral erosion processes. Higher-resolution topography and computational grids are needed to resolve fine-scale flow features like eddies that are important for abrasion (Carter and Anderson, 2006; Lamb et al., 2008c; Pelletier et al., 2015). Factor-of-safety analysis is needed to assess controls on hillslope stability in addition to over-steepening due to lateral erosion, including changes in pore fluid pressure and cohesion due to flood inundation and vegetation scour. Future work extending this analysis is needed to better resolve topography-flow interactions contributing to lateral erosion and mass wasting during outburst floods.

1.6.3 *Implications of hydraulics for deposition, bed armoring and channel roughness*

Some studies of ancient outburst floods have related simulated hydraulics to geomorphic features and deposits (e.g., O'Connor, 1993; Herget and Agatz, 2003; Miyamoto et al., 2006; Komatsu et al., 2009; Alho et al., 2010; Denlinger and O'Connell, 2010; Bohorquez et al., 2015; Larsen and Lamb, 2016), and recent work on modern outburst floods has begun to examine relationships between hydraulics and geomorphology (e.g., Magilligan et al. 2014; Kougkoulos et al., 2018; Cook et al., 2018). Building on this prior work, we focus on the interaction of the flow with valley topography to address how outburst flood hydraulics relate to slackwater-sand and boulder boulder-bar deposition, with implications for bed armoring and roughness relevant to long-term river incision.

Simulated flow patterns suggest that the timing of slackwater sand deposition, and the elevation of slackwater deposits relative to peak flood stage, depend on the interaction of flow hydraulics with local valley topography. Some deposits are located on terraces that are only submerged early in the flood near peak inundation. For instance, deposits 3 and 4 on terraces near Tuting (**Figure 1.4, Figure 1.5; Video A3**) are inundated up to 0.1 to 5 m, respectively, from ~2 to 11 hours after the flood wave arrival (**Figure A4**). Simulated bed shear stresses at deposit 4 are sufficient to suspend the observed 90th percentile grain size (for criteria for suspension see supporting information equations 13-15), and fluctuations in flow speed as flood stage wanes are consistent with laminations present in the deposit. The correspondence between simulated hydraulics and characteristics of this and other deposits shows the potential utility of GeoClaw for predicting the location of historical or ancient outburst flood deposits where inundation patterns are unknown (Denlinger et al., 2002; Bohorquez et al., 2015). However, other flood sand deposits are located on surfaces much lower in elevation with respect to the river, where simulated bed shear stresses remain much higher than the threshold for sand suspension until >20 hours after the flood wave arrives (e.g., deposit 1, **Figure 1.5; Video A4**). These observations suggest high concentrations of sand-size sediment were in suspension as the flood waned, and show that the relationship between deposit elevation and maximum stage may vary significantly for a single flood. This finding suggests additional constraints on provenance and/or age may be needed to correlate ancient slackwater deposits recording outburst flood events.

The simulation results also provide evidence of a link between flood hydraulics and the deposition of large boulder bars along the flood pathway. We focus on bars within 320 km of the breach, for which grain sizes of individual boulders can be resolved with Google Earth imagery.

The largest boulder bar (>1.5 km length) occurs near the inside of a meander bend on the Po River. Deposition and point bar formation may be expected at the inside of bends under background discharge conditions. However, the critical stress required for incipient motion of the large boulders on its surface (~4.6 kPa for 5-meter median intermediate axis; calculations of the shear stress for incipient motion follow Lamb et al., 2008a; supporting information equations (9) and (10)) is extremely high, even compared to observations of other outburst floods (e.g., Lamb and Fonstad, 2010). Landsat 7 imagery from before and after the flood, as well as our simulation results, show that the flood inundated this feature, and simulated stresses at the upstream end of the bar exceed the critical stress for incipient motion of 5-meter blocks (**Figure 1.7c,d; Video A6**). Stress decreases downstream across the bar to values below this threshold for motion, and the stress gradient persists across the boulder bar for >10 hours as stress magnitude wanes. Despite the boulder bar's position near the inside of a channel bend, the large particle sizes and scale of the feature suggest a direct link to outburst floods. We also observed 75 large boulder bars along the pathway that are not located on the inside of meander bends (BoulderBar.kmz). The Siang River boulder bar in **Figure 1.7e-h** is typical of this dataset, similar in scale and particle size to the other 66 mapped bars within 320 km of the breach. Simulated flood shear stresses just upstream of this bar exceed the critical stress required for incipient motion (~1.6 kPa) of the median intermediate axis size boulder measured here (3 m) (**Figure 1.7f, g**), and show similar spatial and temporal stress variations as the Po River boulder bar. Bar deposition may be related to complex spatial and temporal variability in hydraulics and transport capacity; nevertheless, our results suggest the magnitude of flood shear stresses is of the right order to be consistent with transport and deposition of the observed size boulders.

Valley topography produces spatial gradients in bed shear stress during outburst floods that we suggest drive deposition of boulder bars that cannot be moved by lower-magnitude background flows, with implications for erosion. Boulder deposition armors the bed, limiting incision in specific locations during non-flood flows (Sklar and Dietrich, 2004; Turowski et al., 2007). Boulder deposition increases channel roughness, extracting momentum from the flow (Chatanantavet and Parker, 2008), further limiting the capacity of the river to transport sediment, expose the bed, and incise in these locations. Increased channel roughness due to boulder bar deposition may also potentially facilitate lateral erosion (Fuller et al., 2014). The hydraulics of infrequent, high-magnitude floods may therefore exert a strong control on channel incision and development of channel width and the river longitudinal profile. Taken together, our observations highlight the potential for background discharges and outburst floods of different sizes to promote not only different amounts, but different patterns of bedrock erosion (Reid et al., 2018).

1.7 CONCLUSIONS

We combined field and remote sensing observations with 2D numerical flood simulations to study the hydraulics and geomorphic impact of a large landslide-dam outburst flood. Simulated hydraulics of the flood, assuming instantaneous dam failure and a range of Manning's *n* values suitable for natural bedrock channels, are consistent with geomorphic observations of erosion and deposition along >450 km of the flood pathway through the eastern Himalaya. Inundation patterns are consistent with high-water marks >240 km downstream of the breach when we account for monsoon stage at the time of the flood. The accuracy of inundation patterns simulated for this extreme flood over hundreds of kilometers through rugged topography shows that the shallow water equations implemented within GeoClaw can aid in studies of flood hazard, paleoflood reconstruction, and geomorphic processes.

Our proof-of-concept integration of GeoClaw simulations and observations of the Eastern Himalaya provides insights into the control of extreme flood hydraulics on deposition and erosion. Results indicate that the timing and elevation of slackwater sand deposition with respect to peak flood stage vary significantly among the Yigong flood deposits. This finding highlights the potential for slackwater sand deposit elevation to significantly underestimate peak stage, and suggests prehistoric slackwater deposits cannot be correlated based on deposit elevation and simulated inundation patterns in the absence of independent provenance and/or geochronologic constraints. Our flood simulations and observations also provide strong evidence that outburst floods formed numerous large boulder bars along the Tsangpo Gorge and Siang River. We propose that these flood-related deposits armor the bed, increase roughness, and inhibit incision in zones where the interaction of annual flows with topography would not predict boulder deposition.

Immediately downstream of the breach and near valley constrictions in the Tsangpo Gorge and Siang River, simulated shear stresses exceeded the threshold for plucking of meter-scale blocks for multiple hours during the flood. This finding supports the idea that outburst floods may accomplish significant vertical incision into jointed bedrock in detachment-limited reaches of these valleys. However, shear stresses are spatially heterogeneous and vary by a factor of five over distances of less than a kilometer in the Tsangpo Gorge, underscoring the difficulty of equating the length-scale of block plucking with the length-scale of bed incision during an outburst flood. The observation that zones of sustained high shear stress outside the Tsangpo Gorge are associated with valley constrictions points to the potential importance of valley morphology above the channel in controlling outburst flood hydraulics. Future modeling studies are needed to explore the relationship between valley form and hydraulics for different magnitude flows, including Quaternary glacial-lake megafloods through the Tsangpo Gorge. Together with more sophisticated investigation of the interaction of flow hydraulics with slope stability, such work can help quantify how patterns and processes of lateral erosion and incision vary with flood magnitude.

Chapter 2. PROVENANCE AND EROSIONAL IMPACT OF QUATERNARY MEGAFLOODS THROUGH THE YARLUNG-TSANGPO GORGE FROM ZIRCON U-PB GEOCHRONOLOGY OF FLOOD DEPOSITS, EASTERN HIMALAYA

Holocene and late-Pleistocene sediments in the eastern Himalayan syntaxis represent an extraordinary record of glacial outburst megafloods in one of the most tectonically active landscapes on Earth. Glacial damming and outburst floods in the syntaxis may have focused erosion in the steep Tsangpo Gorge and inhibited river incision into the margin of the Tibetan Plateau. However, few flood slackwater deposits have been studied, and it is unknown which of the hundreds of known glacial impoundments in Tibet may have sourced the floods. Here we report n=1438 new detrital zircon U-Pb data from individual ancient megaflood and historical outburst flood slackwater deposits to examine the provenance and erosive potential of these events. Zircon data from megaflood deposits show that most of the recorded megaflood events were sourced from impoundments in the Yarlung River drainage at or to the west of the Namche Barwa massif located in the heart of the syntaxis, rather than from eastern sources along the Yigong and Parlung Rivers. Despite differences in zircon age distributions due to flood source area, the megaflood samples overall contain a disproportionate amount of zircons eroded from the Tsangpo Gorge compared to modern Siang River sediments; deposits from outburst floods that occurred in 1900 and 2000 on the Yigong River indicate that this signal cannot be explained by sediment reworking. Our findings show that nine of the eleven recorded megaflood events preferentially eroded the Gorge—supporting the hypothesis that Quaternary megafloods may have contributed substantially to rapid exhumation of the Eastern Himalayan syntaxis.

2.1 INTRODUCTION

The role of extreme events such as earthquakes, landslides, and outburst floods in long-term erosion and landscape evolution on Earth and on Mars is debated (e.g., Ouimet et al., 2007; Lamb et al., 2008; Lamb and Fonstad, 2010; Lang et al., 2013; Perron and Venditti, 2016; Larsen and Lamb, 2016; Margold et al., 2018). Bedrock rivers respond to perturbations in climate and tectonics to drive landscape evolution (Whipple et al., 2013), and recent work has highlighted important connections between outburst floods of different magnitudes, bedrock incision, lateral erosion, and hillslope processes (Turowski et al., 2008; Larsen and Montgomery, 2012; Beer et al., 2017; Langston and Tucker, 2018; Turzewski et al., 2019). However, we lack direct observations of the largest magnitude flood events on Earth and must rely on numerical simulations and information about these events stored in the sediments on the landscape.

The eastern Himalaya contains a rich geomorphic and sedimentary record of outburst floods in its rugged landscape (**Figure 2.1**). Widespread geomorphic evidence records glacial damming (e.g., Montgomery et al., 2004; Liu et al., 2006, 2015, 2018; Guangxiang and Xitao, 2007; Korup and Montgomery, 2008; Kaiser et al., 2010; Guangxiang and Qingli, 2012; Song, 2013; Zhu et al., 2013, 2014; Huang, 2014; Chen et al., 2016; Hu et al., 2018), and outburst megafloods with discharges >10^6 m^3/s sourced from such impoundments in Tibet (Montgomery et al., 2004; O'Conner et al., 2013; Srivastava et al., 2017). In addition to experiencing high peak annual flows (10^4 m^3/s; Goswami, 1985), rivers in the region also experience century-scale landslide-dam outburst floods (10^5 m^3/s; Delaney and Evans, 2015), resulting in a high capacity for erosion throughout the Holocene and Late Pleistocene (e.g., Larsen and Montgomery, 2012; Lang et al., 2013; Turzewski et al., 2019). Sediment eroded from the Himalaya during megafloods includes biospheric particulate organic carbon that is deposited and buried in the Bay of Bengal, making these events relevant to the global carbon budget in one of the largest river deltas in the world (Galy and Eglinton, 2015).

Previous workers have dated detrital zircons deposited by megafloods, outburst floods, and modern rivers, representing discharges that vary over several orders of magnitude (Booth et al., 2004, 2009; Stewart et al., 2008; Enkelmann et al., 2011; Lang et al., 2013; Lang and Huntington, 2014). Lang et al. (2013) used statistical analyses of detrital zircon U-Pb data from four megaflood slackwater deposits (n=450) to suggest that megafloods have a different signature of erosion on the landscape than modern river flows: forward models that mix zircon ages from possible upstream sediment sources suggest that megafloods disproportionately eroded more sediment from the steep Tsangpo Gorge in the heart of the syntaxis compared to background river discharges and a historical landslide-dam outburst flood on the Yigong River (Shang et al., 2003; Evans and Delaney, 2011; Xu et al., 2012; Delaney and Evans, 2015). This intriguing result highlights the potentially important role of megafloods in long-term river evolution and exhumation, but also raises questions about the sources of the ancient flood events and variability among individual event deposits.

We investigate megaflood sources and the role of these events in preferential erosion of the Tsangpo Gorge by constraining the provenance of detrital zircons in megaflood deposits in the Siang River valley, Arunachal Pradesh, northeastern India. We report n=1438 new zircon U-Pb age data from modern/historical outburst flood and megaflood slackwater deposits. We combine these data with previously reported zircon ages for flood and fluvial deposits and source regions within the Siang-Brahmaputra drainage to examine the role of impoundment location and sediment recycling in megaflood deposit zircon age distributions; constrain potential flood source regions in Tibet; and evaluate the hypothesis that compared to modern river flows, Quaternary megafloods preferentially focused erosion in the Tsangpo Gorge.

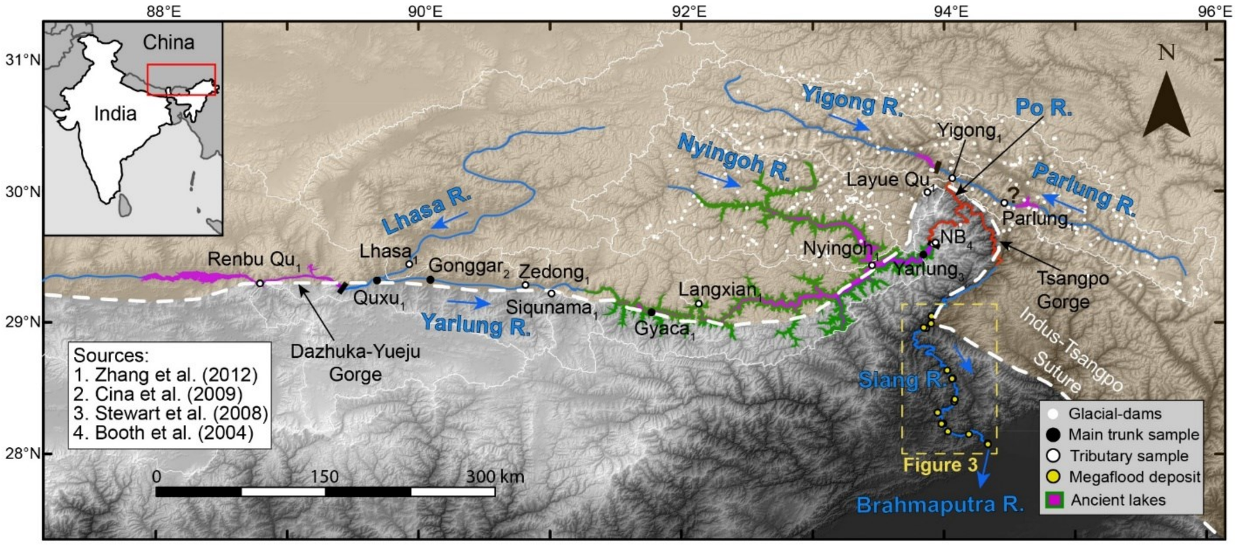

Figure 2.1. Location of study area and samples

Location map of study area as a hillshade over topography (SRTM3 digital elevation model) showing previous detrital samples in the Yarlung River basin including main trunk samples (Cina et al., 2009; Zhang et al., 2012), tributary samples (Zhang et al., 2012), bedrock (Booth et al., 2004) and ancient megaflood deposits (Lang et al., 2013; this study). The Yarlung River feeds into the Tsangpo Gorge (red) from the west and the Yigong and Parlung Rivers feed into the gorge through the Po River from the north.

2.2 BACKGROUND

2.2.1 *Potential source regions of megafloods through the Eastern Himalaya*

Megafloods through the Tsangpo Gorge could have been sourced from any of hundreds of paleo-lake impoundments that have been mapped upstream in Tibet (**Figure 2.1**; Korup and Montgomery, 2008; Korup et al., 2010). The rugged pathways of the Yarlung and Po Rivers meet in between the peaks of Gyala Peri (7294 m.a.s.l.) and Namche Barwa (7782 m.a.s.l.) in the Tsangpo Gorge (**Figure 2.1**). The Yigong and Parlung Rivers are upstream of this confluence to the northeast; upstream of this confluence to the west, the Yarlung River drainage contains an extensive network of tributaries including the Nyingoh and Lhasa Rivers (**Figure 2.1**). In this paper, we refer to glacial-lake impoundments to the northeast of the Namche Barwa massif on the Yigong and Parlung Rivers as eastern Tibetan sources, and impoundments at and to the west of Namche Barwa on the Yarlung River as western Tibetan sources.

Several Holocene and late-Pleistocene impounded paleolakes have been documented on the Yarlung River, representing potential western Tibetan sources for megafloods that would have traveled through the Tsangpo Gorge and into the Siang River valley in India (Montgomery et al., 2004; Liu et al., 2006; Korup and Montgomery, 2008; Kaiser et al., 2010; Song, 2013; Zhu et al., 2013; Zhu et al., 2014; Huang, 2014; Liu et al., 2015; Chen et al., 2016; Hu et al., 2018; Liu et al., 2018). Impoundment of the Yarlung River immediately upstream of Namche Barwa produced at least two lakes during the last 13 ka (**Figure 2.1**). Holocene lake terraces dated at 1160-1574 cal yr B.P. correlate to glacial-moraine dams near the entrance of the Tsangpo Gorge at Namche Barwa, recording a ~81 km^3 paleolake, the failure of which produced a flood with an estimated peak discharge of $1x10^6$ m^3/s (Montgomery et al., 2004). A second set of terraces dating to 9,997- 11,285 cal. yr B.P. may correspond to a larger, 835 km^3 reconstructed lake thought to have produced an estimated peak discharge of $5x10^6$ m^3/s in a catastrophic flood (Montgomery et al., 2004). However, other terraces in the area show that this larger lake may have existed in several stages at different maximum elevations (Montgomery et al., 2004; Liu et al., 2006; Zhu et al., 2013; Huang et al., 2014), and various dated lacustrine sediments up to 75 kyr B.P. are difficult to correlate to one another (Zheng et al., 2003, 2004; Montgomery et al., 2004; Liu et al., 2006, 2015; Huang et al., 2014).

Further upstream and to the west in the middle reaches of the Yarlung River there is evidence of a prolonged glacial-impoundment (32.3 to 13.2 cal. kyr B.P.) and resulting flood above the Dazhuka-Yueju Gorge (Kaiser et al., 2010; Zhu et al., 2013; Hu et al., 2018; **Figure**

2.1). The catastrophic failure of this lake is supported by field evidence of coarse gravels and boulders near the Dazhuka-Yueju Gorge (Hu et al., 2018); estimates of the timing of a flood include constraints from luminescence (12.8 to 13.5 ka; Kaiser et al., 2010; Zhu et al., 2013; Hu et al., 2018) and radiocarbon dating (13.2 kyr B.P.; Hu et al., 2018) of the topmost lacustrine sediments, and may be related to warming in the region during the due to the Bølling-Allerød period (Carling et al., 2002; Hu et al., 2018).

Hundreds of potential glacial-moraine dams have been mapped on eastern Tibetan tributaries of the Yigong and Parlung Rivers upstream of the Po-Tsangpo Gorge (**Figure 2.1**; Korup and Montgomery, 2008; Korup et al., 2010). However, paleo-lake sediments representing potential eastern Tibetan megaflood sources are sparse. Evidence of lake impoundment here is limited to a few lacustrine terraces identified on the Parlung River, which date from 16.1 to 22.5 kyr B.P. (Guangxiang and Xitao, 2007; Guangxiang and Qingli, 2012).

It is unknown whether ancient slackwater flood deposits downstream of the Tsangpo Gorge along the Siang River valley (**Figure 2.2**) record megaflood events sourced from these eastern Tibetan impoundments and/or western Tibetan sources in the Yarlung River drainage at or upstream of the Namche Barwa massif. Here we exploit variations in zircon U-Pb age distributions for different source regions in Tibet to address this question.

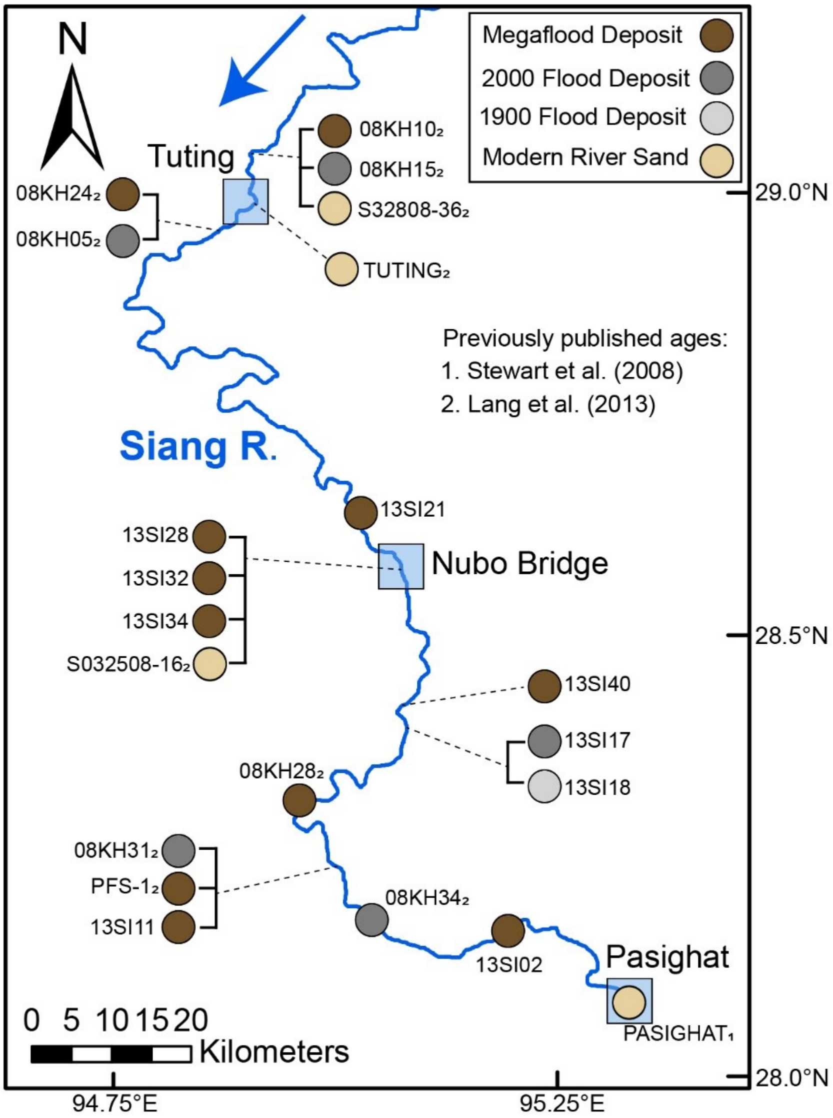

Figure 2.2. Location of detrital samples on the Siang River

Diagram of the Siang River pathway in northeast India showing the location of previous slackwater samples (Stewart et al., 2008; Lang et al., 2013) and samples collected in this study.

2.2.2 *Constraints on source-region zircon U-Pb ages*

Collision of the Indian and Eurasian plates since the early Eocene has resulted in tectonic terrains that produce distinct patterns of zircon crystallization ages in bedrock eroded by the Siang-Brahmaputra River system (Booth et al., 2004; Booth et al., 2009; Cina et al., 2009; Gehrels et al., 2011; Lang et al. 2014). Of the detrital zircon ages that characterize bedrock of this region, the less than ~1000 Ma ages (**Figure 2.3, Table 2.1**) include contributions from Himalayan zircons (~300-750 Ma, with a peak probability density at ~500 Ma; Stewart et al., 2008; Cina et al., 2009; Amidon et al., 2005); anatectic zircons from Himalayan rock of the Namche Barwa massif/Tsangpo Gorge specifically (<30 Ma; Booth et al., 2009); and Tibetan zircons (<300 Ma; Cina et al., 2009; Zhang et al., 2012). Aspects of the long-term evolution of this drainage system are still in question (e.g., Wang et al., 2014; Zhang et al., 2016), but the course of the Yarlung River through these rocks was established in the early Miocene (Lang and Huntington, 2014; Bracciali et al., 2015). Therefore, zircon U-Pb age distributions from megaflood samples can be a tracer of sediment sources and erosion patterns over the Quaternary.

Table 2.1. Previous detrital samples in the Yarlung River basin

Sample name	Location Lat	Location Lon	Size (n)	Reference
	[DD]	[DD]		
Quxu	29.3193	90.6864	77	Zhang et al., 2012
Gonggar	29.3228	91.0921	340	Cina et al., 2009
Gyacca	29.0747	92.7748	78	Zhang et al., 2012
Yarlung R.	29.3228	91.0921	163	Stewart et al., 2008
Renbu Qu	29.2959	89.7952	95	Zhang et al., 2012
Lhasa	29.4426	90.9315	86	Zhang et al., 2012
Zedong	29.2837	91.8158	84	Zhang et al., 2012
Siqunama	29.219	92.0144	103	Zhang et al., 2012
Langxian	29.141	93.135	84	Zhang et al., 2012
Nyingoh	29.4333	94.4543	91	Zhang et al., 2012
Namche Barwa Cirque	29.60642	94.93687	129	Booth et al., 2004
Layue Qu	29.9888	94.875	89	Zhang et al., 2012
Yigong R.	30.0967	95.0647	116	Zhang et al., 2012
Parlung R.	29.9084	95.4606	94	Zhang et al., 2012

Previously published detrital zircon data from the region (n=2299) are summarized in **Figure 2.4, Figure 2.3, Table 2.1,** and **Table 2.2**. Western Tibetan sources are characterized by previously published detrital zircon ages from the main trunk of the Yarlung River and its tributaries (**Figure 2.3**). Detrital samples from the main trunk Yarlung River west of the Tsangpo Gorge are generally dominated by a narrow ~50 Ma age peak representing Paleogene plutonic rocks (Zhang et al., 2012); a few 100-220 Ma zircons sourced from Cretaceous to late Triassic volcanic and sedimentary rocks and a minor component of 400-750 Ma zircons from Paleozoic to late Proterozoic rock of the Greater Himalayan Sequence south of the Indus-Tsangpo suture (Stewart et al., 2008; Zhang et al., 2012). Age distributions of tributaries to the Yarlung River farther upstream in the middle reaches of the drainage are more variable, and generally contain age peaks <250 Ma as well as contributions of ~500-750 Ma zircons plus or minus other age components. Zircon ages from the Tsangpo Gorge and Namche Barwa massif have a peak at (1) ~27 Ma, representing anatectic zircons that are distinguished by their ≤30 Ma ages and high U/Th ratios; and (2) ~490 Ma (range ~350-550 Ma), representing Himalayan ages (Booth et al., 2004, 2009; Zhang et al., 2012). Zircons from tributaries entering the Gorge through the Po River from eastern Tibetan sources are mostly ~100-220 Ma in age, with some ~45-75 Ma and few >220 Ma zircons.

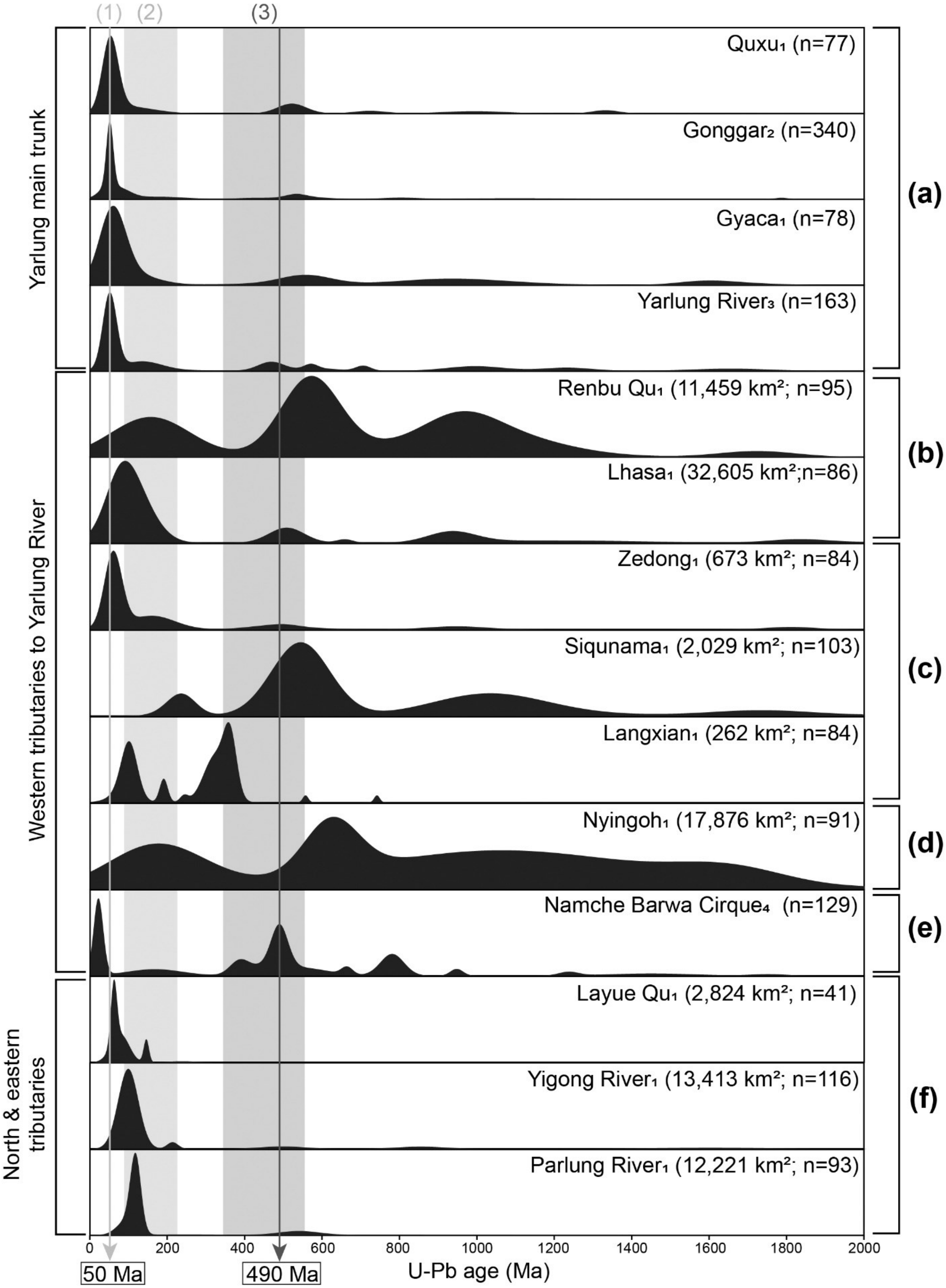
(1)
(2)
(3)
Quxu₁ (n=77)
Gonggar₂ (n=340)
Gyaca₁ (n=78)
Yarlung River₃ (n=163)
Renbu Qu₁ (11,459 km²; n=95)
Lhasa₁ (32,605 km²;n=86)
Zedong₁ (673 km²; n=84)
Siqunama₁ (2,029 km²; n=103)
Langxian₁ (262 km²; n=84)
Nyingoh₁ (17,876 km²; n=91)
Namche Barwa Cirque₄ (n=129)
Layue Qu₁ (2,824 km²; n=41)
Yigong River₁ (13,413 km²; n=116)
Parlung River₁ (12,221 km²; n=93)
Yarlung main trunk
Western tributaries to Yarlung River
North & eastern tributaries
(a)
(b)
(c)
(d)
(e)
(f)
0
200
400
600
800
1000
1200
1400
1600
1800
2000
50 Ma
490 Ma
U-Pb age (Ma)

Figure 2.3. Zircon age distributions of source region samples

Zircon age distributions of previous detrital samples shown on kernel density estimate (KDE) plots including main trunk, tributary, and bedrock samples (a-f). Line (1) represents the age peak at ~50 Ma that is characteristic of the Yarlung River source samples (a), and the blue line at (2) represents the age peak at ~490 Ma that is characteristic of Namche Barwa bedrock. Sources for detrital samples include: Zhang et al. (2012)$_1$, Cina et al., (2009)$_2$, Stewart et al., (2008)$_3$. A single bedrock sample is sourced from Booth et al., (2004)$_4$.

2.2.3 *Previous detrital zircon U-Pb dating of slackwater deposits on the Siang River*

Detrital samples downstream of the Tsangpo Gorge from the Siang River in northeastern India integrate the Tibetan and Himalayan source age distributions described above (**Figure 2.2, Figure 2.4**). Most zircons from samples representative of the modern Siang River are distributed around 50 Ma and 350-550 Ma (Stewart et al., 2008; Lang et al., 2013). These authors argued that the large proportion of 350-550 Ma zircons (~47 %) from just 2% of the total upstream drainage localized around the Tsangpo Gorge reflects extreme erosion and sediment evacuation by the modern river focused in the Gorge area.

Zircon age distributions of slackwater deposits from the 2000 Yigong River landslide-dam outburst flood sampled up to 30 m above the Siang River channel by Lang et al. (2013) differ somewhat from those of modern Siang River sediments (**Figure 2.4**). The youngest age peak in the 2000 Yigong flood deposit sample compilation is ~66 Ma, older than the ~50 Ma peak that characterizes Yarlung River source samples and modern Siang River detritus. The Yigong flood deposits also contain 350-550 Ma Himalayan-age zircons like the modern Siang River samples, and ~100-220 Ma zircons representing the Yigong River age signature (**Figure 2.3**).

Zircon ages populations from four ancient megaflood slackwater deposits sampled up to 150 m above the modern Siang River channel by Lang et al. (2013) (n=450) contain more ~350-550 Ma zircons that are characteristic of the Tsangpo Gorge compared to the modern Siang

River and 2000 Yigong flood samples (**Figure 2.4**). Based on forward mixture modeling of these previously data, Lang et al. (2013) argued that megafloods disproportionately focused erosion in the Tsangpo Gorge compared to these smaller magnitude flows.

We explore potential megaflood source areas and test the hypothesis that ancient megaflood sediments preferentially eroded material from the Tsangpo Gorge compared to smaller flows by combining previous data with new analyses from additional megaflood deposits and deposits from the 1900 and 2000 Yigong River outburst floods—and use the combined dataset of over 4100 detrital zircon U-Pb ages explore the potential influence of flood provenance, erosion, and sediment recycling, on detrital age signals.

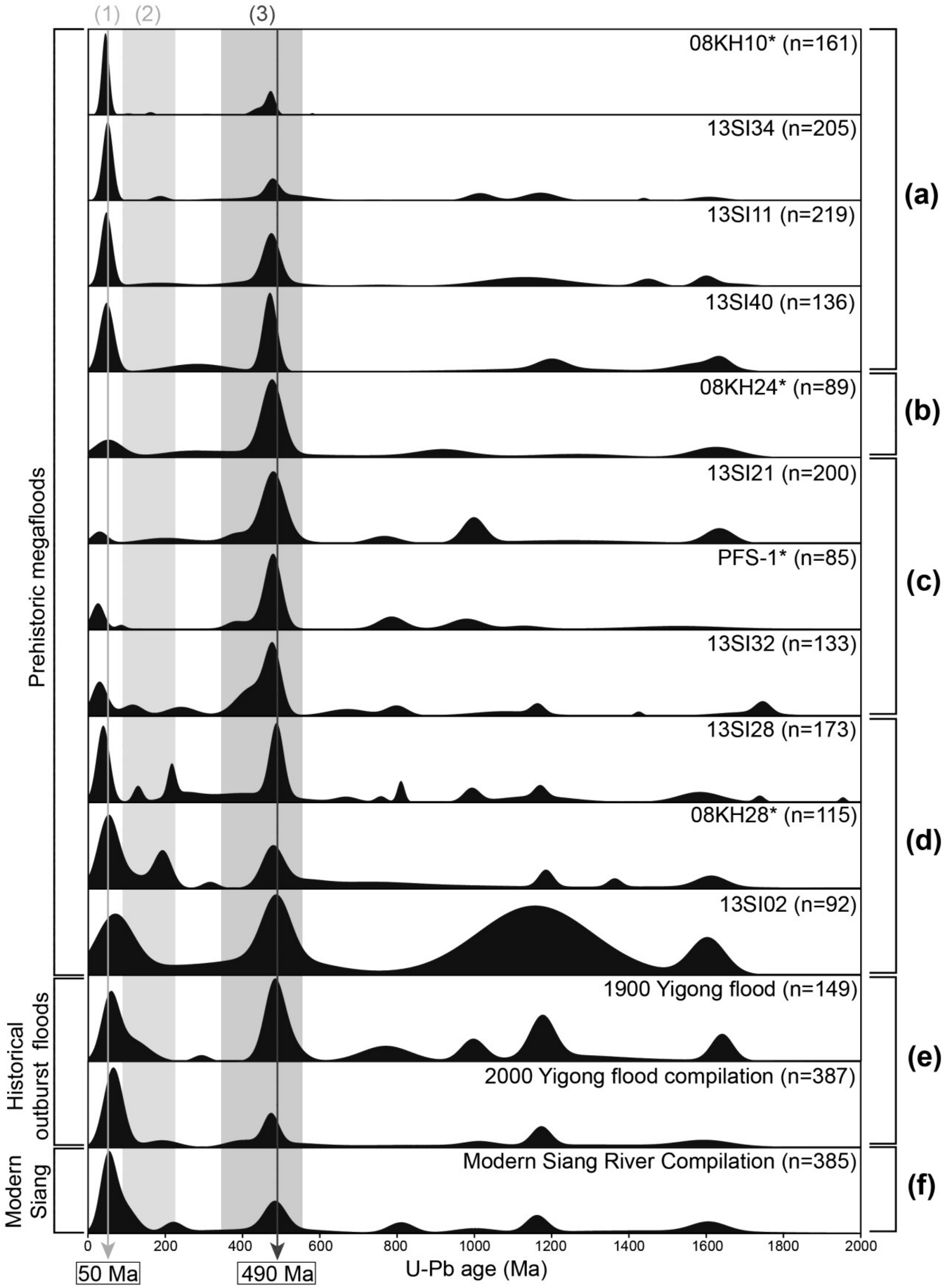
(1)
(2)
(3)
08KH10* (n=161)
13SI34 (n=205)
13SI11 (n=219)
13SI40 (n=136)
08KH24* (n=89)
13SI21 (n=200)
PFS-1* (n=85)
13SI32 (n=133)
13SI28 (n=173)
08KH28* (n=115)
13SI02 (n=92)
1900 Yigong flood (n=149)
2000 Yigong flood compilation (n=387)
Modern Siang River Compilation (n=385)
(a)
(b)
(c)
(d)
(e)
(f)
Prehistoric megafloods
Historical outburst floods
Modern Siang
0
200
400
600
800
1000
1200
1400
1600
1800
2000
U-Pb age (Ma)
50 Ma
490 Ma

Figure 2.4. Zircon age distributions of detrital samples collected

Zircon age distributions of previous (4) ancient megaflood deposits (starred; Lang et al., 2013), (7) new ancient megaflood deposits (this study), new 1900 Yigong flood sample (this study), 2000 Yigong flood compilation (Lang et al., 2013; this study), and the previous modern river sample compilation (Stewart et al., 2008; Lang et al., 2013).

2.3 METHODS

2.3.1 *Slackwater flood deposit identification and sample collection*

The n=1438 new detrital zircon U-Pb data reported here come from two historical landslide-dam outburst flood samples, one reported here for the first time and one described by Turzewski et al. (2019), and seven new ancient megaflood samples described here for the first time (**Figure 2.2; Table 2.2**). All samples were collected from exposed faces of outburst flood deposits in road cuts along the Siang River in northeast India during fieldwork performed in 2013. Sample locations for these deposits, as well as previously published samples of Lang et al. (2013) are shown in **Figure 2.2 and Table 2.2**.

Table 2.2. Detrital samples collected from the Siang River

Sample Name	Deposit type	Lat	Lon	Elevation	Number of analyses
		[DD]	[DD]	[m]	n
13SI02	Megaflood	28.1533	95.19072	555	92
13SI11	Megaflood	28.23355	94.98277	271	215
13SI40	Megaflood	28.41904	95.08376	309	135
13SI28	Megaflood	28.5763	95.06302	427	164
13SI32	Megaflood	28.57915	95.06281	400	133
13SI34	Megaflood	28.57959	95.06693	360	200
13SI21	Megaflood	28.63944	95.02667	394	200
08KH10[1]	Megaflood	29.051366	94.906178	502	161
08KH24[1]	Megaflood	28.965522	94.847082	553	89
08KH28[1]	Megaflood	28.317589	94.95328	353	115
PFS-1[1]	Megaflood	28.233917	94.983443	270	85
13SI17	1900 Yigong flood	28.40177	95.07956	278	149
13SI18	2000 Yigong flood	28.40177	95.07956	279	131
08KH34[1]	2000 Yigong flood	28.173515	95.030536	199	42
08KH31[1]	2000 Yigong flood	28.235035	94.996516	230	113
08KH05[1]	2000 Yigong flood	28.960825	94.865067	466	44
08KH15[1]	2000 Yigong flood	29.048683	94.910801	475	57
SC03-26-08-(6)[2]	Modern Siang River	28.0768	95.3356	156	137
S032508-16[1]	Modern Siang River	28.576655	95.070195	264	88
TUTING[1]	Modern Siang River	28.996279	94.903436	425	58
S032808-36[1]	Modern Siang River	29.048474	94.910787	449	73

Note: previous detrital samples include Lang et al., (2013)[1]; Stewart et al., (2013)[2]

Flood deposits were distinguished from fluvial and landslide deposits based on their sedimentary features and position, following Lang et al. (2013) and Turzewski et al. (2019). We observed fluvial deposits near the river level at the time of fieldwork that had sedimentary structures like cm-scale cross-beds indicating bedload transport (**Figure B1**), but we avoided sampling these deposits and restricted sampling to laminated slackwater flood deposits indicating deposition from suspension. Ancient flood deposits are exposed in roadcuts above the Siang River and near major tributaries that inundate during floods. One slackwater deposit from the 2000 Yigong flood that was identified in a previous field season was observed in 2013 to have been covered by a small landslide, illustrating a mechanism by which ancient flood deposits may be preserved in this rapidly eroding landscape. In several locations, deposits from multiple megaflood events were located in stratigraphic succession, in some cases separated by landslide deposits.

We analyzed zircons from two slackwater flood deposits interpreted to represent deposition from historical landslide-dam-break outburst floods on the Yigong River (e.g., Delaney and Evans, 2015). The 2000 Yigong flood sample (13SI18) was mapped by Turzewski et al. (2019) 48 m above the modern river at low flow. This deposit is composed of laminated fine to medium grain sand, shows no signs of soil development, and has small <0.5 m vegetation growth on top. Sample (13SI17) is from a laminated deposit with similar grain size, that is located on a surface 1-2 m lower in elevation than the 2000 flood deposit and is capped by thick vegetation including a ~40 cm diameter jackfruit tree that locals estimated to be around 50-70 years old (T. Tayeng, personal communication, 2013). The age of this tree and the characteristics of this deposit indicate it was deposited by the 1900 Yigong River outburst flood (**Figure B2**).

The seven new megaflood deposits (**Figure 2.2**) are located 72-381 m above the modern Siang River level at low-flow. The highest deposit (13SI02) exposure is approximately 90 m long and 6 m thick, making it the largest deposit identified in the field (**Figure B3**). Samples 13SI21 and 13SI40 are from deposits on terraces >70 m above the river level exposed in roadcuts and are 1-2 m thick (**Figure B4; B5**). The remaining samples are from vertical sequences of slackwater megaflood deposits separated by landslide colluvium (**Figure B6**). Three of the deposits (13SI28, 13SI32, 13SI34) are 96-163 m above the river on a series of terraces near Nubo Bridge, which was destroyed during the 2000 Yigong flood (**Figure B7; B8**). For reference, at this location, deposits from the 2000 Yigong flood are located at 35 m above the river level.

2.3.2 *Detrital zircon sample preparation and U-Pb geochronology*

About 1-2 kg of fine-medium grained sand from each sample was processed with standard mineral separation techniques. Samples were sieved to isolate the 80-250 μm size fraction, and minerals were separated with a Wilfley table, heavy liquids and a Frantz magnetic separator. Separated zircons from this size fraction were mounted, polished, and imaged with backscattered electron imaging (Hitachi 3400N SEM) at the University of Arizona. Zircon cores were analyzed for U-Th-Pb geochronology with laser ablation multi-collector inductively coupled mass spectrometry (LA-MC-ICPMS) using a 30 μm spot diameter at the Arizona LaserChron Center (Gehrels, 2011). U-Pb age data were reduced using NUPMagecalc and ISOPLOT using standard age filters. Additional information about preparation, analysis, and reduction of data is available in Pullen et al. (2014).

2.3.3 *Statistical analysis of detrital provenance*

We compared zircon U-Pb age distributions from the new and previously published samples using a variety of statistical methods. Zircon age distributions are presented as kernel density estimates (KDE) fitted with automatic selection of bandwidth (Botev et al., 2010). We also used multidimensional scaling (MDS) methods to quantify similarity among the age distributions of different samples (Vermeesch, 2013). This technique maps samples as points onto a two-dimensional map where similar samples cluster together and dissimilar samples plot far apart (Vermeesch, 2013). The distance between points in this mapping is measured as a KS statistic; solid lines between samples are plotted to indicate the nearest neighbor (“most similar”), whereas dotted lines represent the next most similar sample (Vermeesch, 2013). A ‘stress value’ (S) is calculated for the whole comparison that acts as a goodness-of-fit metric, where S=0.2 represents a poor fit and S=0 is a perfect fit (Vermeesch, 2013). This method has shown to be a useful tool for examining similarity in detrital datasets in a variety of geological applications (e.g., Vermeesch, 2013, 2015, 2017; Arboit et al., 2016; Kirkland, 2016; Licht et al., 2016; Spencer and Saylor et al., 2016; Xu et al., 2017; Makuluni et al., 2018; Wissink et al., 2018). Detrital provenance was further investigated using Bayesian inversion of zircon age distributions, which uses the information in the downstream detrital sample to search for age components and their characteristics (Gallagher et al., 2009; Jasra et al., 2006).

We used BayesMix software (Gallagher et al. 2009), which has been used previously to invert zircon U-Pb age distributions to distinguish tectonic terrains and analyze the provenance of loess and paleosol deposits (e.g. Filleaudeau et al., 2012; Licht et al., 2016; Perrot et al., 2017). BayesMix uses a reversable jump Markov chain Monto-Carlo (RJ-MCMC) sampling strategy to select the age, width, and number of individual components, and the proportion of each component present in sample age distributions (Gallagher et al., 2009; Jasra et al., 2006). We ran BayesMix with 20,000 iterations assuming heavy skew-t distributions for priors and compared the age, error, and proportion of all components from each sample. The inversion was performed on compilations of detrital zircon data from geologically equivalent deposits recording the same event/processes including five 2000 Yigong outburst flood deposits (n=387), and four modern Siang river samples (n=356). We performed inversions on a compilation of all 11 megaflood deposits (n=1608) and on sub-groups of similar megaflood samples.

2.4 RESULTS

2.4.1 *Detrital zircon UPb ages*

Zircon U-Pb data from the n=1438 new analyses presented here are available online in the GitHub repository at: https://github.com/zewski14/TurzewskiThesisData. **Figure 2.4** presents zircon age distribution KDEs for seven new and four previously reported megaflood samples (Lang et al., 2013); new 1900 Yigong flood sample; 2000 Yigong flood sample compilation (data from Lang et al. (2013) and sample 13SI18 from this study); and compilation of modern Siang River sample data (Stewart et al., 2008; Lang et al., 2013).

All megaflood deposits have a ~490 Ma age peak corresponding to the prominent age peak in the Namche Barwa/Tsangpo Gorge source sample (**Figure 2.3, Figure 2.4). **The relative magnitude of the ~490 Ma peak, as well as the position, width, and relative magnitude of the youngest age peak varies among deposits. Four of the megaflood deposits (group 1) have a youngest age peak at ~50 Ma (**Figure 2.4a, b**), corresponding to the youngest age peak observed in western Tibetan source samples along the main trunk of the Yarlung River (line 1 in **Figure 2.3**); a fifth sample (08KH24; **Figure 2.4b**) has a similar youngest age peak that is broader and relatively smaller than those of the other samples in group 1. Three of the deposits (group 2) have a youngest age peak (**Figure 2.4c**) that matches the ~27 Ma youngest age peak in the Namche Barwa source sample that represents anatectic zircons (**Figure 2.3**). Three deposits (group 3) have youngest age peaks in the ~25 to 65 Ma range and also contain prominent age peaks from ~100-220 Ma (**Figure 2.4d**) that may correspond to eastern Tibetan sources of the Yigong and Parlung Rivers or tributaries of the middle-reaches of the Yarlung River to the west (**Figure 2.3**).

The new 1900 Yigong flood sample and updated 2000 Yigong flood sample compilation share an age peak at ~490 Ma similar to the megaflood samples, but have a youngest age peak around ~66 Ma with positive skew toward older ages (**Figure 2.4e**). When the new megaflood sample data are combined with the previously published megaflood zircon data of Lang et al. (2013), the compiled dataset support the previous hypothesis that megaflood sediments contain more material from the Tsangpo Gorge (bar 3) compared to the modern Siang River and 2000 Yigong flood sample compilations (**Figure B9**).

2.4.2 *Evaluating similarity between samples and sources using MDS*

The MDS map (**Figure 2.5**) plots similarity among detrital samples representating source areas in Tibet and the Tsangpo Gorge, modern Siang River sediment and Yigong flood deposit data compilations, and individual megaflood deposits. The overall stress value of the map is 0.10283, between a fair and good fit to the data (Vermeesch, 2013). Consistent with the sample KDEs, the MDS map shows more overlap between the Yarlung, Yigong, and Parlung zircon distributions compared to the distribution from the Namche Barwa cirque sample—and supports that the Tsangpo Gorge detrital zircon signal is distinct from other sedimentary sources in the drainage. The modern Siang River and 2000 Yigong flood deposit compilations plot close together, reflecting the similarity of their KDEs. The 1900 Yigong flood sample is close to but not directly linked to the 2000 flood compilation, highlighting the potential for significant variability among detrital age distributions for very similar outburst flood events sourced from the same location.

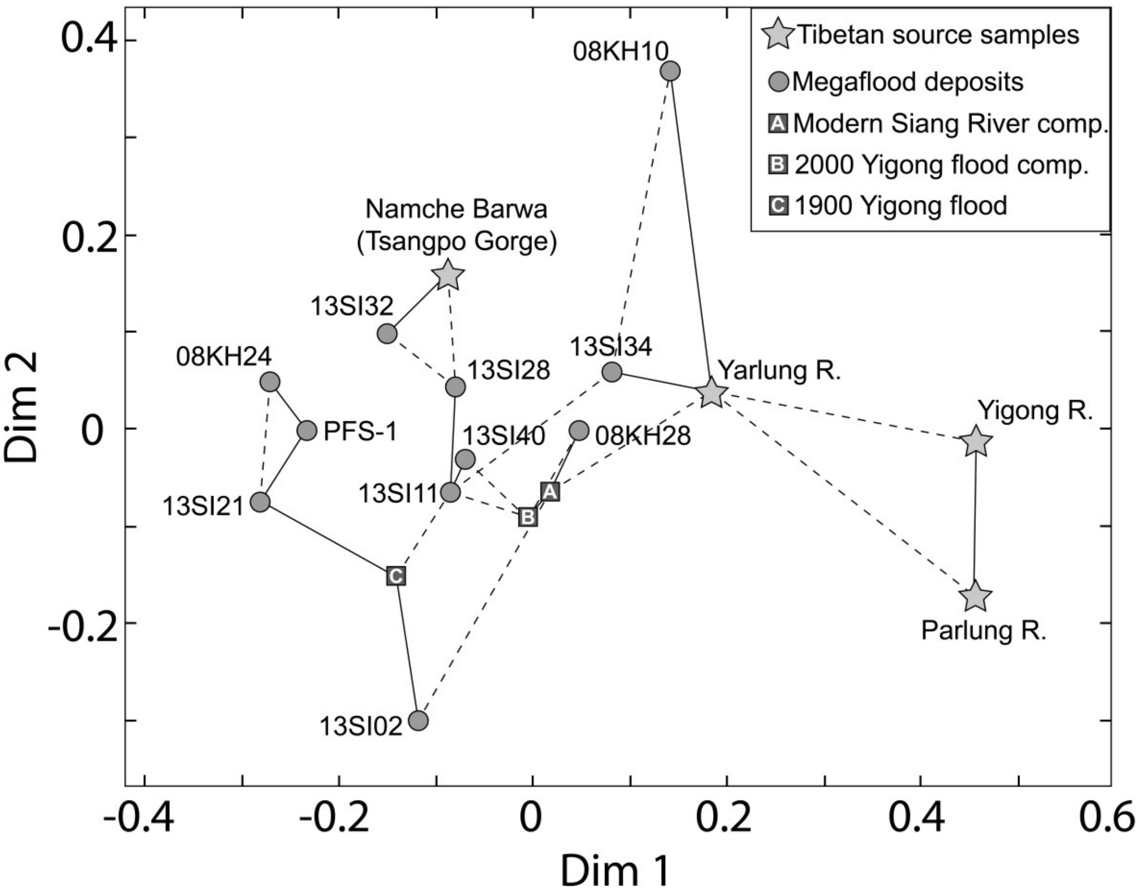

Figure 2.5. MDS map of zircon data

MDS map displaying similarity between four source samples used in previous studies (Yarlung River, Namche Barwa Cirque, Yigong, and Parlung Rivers), modern river and 2000 Yigong flood compilations, the 1900 Yigong flood sample, and all individual megaflood deposits (Stress value = 0.10283). Solid lines between samples represent the most similar neighbor, whereas a dotted line is the second most similar. The distance in the x and y direction on this plot between samples is in the unit of a KS statistic, so more dissimilar samples plot further apart on the 2D map.

Further insight from MDS analysis is limited. The MDS map is relatively insensitive to the positions of small age peaks observed in the different sample distributions. For example, samples 13SI32 and 13SI28 have prominent zircon age peaks from ~100-220 Ma, yet they plot nearest to the Namche Barwa source sample, which lacks these defined age peaks. In addition, comparing large and small *n* samples on an MDS map can be problematic (Vermeesch, 2015), so we evaluated the effects of sample size using a bootstrap approach. When we randomly remove

20% of the grains and re-compute the MDS map, we find in many iterations that the positions and connections among the samples vary. For example, a connection between PFS-1 and 13SI32 appears in several iterations (**Figure B10**) that is not present in the original map (**Figure 2.5**), yet we group these two samples based on the similarity of their KDEs (**Figure 2.4**). Together, these observations suggest the large difference in sample size between megaflood deposits and some source samples makes the MDS map of limited use for interpreting zircon provenance.

2.4.3 *BayesMix age component results*

BayesMix inversion (**Figure 2.6, Table 2.3**) identifies age components consistent with a ~50 Ma peak representing Tibetan source sediment in all sample compilations, but in varying proportions. The youngest age component in the modern Siang River and 2000 Yigong Flood sample compilations, respectively, represents 30-32% of the zircons, whereas the youngest component in the megaflood compilation represents 22% of the zircons. The next largest age components by proportion are consistent with ~350-550 Ma Himalayan ages from the Tsangpo Gorge area. Components in the 350-550 Ma range are identified in smaller proportions in the modern Siang River and 2000 Yigong flood compilations (23-24%) compared to the megaflood compilation (37%). The two age components in this range that are resolved in the megaflood compilation have means at 391 Ma and 475 Ma, corresponding to peaks in the Namche Barwa source sample. The BayesMix model identifies age components in the 50 to 350 Ma age range for the megaflood sample compilation that are not observed in the modern Siang River and Yigong flood deposit compilations.

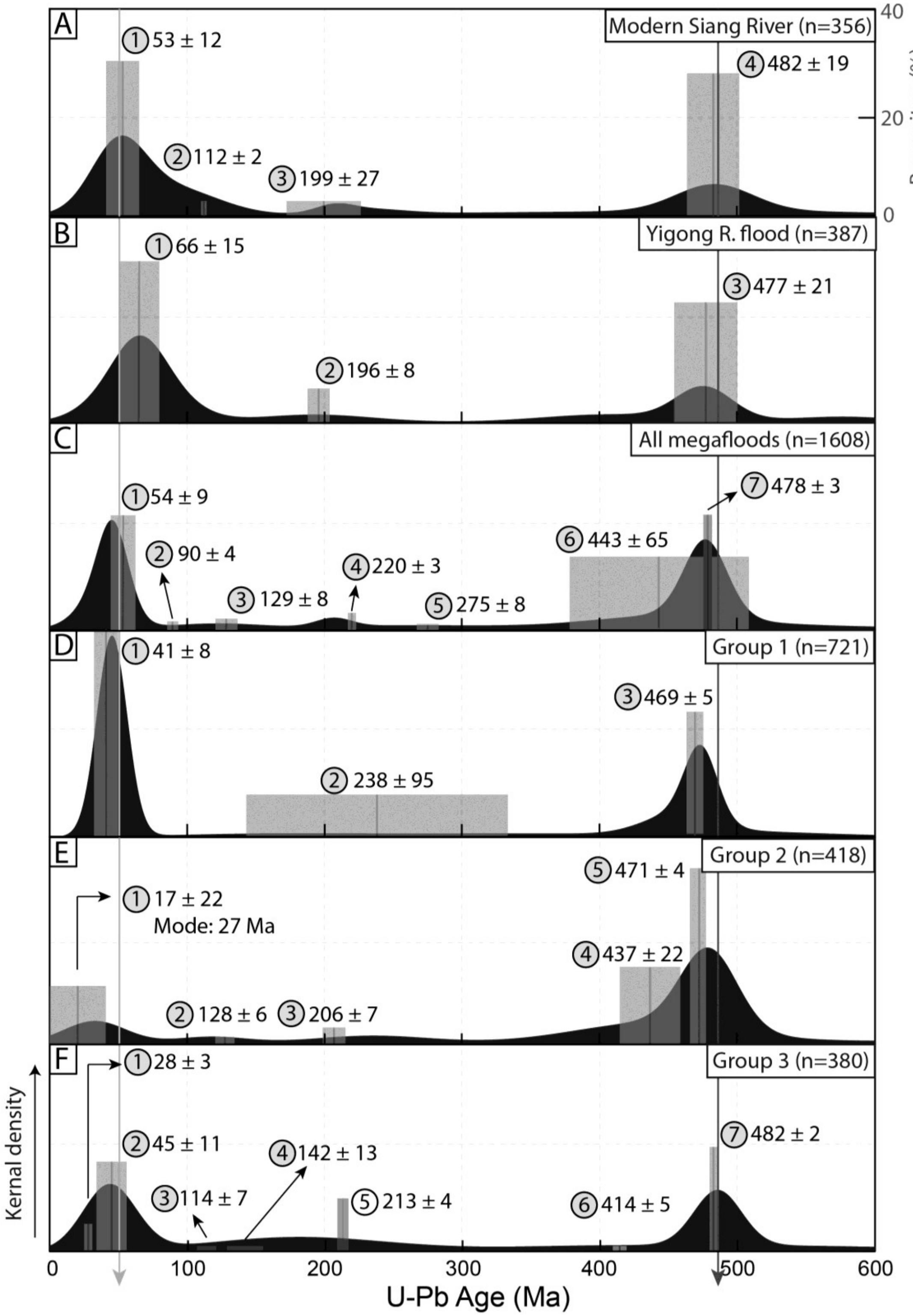

Figure 2.6. Results from the BayesMix inversion of sample compilations

Shown are the results from BayesMix inversion of the sample compilations that identifies different age components in the (a) modern sample, (b) 2000 flood sample compilation, (c) megaflood compilation, and the megaflood subgroups 1-3 (d-f).

BayesMix inversion of the zircon data for sample groups 1, 2 and 3 show differences in the position and magnitude of the age components in each group (**Figure 2.6, Table 2.3**). Prominent age components at ~41 Ma and ~45 Ma in group 1 and group 3 samples represent 40% and 17% of the zircons in each group, respectively; these age components overlap the diagnostic ~50 Ma peak from the Yarlung River source samples, although the positions of peaks in some individual samples varies and may be consistent with other sources. In contrast, the youngest age component in the group 2 samples comprising 11% of zircons with a mode at 27 Ma is consistent with the ≤30 Ma ages seen in the Namche Barwa source sample. The relative contribution from 350-550 Ma Himalayan rock from the Tsangpo Gorge area varies among individual samples, but on average these components make up 22-24% of zircons in groups 1 and 3, and 49% of group 2 zircons. Taken together, the BayesMix results highlight prominent Himalayan and Tibetan age components in the sample data, which we relate to zircon source areas below.

Table 2.3. Age components identified with BayesMix

Compilation	Modern river samples (n=356)			Yigong flood samples (n=387)			Megafloods (n=1608)			Group 1 (n=721)			Group 2 (n=418)			Group 3 (n=380)		
Sample names	*S32808-36,TUTING, S032508-16,PASIGHAT*			*08KH15,08KH05,08KH31, 08KH34,13SI17*			*08KH10,13SI34,13SI11,13SI40, 13SI02,13SI28,08KH28, 13SI32,13SI21,08KH24,PFS-1*			*08KH10, 13SI34, 13SI11, 13SI40*			*13SI21, PFS-1, 13SI32*			*13SI28, 08KH28, 13SI02*		
Component	Mean (Ma)	Error (Ma)	(%)	Mean (Ma)	Error (Ma)	(%)	Mean (Ma)	Error (Ma)	(%)	Mean (Ma)	Error (Ma)	(%)	Mean (Ma)	Error (Ma)	(%)	Mean (Ma)	Error (Ma)	(%)
1	53	12.6	30.0	66	15.7	31.8	54.8	9.5	22.4	41.6	8.6	40.0	17.9	22.6	11.7	28.2	3.4	5.2
2	112.1	2.4	3.4	196.5	8.6	6.3	90	4.6	0.7	238.6	95.4	8.7	128.0	6.7	0.7	45.2	11.9	17.1
3	199.4	27.2	3.6	477.1	21.3	23.1	129.6	8.4	2.1	469.1	5.1	24.7	206.4	7.9	3.0	114.1	7.5	1.3
4	482.2	19.6	24.0	766.2	7.8	1.9	220.1	3.2	3.5	978.9	10.0	4.2	437.0	22.3	15.7	142.2	13.4	1.2
5	817.1	7	6.8	1094.7	114.2	13.0	275	8.9	1.5	1214.1	9.6	8.8	471.9	4.5	34.8	213.9	4.7	10.2
6	1008.7	13.2	3.1	1151.3	31.9	8.8	443.1	65.3	14.8	1855.8	53.7	8.5	835.3	61.2	6.5	414.8	5.5	1.7
7	1155	6.9	12.6	1563.4	111.2	15.1	478.1	3.7	22.7	1619.7	5.1	3.6	991.4	4.7	6.9	482.1	2.4	20.3
8	1597.4	45.4	10.6	-	-	-	697.8	5.1	0.8	2494.9	64.9	1.1	1202.1	17.4	7.5	692.7	204.0	15.7
9	2900.9	12.2	4.1	-	-	-	834.1	4.3	3.6	2865.3	9.6	0.5	1305.4	7.0	0.1	1006.7	11.4	5.6
10	3227.1	8.1	0.6	-			1007.9	7.3	4.7	-	-	-	1726.2	57.0	13.2	1186.2	4.3	9.4
11	3529.2	24.4	1.2	-	-	-	1133.2	171.4	9.0	-	-	-	-	-	-	1349.6	43.4	5.5
12	-	-	-	-	-	-	1176	4.7	6.4	-	-	-	-	-	-	1608.8	33.7	5.2
13	-	-	-	-	-	-	1615.6	45.3	7.5	-	-	-	-	-	-	2849.5	15.7	0.1
14	-	-	-	-	-	-	2861.6	24.2	0.5	-	-	-	-	-	-	-	-	-

2.5 DISCUSSION

Here we interpret zircon data from 11 megaflood deposits in the context of the zircon age distributions from potential source areas in Tibet, modern Siang River sediments, and historical outburst flood deposits. Floodwaters may entrain impounded lake sediment, material eroded from the hillslopes and channel during the depositing flood event, and reworked sediment from previous flood/fluvial deposits along the flood pathway—recording contributions from each of these sources in the zircon age distributions they deposit. Most of the megaflood deposit age distributions indicate zircon provenance from areas at or to the west of Namche Barwa in the Yarlung River drainage, or from Himalayan rocks of the Tsangpo Gorge. These data (1) suggest most of the megafloods that produced the sampled deposits were sourced from impoundments at or to the west of Namche Barwa in the Yarlung River drainage, and (2) indicate preferential erosion of the Tsangpo Gorge area during most of the recorded megaflood events, supporting the hypothesis that megafloods may have contributed substantially to exhumation of the Gorge.

2.5.1 *Zircon provenance and constraints on megaflood sources*

There is widespread evidence of glacial-moraine dams in the eastern Himalaya, but it is unclear which potential sources of zircons are represented in the Siang River valley megaflood deposits. Lang et al. (2013) suggested that the megafloods that produced these deposits were sourced from glacially-impounded lakes in western Tibet because of the extensive record of lacustrine deposits on the Yarlung River adjacent to and upstream of Namche Barwa (Montgomery et al., 2004; Liu et al., 2006, 2015, 2018; Kaiser et al., 2010; Zhu et al., 2013, 2014; Huang et al., 2014; Chen et al., 2016). Recent observations of coarse sediments and bed forms in the middle-reaches of the Yarlung River provide evidence of megafloods sourced from impoundments even further to the west (Hu et al., 2018). Limited evidence also exists for paleolake deposits on the Yigong and Parlung Rivers in eastern Tibet (Guangxiang and Xitao, 2007; Guangxiang and Qingli, 2012), raising the question of whether megafloods were sourced from glacial impoundments in this area.

Outburst floods may be highly erosive at and immediately downstream of the dam breach (O'Connor and Beebee, 2009; Froehlich, 2016; Table, et al., 2018; Turzewski et al., 2019), entraining impounded lake sediment and/or dam, hillslope, and fluvial material near the source. Zircons from the dammed area may therefore be well represented in flood deposits downstream, as is observed for slackwater deposits of the 1900 and 2000 Yigong River floods (Lang et al., 2013; this study). Distinctive age peaks <250 Ma from potential megaflood source areas to the east and west of Namche Barwa in Tibet appear in varying proportions in the megaflood slackwater deposits, and have the potential to constrain the source areas of megafloods that produced the Siang River valley slackwater deposits.

Most of the megaflood deposits contain a strong western Tibetan source signature. The four megaflood deposits in group 1 (**Figure 2.4a**) and sample 08KH24 (**Figure 2.4b**) contain a prominent ~50 Ma peak characteristic of a Yarlung River source and generally lack other significant <600 Ma zircon peaks, except for the ~490 Ma Himalayan age component present in all flood deposits in this study. The three megaflood deposits in group 2 (**Figure 2.4c**) contain a significant proportion of zircons that appear to have been sourced from the Namche Barwa massif/Tsangpo Gorge specifically, with a peak at ~27 Ma and a very large contribution of zircons at 350-550 Ma (**Figure 2.3e**). Two of the group 3 deposits (08KH28, 13SI28; **Figure 2.4d**) also have prominent ≤ 50 Ma age peaks indicative of Yarlung catchment/Namche Barwa provenance. These clear Yarlung River and Namche Barwa zircon provenance signals provide strong evidence that all eight group 1 and 2 deposits, and two of the group 3 deposits, record megafloods sourced from impoundments at or to the west of Namche Barwa that would have traversed the Yarlung River pathway through the Tsangpo Gorge.

Only one of the megaflood deposits (13SI02) may be compatible with an eastern Tibetan flood source (**Figure 2.4d**). The youngest age peak at ~66 Ma and significant contribution of ~100-220 Ma zircons in deposit 13SI02 are similar to the zircon signals found in the Yigong and Parlung River source and the 1900 and 2000 Yigong flood samples and may be compatible with an impounded lake source to the east of Namche Barwa, although the age distribution of sample 13SI02 is poorly resolved. The other two group 3 deposits that show a significant contribution of ≤ 50 Ma zircons indicative of Yarlung catchment/Namche Barwa provenance (08KH28, 13SI28) also contain zircons in the ~100-220 Ma age range, which may be consistent with eastern Tibetan sources and/or flood-transported or reworked sediment that originated in the middle reaches of the Yarlung River. However, given that the youngest zircon age peak in these samples is significantly younger than 66 Ma, the impoundments that sourced the depositing floods were likely located west of Namche Barwa in the Yarlung drainage.

Diagnostic age peaks from multiple flood source areas are present in most of the flood deposits, showing the extent to which outburst floods rework previous flood and/or fluvial deposits. The 2000 Yigong flood deposit data show that a flood sourced from this eastern Tibetan tributary impoundment contains ~100-220 Ma zircons that characterize the eastern tributary source regions as well as ~50 Ma zircons characteristic of western Tibetan sources, similar to modern Siang River sediment (**Figure 2.4e,f**). Several of the group 1 and group 2 megaflood deposits from western Tibetan sources contain age peaks that are diagnostic of source areas in the middle reaches of the Yarlung drainage. It is not possible to tell whether zircons with these diagnostic ages were entrained from their source area directly during the flood that produced the sampled deposit, or reworked from the deposits of a previous flood event. Nevertheless, the zircon ages may be consistent with provenance from impoundments on the middle Yarlung River (e.g., the Dazhuka-Yueju Gorge; **Figure 2.1**) or tributaries to the Yarlung. Despite contributions to the zircon age signals of sediment reworking, our data show that the sediment preserved in megaflood slackwater deposits mostly comes from the western Tibetan sources within the Yarlung River drainage and from Namche Barwa/the Tsangpo Gorge—suggesting that these areas were where impounded lakes that sourced the megafloods were located.

Our data link most slackwater megaflood deposits to glacially impounded lake sources to the west of Namche Barwa, which is not surprising given the difference in valley morphology of the eastern and western drainages. Widespread glacial advances are dated throughout the region from 11-30 ka (Owen et al., 2002; Owen and Benn, 2005; Korup and Montgomery, 2008; Hu et al., 2017), including eastern Tibetan tributaries of the Yigong and Parlung River (Guangxiang and Xitao, 2007; Guangxiang & Qingli, 2012) that could result in glacial-moraine damming and lake impoundment. Glacial-moraine damming might produce smaller lakes in the eastern catchments compared to the Yarlung River catchment to the west of Namche Barwa because there is limited accommodation space for large (>10 km^3) lakes in these high-relief, narrow eastern tributaries. Indeed, the only mapped evidence of lacustrine sediments from glacial-impounded lakes exists in the Songzong sub-basin of the Parlung River catchment, which has a total area of only 16 km^2 (Guangxiang and Qingli, 2012). The area of the Songzong sub-basin is dwarfed by the areas of the Yarlung River sub-basins to the west of Namche Barwa (**Figure 2.1, Figure 2.3**). If the morphology of the Parlung and Yigong basins did not facilitate the formation of large glacially impounded lakes, this might explain why there is little evidence of megafloods from these tributaries in slackwater megaflood deposits along the Siang River.

2.5.2 *Preferential erosion and sediment evacuation from the Tsangpo Gorge during megafloods*

Our findings bear on the use of zircon age distributions to infer spatial patterns of erosion in the Eastern Himalaya. Lang et al. (2013) found a disproportionate amount of zircons from the Tsangpo Gorge in megaflood slackwater deposits compared to Yigong flood deposits and modern Siang River sediments, and used this result to argue that megafloods preferentially focus erosion in the Gorge. Our analyses of 1438 zircons from seven additional megaflood deposits brings the total observations to 11 deposits and n=1608 zircon data, which confirm that on average the megaflood samples do have a higher proportion of zircons derived from the Gorge compared to the modern Siang River and Yigong flood samples. However, our large dataset also shows significant variation among the zircon age distributions of individual megaflood deposits. Section 5.1 discussed the potential contributions to zircon provenance and age distributions of flood impoundment location and sediment reworking; here we explore the degree to which the age distributions reflect the spatial pattern of erosion during a flood event.

Megafloods that we interpret to have come from failed glacial moraine impoundments on the flanks of Namche Barwa just upstream of the Tsangpo Gorge (group 2) have the greatest contribution (~49%) of ~490 Ma zircons characteristic of Himalayan rock from the Tsangpo Gorge area in their deposits. We do not know how many of these zircons were eroded from the Gorge area during vs. prior to the megafloods that produced the sampled deposits. However, these megaflood deposits contain about twice as many ~490 Ma zircons as is observed in 2000 Yigong flood and modern Siang River deposits, and significantly more ~490 Ma zircons than are found in all but one of the other flood deposits (08KH24), indicating that sediment reworking cannot explain the bulk of this signal. Outburst floods sourced from impoundments at Namche Barwa would be expected to focus erosion near the breach, eroding and entraining a disproportionate amount of material in the Gorge area. We suggest the simplest interpretation is that the great abundance of Himalayan zircons in these deposits does reflect preferential erosion in the Tsangpo Gorge.

Varying proportions of Gorge-sourced zircons in the other megaflood samples are more difficult to interpret, but nevertheless support the idea that megafloods preferentially eroded and entrained material from the Tsangpo Gorge area compared to modern river flows. Individual megaflood sample age distributions vary due to factors like impoundment location and sediment recycling, making it impossible to quantify the specific percent contribution to the Gorge-sourced zircon signal due to erosion from the depositing megaflood. Despite these complications, 9 of the 11 megaflood deposits contain significantly more zircons sourced from the Tsangpo Gorge compared to modern Siang River sediments (**Figure 2.4**), providing strong evidence that megafloods are capable of focusing erosion in the Gorge. This finding combined with evidence indicating that most of these megafloods were probably sourced from impoundments in the Yarlung River drainage at or to the west of Namche Barwa, highlight the potential for repeated megafloods to influence the morphology of the Yarlung-Po River pathway through the Tsangpo Gorge—and support the hypothesis that preferential erosion of the Tsangpo Gorge during megafloods may have been an important mechanism for keeping pace with rapid rock uplift during the Quaternary.

2.6 CONCLUSIONS

We presented new detrital zircon U-Pb geochronology data for outburst flood slackwater deposits preserved downstream of the Tsangpo Gorge, that combined with previous zircon data for Tibetan source regions and downstream fluvial and outburst flood deposits shed light on the sources and erosional impact of Quaternary megafloods in the eastern Himalayan syntaxis. Despite complications due to the entrainment of previously deposited sediment along the flood pathway, the flood slackwater deposits contain clear zircon provenance signals that we interpret to reflect impounded lake sources and spatial patterns of erosion during floods:

- Diagnostic ≤250 Ma age components in the studied deposits indicate that most megaflood events were sourced from impoundments in the Yarlung River drainage at or to the west of Namche Barwa, with some sample ages suggesting provenance potentially as far upstream as the middle Yarlung.
- Only one of the eleven studied megaflood deposits may be compatible with an eastern Tibetan source on the Yigong and Parlung Rivers. It is possible that limited accommodation space for large (>10 km^3) lakes in the high-relief, narrow valleys of the Parlung and Yigong drainages may explain the paucity of evidence for megafloods from eastern Tibetan sources in our dataset.
- Our analyses of n=1139 zircons from 7 new megaflood deposits add significantly to the available data documenting floods through the Tsangpo Gorge, and confirm that megaflood deposits contain a disproportionate amount of zircons from the Gorge compared to the modern Siang River and historical Yigong flood deposits. The overabundance of Gorge-sourced zircons cannot be explained by sediment reworking alone, and provides evidence that megafloods preferentially focused erosion in the Gorge.

- The highest proportions of Gorge-sourced zircons are found in deposits from megafloods that we interpret to have been sourced from glacial-moraine dam impoundments on the flanks of Namche Barwa, immediately upstream of the Tsangpo Gorge. This finding highlights the potential for outburst flood source location to control erosion patterns by focusing erosion at and immediately downstream of the dam breach.

Taken together, our findings place new constraints on megaflood source locations and processes of sediment reworking that influence downstream zircon age distributions, and show that megafloods had the potential to preferentially erode the Tsangpo Gorge and contribute substantially to rapid exhumation of the Eastern Himalayan syntaxis.

Chapter 3. RADIOCARBON AND SINGLE-GRAIN LUMINESCENCE DATING OF MEGAFLOOD SLACKWATER DEPOSITS IN THE SIANG RIVER VALLEY

Ancient slackwater deposits in the Siang River valley, northeast India, record glacial outburst megafloods sourced from different areas of the Tibetan plateau and their profound impact on erosion of the eastern Himalaya. At present, there are few constraints on the depositional ages of megaflood deposits, limiting our understanding of the frequency of these events and of the net erosional impact of repeated megafloods in the region. In this study, we constrain the chronology of Siang River megafloods using radiocarbon and single-grain luminescence dating of sediment from a historical landslide-dam outburst flood and ancient megaflood deposits. Radiocarbon ages associated with megaflood deposits range from 1515 to 975 calibrated years B.P., overlapping the ages of impounded lake terraces just upstream of the Namche Barwa massif and Yarlung-Tsangpo Gorge. Single-grain infrared stimulated luminescence (IRSL) data (n=1484) from 15 slackwater outburst flood deposits show different degrees of bleaching. Four well-bleached single-age samples likely record the timing of megaflood events at ~29 and ~34 ka. Eleven poorly-bleached samples contain few grains that are consistent with the known age of the historical flood or maximum depositional age constraints from radiocarbon dating, and instead contain prominent inherited luminescence-age components. Two of the poorly-bleached samples are dominated by age components that are within error of ~34 ka, providing additional evidence that a megaflood occurred around this time. Prominent-age components in the other poorly-bleached samples at ~21, 24, and 42 ka may correspond to sediment recycled from previous megafloods. Altogether, the radiocarbon, single-age samples, and reworked megaflood event age components indicate there were at least 9 megaflood events since 42 ka. These luminescence data aid in the interpretation of detrital zircon U-Pb data from the same deposits by constraining the likely contribution of reworked sediment to the zircon record of flood provenance.

3.1 INTRODUCTION

Ancient sediments in the Siang River valley of northeastern India record a history of powerful glacial outburst megafloods sourced from Tibet that play an important role in shaping the rugged eastern Himalayan landscape and carving the Yarlung Tsangpo Gorge. Despite extensive sedimentary evidence of glacial-impoundments on the Yarlung River in the last 75 ka (**Figure 3.1**; Montgomery et al., 2004; Liu et al., 2006; Guangxiang and Xitao, 2007; Korup and Montgomery, 2008; Kaiser et al., 2010; Guangxiang and Qingli, 2012; Zhu et al., 2013; Zhu et al., 2014; Huang, 2014; Liu et al., 2015; Chen et al., 2016; Hu et al., 2018; Liu et al., 2018), the frequency of impoundment failure and the number of megafloods sourced from these lakes is unknown, limiting our understanding about how these events contribute to shaping this rapidly uplifting landscape over time.

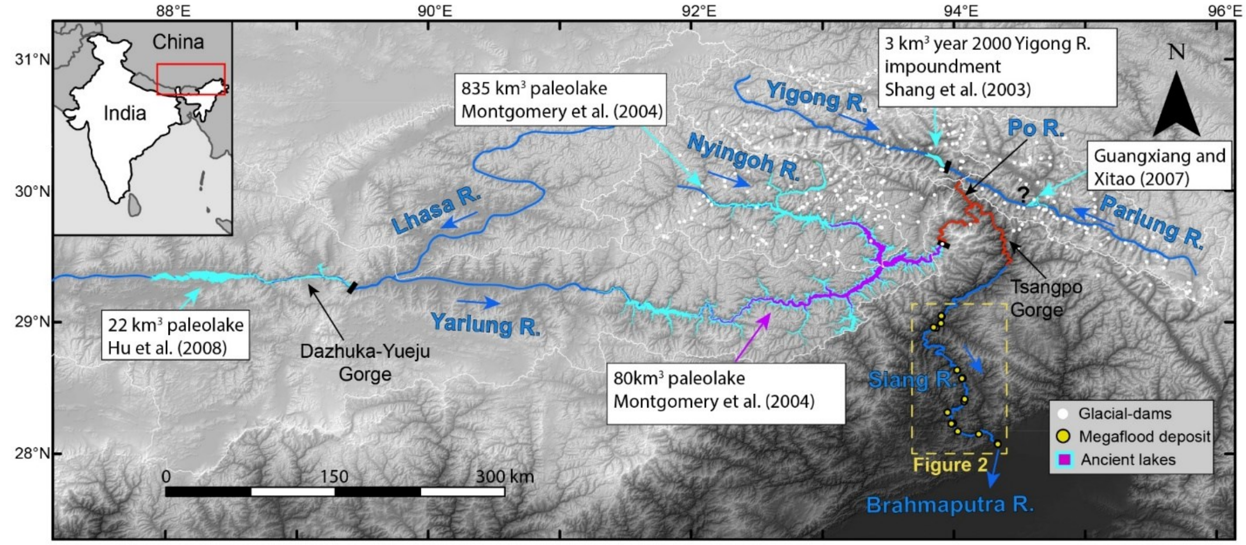

Figure 3.1. Study location

Location map of study shown with hillshade over SRTM3 digital elevation model. White dots show the location of possible ancient glacial-dams (Korup and Montgomery, 2008). Lacustrine sediments in Tibet on the Yarlung, Yigong, and Parlung Rivers constrain the timing and extent of several ancient glacially-dammed lakes.

Ancient slackwater deposits preserved in the Siang River valley downstream of the Tsangpo Gorge provide a record of megaflood events (**Figure 3.2**). Zircons analyzed from these deposits show that megafloods on average erode more rock from the Tsangpo Gorge compared to historical outburst floods and modern river flows (Lang et al., 2013; Chapter 2). The data also indicate that most megaflood events were sourced from impoundments to the west of Namche Barwa on the Yarlung River, but are insufficient to link deposits directly to impoundment location and do not constrain the chronology of these events (Chapter 2).

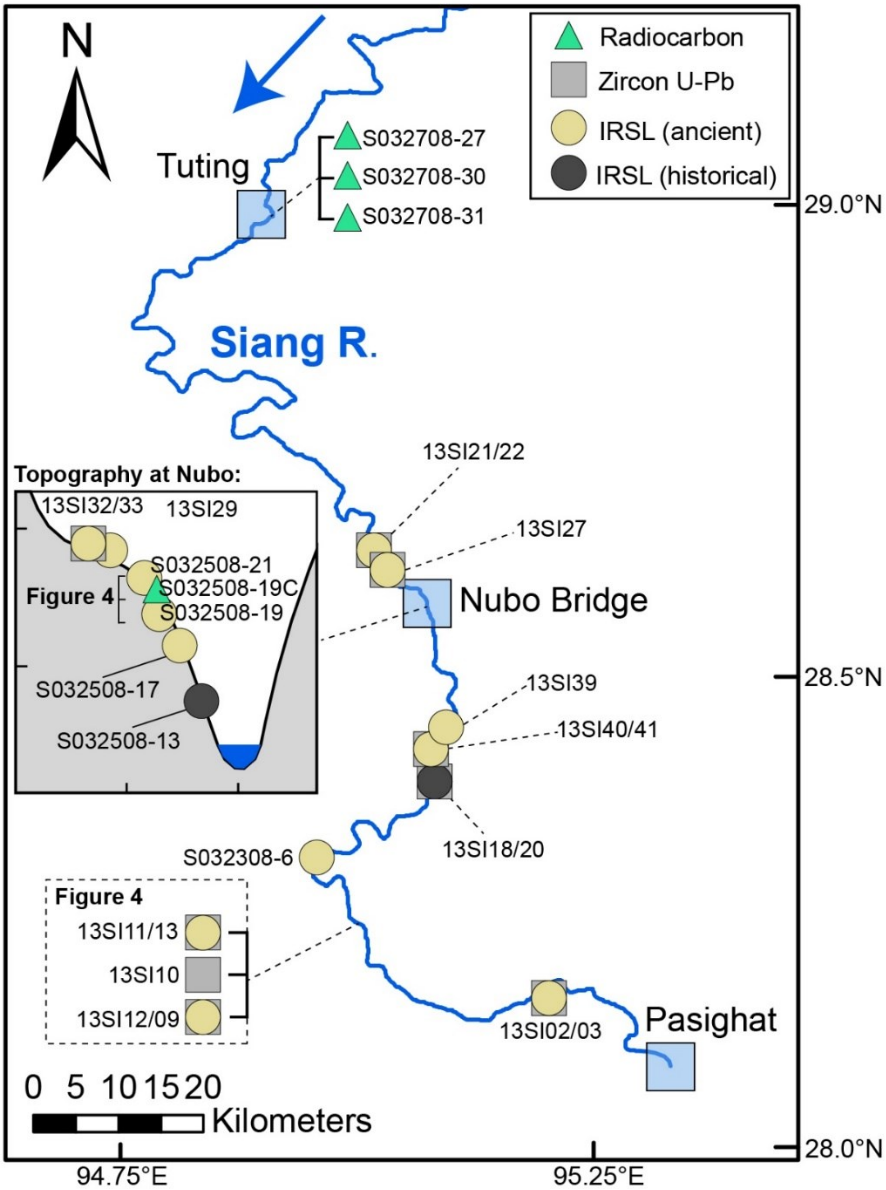

Figure 3.2. Deposit locations on the Siang River

The location of slackwater outburst flood deposits from the year 2000 Yigong River outburst flood and ancient megafloods on the Siang River in northeastern India sampled for zircon U-Pb, radiocarbon, and luminescence dating. Previous detrital zircon U-Pb megaflood samples are shown (gray box) in locations where deposits were also analyzed with luminescence (yellow circle).

Several geochronologic techniques are applicable to dating Quaternary flood slackwater deposits. Radiocarbon dating is useful to constrain the depositional age of flood sediments (e.g., Kirkbride et al., 2006; Lopes and Mix, 2009; Murton et al., 2010; Wiedmer et al., 2010; Margold et al., 2011; Waitt, 2016), by providing maximum depositional ages of charcoal in flood slackwater or other associated deposits. Luminescence dating methods that measure the time since sediment was last exposed to light are useful to date sediments that are >50 ka, beyond the range of conventional radiocarbon dating. Many studies have applied optically stimulated luminescence (OSL) to date flood sediments (Srivastava et al., 2009; McLaren et al., 2009; Kale et al., 2010; Medialdea et al., 2011; Tsukamoto et al., 2013; Kunz et al., 2014; Singh and Jaiswal, 2019; Goswami et al., 2019; He et al., 2019), and one study applied these methods to multi-aliquot quartz samples from four ancient megaflood deposits in the Siang River valley (Srivastava et al., 2017). A potential complication with multi-aliquot flood deposit samples, for which the luminescence signal is measured from many grains at once, is partial bleaching, where not all grains analyzed in a sample are reset by exposure to light (Duller, 2008; Rhodes, 2011; Rhodes, 2015). Luminescence samples from fluvial sediments often have few well-bleached grains (Fiebig and Preusser, 2007; Singh and Jaiswal, 2019), and the degree of bleaching in outburst flood sediments on the Siang River is unknown. Some sediment transported during high-energy outburst floods is likely reset by light when it is exposed at the surface of the flow, but other sediments might retain a luminescence signal from previous events. Therefore, single-grain methods are necessary to constrain bleaching patterns in outburst flood deposits and to accurately interpret luminescence data for ancient megaflood sediments.

In this study, we constrain megaflood chronology with radiocarbon and single-grain infrared stimulated luminescence dating (IRSL) of feldspar from slackwater megaflood deposits preserved along the Siang River valley (**Figure 3.2**). Radiocarbon dating is applied to charcoal obtained from three samples of an ancient slackwater deposit and from a landslide separating flood deposits in a vertical sequence. We develop and analyzed a large single-grain IRSL dataset (n=1484) from samples of two historical outburst flood deposits, and 13 ancient megaflood deposits. The slackwater deposit samples are also interpreted in the context of detrital zircon U-Pb samples from previous work (**Figure 3.2**), providing new constraints on the timing, sources, and erosional impact of megafloods through the Tsangpo Gorge.

3.2 BACKGROUND

3.2.1 *Records of ancient impounded lakes across the Tibetan Plateau*

There is widespread sedimentary and geomorphic evidence of glacial-moraine dams upstream of the Tsangpo Gorge that could have impounded the Yarlung River or its tributaries and produced megafloods (**Figure 3.1**; Korup and Montgomery, 2008; Korup et al., 2010). Ancient lacustrine sediments are observed on northeastern tributaries that flow into the Tsangpo Gorge through the Po River (Guangxiang and Xitao, 2007; Guangxiang and Qingli, 2012) and from the Yarlung River to the west of Namche Barwa (Montgomery et al., 2004; Liu et al., 2006; Korup and Montgomery, 2008; Kaiser et al., 2010; Zhu et al., 2013; Zhu et al., 2014; Huang, 2014; Liu et al., 2015; Chen et al., 2016; Hu et al., 2018; Liu et al., 2018). The spatial extent and chronology of several glacially impounded lakes is constrained by lacustrine sediments (**Figure 3.1**), but dated lake sediments are few, and not all of the lakes may have failed catastrophically to produce megafloods.

Lacustrine sediments on the Parlung River, to the northeast of the Tsangpo Gorge, indicate that it was likely impounded from 22.5 to 16.1 kyr B.P. (Guangxiang and Xitao, 2007; Guangxiang & Qingli, 2012). No clear observations of the full extent of this impoundment or sedimentary evidence that it produced a megaflood down the Po River into the Tsangpo Gorge (Guangxiang and Xitao, 2007; Guangxiang and Qingli, 2012) exist at this time, and little evidence of megafloods from this source area are apparent in detrital zircon U-Pb ages from megaflood slackwater deposits downstream (Chapter 2). Nevertheless, the nearby Yigong River has been the source of at least two landslide-dam outburst floods in 1900 and 2000 (Shang et al., 2003; Evans and Delaney, 2011; Delaney and Evans, 2015) that caused significant erosion and deposition along the flood pathway and through the Tsangpo Gorge downstream (Finnegan et al., 2008; Larsen and Montgomery, 2012; Turzewski et al., 2019).

Lacustrine terraces were dated with radiocarbon on the Yarlung River directly west of Namche Barwa (**Figure 3.1**) and the ages offer constraints on when two glacial lakes may have existed to produce megafloods (Montgomery et al., 2004; Liu et al., 2006). The lowest elevation terraces on the Yarlung River that are closest to the Tsangpo Gorge are at 3071 and 3104 m a.s.l., and date respectively from 1702 to 1584 cal. yr B.P and 1335 to 1127 cal. yr B.P. (Montgomery et al., 2004). The elevations of these terraces imply an 81 km^3 paleolake based on modern topographic datasets (**Figure 3.1**; Montgomery et al., 2004). Nearby terraces at 3525 and 3540 m a.s.l. date respectively from 11469 to 11267 cal. yr B.P. and from 10235 to 9844 cal. yr B.P, that could potentially correspond to a larger >800 km^3 lake (Figure 1; Montgomery et al., 2004). Lacustrine terraces on the Nyingoh River span a large time period from 41 to 13 ka B.P. (Liu et al., 2015), and terrace sediment near the confluence of the Nyingoh and Yarlung Rivers are up to 75 ka (Zhu et al., 2013). However, the overlap of the spatial extent of impounded lakes near the confluence of the Nyingoh and Yarlung River makes it difficult to constrain lake chronology and indicates that there were several filling and emptying events that may have produced megafloods (Montgomery et al., 2004; Liu et al., 2006; Zhu et al., 2013; Huang et al., 2014; Liu et al., 2015).

Luminescence dating of lacustrine sediments constrain a ~22 km^3 impounded lake from 32.3 to 13.2 ka B.P. further upstream to the west in the middle reaches of the Yarlung River near the Dazhuka-Yueju Gorge (**Figure 3.1**; Hu et al., 2018). Coarse gravels and bedforms downstream of the Dazhuka-Yueju Gorge are evidence that this lake failed sometime near the age of the highest terrace sediments around 13.2 ka (Hu et al., 2018). A detrital zircon U-Pb signature of sediment sourced from tributaries in the middle-reaches of the Yarlung River is observed in megaflood deposits downstream along the Siang River (Chapter 2), which shows that megaflood events were either sourced from this region or that megafloods have reworked and transported sediment from this source.

3.2.2 *Megaflood deposits on the Siang River, northeastern India*

Zircons from 11 megaflood deposits located downstream of the Tsangpo Gorge on the Siang River were analyzed in previous studies (Lang et al., 2013; Chapter 2). Detrital zircon U-Pb data show that most deposits were sourced from megafloods that originated to the west of Namche Barwa on the Yarlung River and that deposits may contain a record of recycled sediment from previous megaflood events (Chapter 2). Zircon U-Pb data from individual megaflood deposit samples cannot be linked directly to impoundment location and do not constrain depositional age. However, four other megaflood deposits in the Siang River valley were dated in a previous study using optically stimulated luminescence methods on multi-aliquot samples of quartz, resulting in minimum ages ranging from 8 to 6 ka (Srivastava et al., 2017).

3.3 METHODS

3.3.1 *Radiocarbon sample collection and dating methods*

Four detrital charcoal samples were collected in 2008 and dated using radiocarbon analysis (**Table 3.4**). Three of the samples (S032708-27, S032708-30, S032708-31) were obtained from pits dug into an ancient megaflood deposit on a terrace near Tuting village that is 107 m above the modern river level at low flow (**Figure 3.2; Figure C1**). The fourth radiocarbon sample (S032508-19C) is wood that was collected from a small stone line separating two slackwater deposits at the Nubo Bridge location, 98 m above the modern river level (**Figure 3.2; Figure 3.3**). Soil development was present around the stone line, and the angularity of the cobbles indicates that the feature separating the two slackwater deposits is a small landslide deposit. Samples were dated using accelerated mass spectrometry and calibrated with the curve from Reimer et al. (2013) using OxCal 4.3 software (**Figure C2**; Bronk and Ramsey, 2009a).

Table 3.4. Radiocarbon samples

Sample ID	Lon	Lat	14C age	Cal. B.C. (yr)	Cal. B.P. (yr)	Probability (%)
S032708-27	94.89684	28.99974	1381±27	610 - 675	1344 - 1409	95.4
S032708-30	94.89684	28.99974	1130±23	953 - 1044	975 - 1066	90.8
S032708-31	94.89684	28.99974	1637±27	504 - 598	1421 - 1515	54.6
S032508-19C	95.06686	28.57957	1248±67	654 - 900	1119 - 1365	92.5

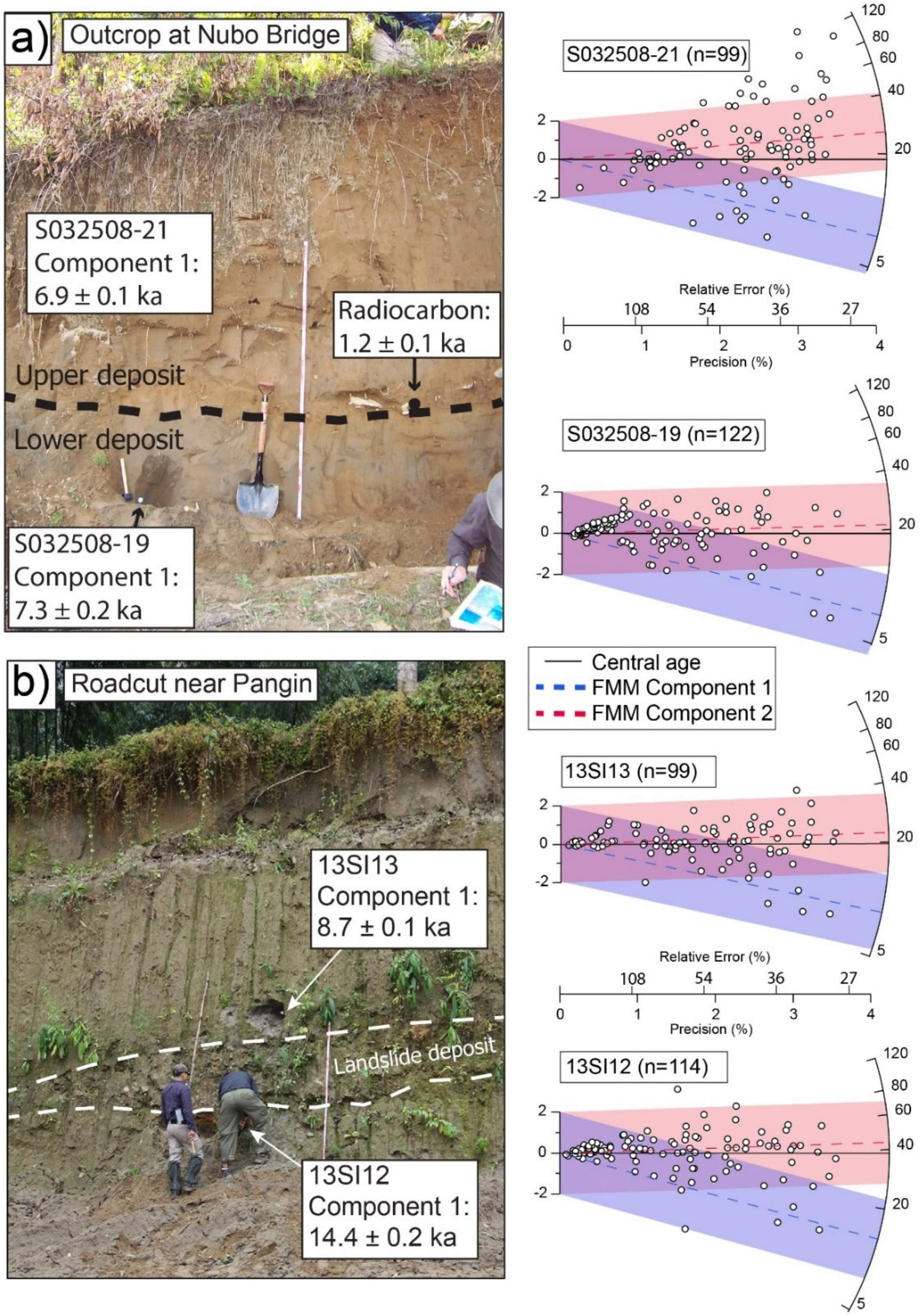

Figure 3.3. Slackwater deposits in vertical sequences

Slackwater megaflood deposits separated by landslides were identified at the Nubo Bridge roadcut (a) and in the roadcut near Pangin Village (b). Radial error plots of IRSL ages from these (4) megaflood samples are shown on the right.

3.3.2 *Luminescence sample collection and dating methods*

Sediment for luminescence dating was collected from 15 outburst flood deposits preserved in road cuts and on terraces in the Siang River valley during field seasons in 2008 and 2012 (**Figure 3.2**). Six of the 13 ancient glacial-lake outburst megaflood deposits and one of the two deposits from a historical landslide-dam outburst flood analyzed for luminescence dating here were described and analyzed for detrital zircon U-Pb dating in previous studies (Lang et al., 2013; Chapter 2). Two luminescence samples are from deposits of the historical 2000 Yigong River outburst flood (hereafter, Yigong flood) studied by Lang et al. (2013) and Turzewski et al. (2019), which are <50 m above the modern river level at low flow. The other thirteen samples are from ancient megaflood deposits that range from 66 to 355 m in elevation above the modern river level (**Table 3.5**).

Table 3.5. Luminescence sample locations and calculated ages

Luminescence sample	Zircon U-Pb sample	Lon	Lat	n	Overdispersion (%)	CAM age (ka)	S.E.	MAM age (ka)	S.E.
S032308-6	-	94.95328	28.31759	144	46.1	30.5	1.6	18.0	1.8
S032508-13	-	95.06935	28.57659	178	105	24.1	2.4	2.7	0.6
S032508-17	-	95.06778	28.57987	80	69.7	19.9	2.1	18.7	3.2
S032508-19	-	95.06686	28.57957	122	41.9	19.2	1.5	13.6	1.4
13SI29	-	95.06302	28.57630	91	46.1	30.8	2.2	19.0	2.8
13SI33	13SI32	95.06281	28.57915	119	32.5	29.3	1.3	20.6	1.2
13SI12	13SI09	94.98277	28.23355	114	41.3	38.2	2.7	25.9	3.9
13SI13	13SI11	94.98277	28.23355	99	36.7	19.5	1.1	14.4	1.8
13SI03	13SI02	95.19072	28.15330	145	43.5	27.7	1.6	17.3	2.5
13SI22	13SI21	95.02667	28.63944	45	48.4	32.8	4.4	24.3	6.2
13SI27	-	95.02378	28.63391	56	23.8	34.6	2.6	34.4	5.6
13SI39	-	95.09100	28.42430	70	23.9	34.4	2.6	34.2	3.0
13SI41	13SI40	95.08376	28.41904	58	50.9	34.9	4.0	20.3	4.6
13SI20	13SI18	95.07956	28.40177	64	75.5	15.4	2.0	4.7	1.1
S032508-21	-	95.06686	28.57957	99	62.4	18.7	1.8	10.9	1.4

Two of the megaflood IRSL samples were taken from a sequence of deposits separated by landslides in a roadcut near the Siyom tributary of the Siang River (**Figure 3.3**). Six of the megaflood samples and a single Yigong flood sample are from the Nubo Bridge area; several of the megaflood samples were in vertical sequences separated by landslides in this location (**Figure 3.2, Figure 3.3**). The rest of the analyzed flood deposits were sampled from terraces at different elevations along the Siang River valley and were not observed in vertical sequences or directly adjacent to other deposits (**Figure 3.2**). All deposits sampled were >1 m thick and composed of fine-medium grain sand. Fresh holes were dug into the outcrops and luminescence samples were collected using PVC tubes with caps secured using tape. A kilogram of sand was collected at each sample site to measure dose rate and moisture content.

Measurements of the dose rate (D_r) and equivalent dose (D_e) are required to determine a luminescence age. The equivalent dose D_e (Gy) is the dose absorbed since the last zeroing event and it is determined by calibrating the natural signal to signals produced by artificial irradiation in the laboratory. This measurement is divided by a measurement of the natural dose rate, D_r (Gy/ka), consisting of alpha, beta, gamma and cosmic radiation, to estimate the age of the grain:

$$Age = \frac{D_e}{D_r} \tag{3.2}$$

Because measurements are made on feldspars, which are prone to anomalous fading (athermal loss of signal), fading corrections are applied to the age of each grain measured. Laboratory methods to measure the dose rate (D_r), equivalent dose (D_e), and to correct for fading are in the supporting information (**Text C1; C2**).

We addressed anomalous fading in the feldspar grains measured following the approach of Auclair et al. (2003) and corrected ages following Huntley and Lamothe (2001). High temperature IRSL stimulation, which produces a signal that shows less fading (Buylaert et al.

2012) than the low temperature stimulation used here, was not employed because of the relatively poor bleaching of the high stimulation signal. A fading correction was applied to each individual grain, which despite scatter resulting in lower precision has relatively good reproducibility (supplementary material in Feathers et al., 2018). Ages are quoted with 1-sigma errors.

A dose recovery test was performed to test procedures and estimate over-dispersion used for modeling grain ages with the central age model (CAM), minimum age model (MAM), and a finite mixture model (FMM) (Galbraith et al., 1999; Arnold et al., 2009; Galbraith and Roberts, 2012). Over-dispersion refers to percent variation that cannot be accounted for by differences in precision among ages. Broader distributions of the ages result in higher over-dispersion. The dose recovery test was performed on a sub-sample of n=121 grains (13SI13; 13SI03; 13SI29; **Figure C3**). In this test, luminescence was removed by exposure to 1 s of the laser and then a dose of known magnitude was administered. The single-aliquot regenerative-dose (SAR) procedure is then applied to try to recover the known dose.

3.4 RESULTS

Data from radiocarbon samples are in **Table 3.4, Figure 3.4, and Figure C2**, and the data from all single-grain luminescence measurements from the 15 samples (n=1484) are in the supporting information **Table C1**. Ages determined in each luminescence sample and from the dose recovery test are presented as radial plots shown in **Figure 3.3 and Figures C3-C5.** The dose recovery test on the sub-sample produced a value of 0.961 ± 0.023 with 23% over-dispersion; we therefore conservatively considered 25% over-dispersion to be well-bleached for single-age samples to calculate age components in the MAM and FMM.

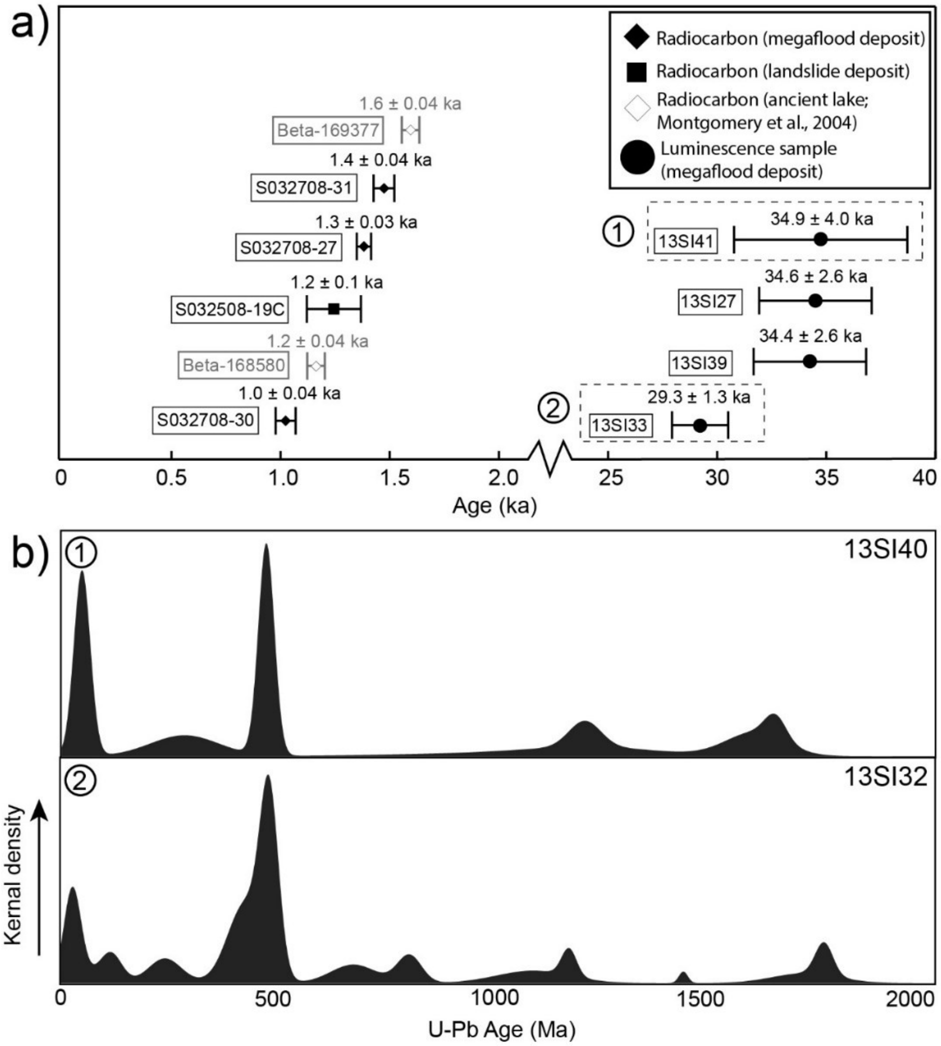

Figure 3.4. Luminescence data from Nubo Bridge samples

Radiocarbon dates from ancient megaflood deposits are shown on the right of (a) from present to 2 ka, along with the age of dated terraces that constrain an ancient impounded lake near Namche Barwa (Montgomert et al., 2004). Ages determined from the central age model (CAM) for four well-bleached single-age megaflood depost samples are shown on the left axis that ranges from 25 to 40 ka. The zircon U-Pb distribution from two of these samples (1, 2) is shown below in (b) on kernal density estimate plots.

3.4.1 *Radiocarbon results from slackwater flood and associated deposits*

Radiocarbon ages from a megaflood deposit on a terrace near Tuting village (**Figure 3.2; C1**) range from 1515 to 975 calibrated years B.P. (**Figure 3.4**; **Table 3.4**). The youngest of these three radiocarbon samples is 1020 ± 45 years B.P. (90.8% probability), which pre-dates the youngest terrace sediments at ~1200 years B.P. near Namche Barwa (**Figure 3.4**; Montgomery et al., 2004). The oldest radiocarbon age from these three samples (1468 ± 47 years B.P.) is in between the ages of the youngest and oldest (1643 ± 40 years B.P) terrace sediments near Namche Barwa (Montgomery et al., 2004). The radiocarbon age of the charcoal sample taken from the landslide separating two ancient megaflood deposits at the Nubo Bridge location (**Figure 3.3a**) is 1242 ± 123 years B.P, which is also in between the ages of dated terrace sediments from ancient impounded lakes near Namche Barwa (**Figure 3.4**).

3.4.2 *Luminescence results from slackwater flood deposits*

Luminescence data show that four of the ancient megaflood samples (13SI27, 13SI33, 13SI39, 13SI41) are well-bleached single-age samples that are characterized well by the CAM (**Figure 3.4, Figure C5, C6**). The central age of sample 13SI33 is ~29 ka, and the central ages of samples 13SI27, 13SI39, and 13SI41 are within error at ~34 ka (**Figure 3.4, C6**). The rest of the slackwater flood deposits analyzed, including samples from the Yigong flood, have different degrees of bleaching and we constrain multiple age components with the FMM (**Figure 3.5**).

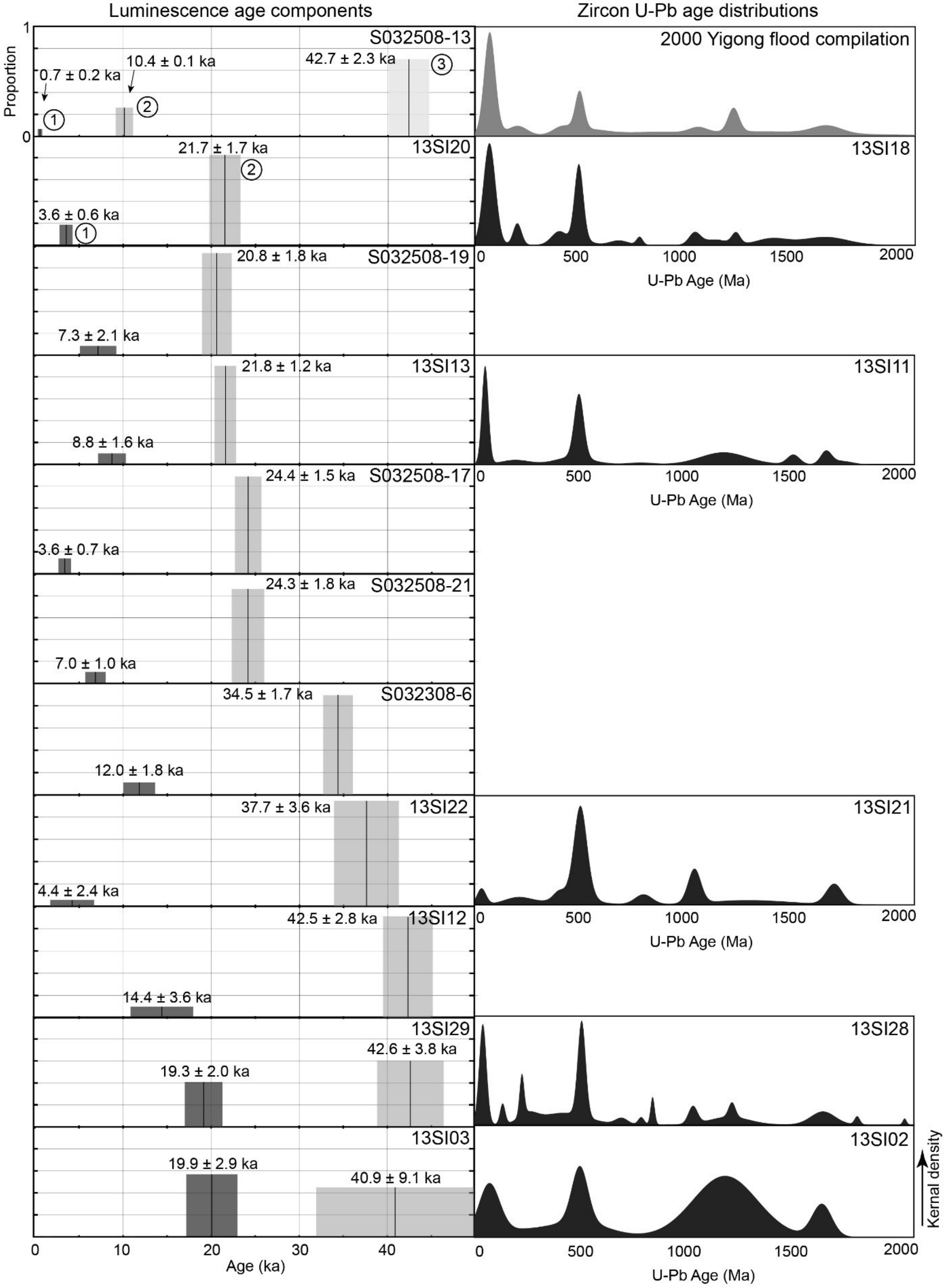
Luminescence age components
Zircon U-Pb age distributions
Proportion
1
0
S032508-13
0.7 ± 0.2 ka
①
10.4 ± 0.1 ka
②
42.7 ± 2.3 ka
③
2000 Yigong flood compilation
13SI20
21.7 ± 1.7 ka
②
3.6 ± 0.6 ka
①
13SI18
S032508-19
20.8 ± 1.8 ka
7.3 ± 2.1 ka
13SI13
21.8 ± 1.2 ka
8.8 ± 1.6 ka
13SI11
S032508-17
24.4 ± 1.5 ka
3.6 ± 0.7 ka
S032508-21
24.3 ± 1.8 ka
7.0 ± 1.0 ka
S032308-6
34.5 ± 1.7 ka
12.0 ± 1.8 ka
13SI22
37.7 ± 3.6 ka
4.4 ± 2.4 ka
13SI21
13SI12
42.5 ± 2.8 ka
14.4 ± 3.6 ka
13SI29
42.6 ± 3.8 ka
19.3 ± 2.0 ka
13SI28
13SI03
19.9 ± 2.9 ka
40.9 ± 9.1 ka
13SI02
Kernal density
0
10
20
30
40
Age (ka)
0
500
1000
1500
2000
U-Pb Age (Ma)

Figure 3.5. Luminescence age components in flood samples

Age components idenfitied with the finite mixture model (FMM) in the year 2000 Yigong flood samples and ancient slackwater megaflood samples are shown on the left, and the corresponding zircon U-Pb distrbution for several of these samples is shown on the KDE plots to the right. Note that the Yigong flood sample 13SI20 is the only sample that contains (3) age components and it has a corresponding zircon U-Pb sample 13SI18. The full compilation of Yigong flood samples is shown adjacent to sample S032508-13.

Samples from the Yigong flood have luminescence age distributions that do not represent the known depositional age of the deposits. These two samples have only nine grains that are <1 ka and they have overdispersion values ≥75%, much higher than the 25% assumed for a well-bleached sample (**Figure 3.5**). Three components are identified in sample S032508-13 at ~0.7, 10, and 42 ka, whereas two components are identified in sample 13SI20 at ~3 and 21 ka (**Figure 3.5**).

The eight megaflood deposits that are not well characterized by the CAM each contain two age components identified with the FMM (**Figure 3.5**). In two of these megaflood deposits, the two age components (in this case ~41-43 ka and ~19-20) each contribute similar numbers of grains to the luminescence signal. The remaining six megaflood deposits are dominated by their older age components, which range from ~21 to ~43 ka and represent ≥80 % of the grains in each sample; the smaller, younger age components in these six megaflood deposits range from ~4 to 14 ka. Only three deposits have an age component at ~7-8 ka that is within error of the minimum multi-aliquot OSL ages from previously dated ancient megaflood deposits (Srivastava et al., 2017).

3.4.3 *Comparison of luminescence and radiocarbon results from related deposits*

Age components identified in luminescence samples from ancient megaflood deposits above and below the landslide deposit dated with radiocarbon (**Figure 3.3a**), are older than the radiocarbon age (1242 ± 123 years B.P). The youngest age component in the slackwater flood deposit above the landslide (S032508-21) is 6.9 ± 0.1 ka and makes up ~16% of the sample; this component is very close in age to the youngest component in the slackwater flood deposit below the landslide (S032508-19) at 7.3 ± 0.2 ka that makes up ~7% of the sample (**Figure 3.3a**). Most of the grains (84%) in the upper flood deposit are associated with an older age component at ~24 ka, and most of the grains (93%) in the lower flood deposit are associated with a component at ~20 ka.

Samples 13SI13 and 13SI12 were collected above and below a landslide that was not dated with radiocarbon (**Figure 3.3b**). The youngest component in the sample below the landslide (13SI12) is at ~14 ka and the oldest component is at ~43 ka, whereas the youngest in the sample above the landslide (13SI13) is at ~8 ka and the oldest is at ~22 ka (**Figure 3.3b**). The remaining megaflood slackwater samples were collected from outcrops at various elevations, and not directly related to one another (**Figure 3.2**).

3.4.4 *Comparison of luminescence and zircon U-Pb results from the same deposits*

Previously published zircon U-Pb data from one of the historical Yigong flood deposits and six of the megaflood deposits analyzed here also show some patterns that provide insight into the various sources of sediment integrated by the 15 slackwater flood deposit samples. The zircon U-Pb age distribution from different slackwater deposits of the Yigong flood are similar to each other (**Figure 3.5;** Chapter 2), reflecting their shared flood source and flood pathway through the Tsangpo Gorge, but luminescence samples from deposits of this event have different age components (**Figure 3.5**). Single-age megaflood samples that have ages at 29 ka and 34 ka, have associated zircon U-Pb samples that are different from one another (**Figure 3.4, C6**). The two megaflood deposits with grains evenly distributed between components at ~19 and 42 ka have different zircon U-Pb age distributions.

3.4.5 *Timing of megaflood events on the Siang River*

The tightly constrained Gaussian age distributions in both the single-age component and multi-age component luminescence samples are consistent with rapid bleaching. Partial bleaching of fluvial sediments will produce a uniform/broad age distribution rather than tightly constrained Gaussian distributions like we see here (Singh and Jaiswal, 2019). We therefore suggest bleaching during outburst floods is likely to be responsible for these narrow age components.

If this is the case, single-age luminescence samples and the overlap between bleached age components identified in flood deposits provide evidence of at least 9 megaflood events on the Siang River since 42 ka (**Table 3.6; Figure 3.6**). The first is at ~0.7 ka, defined by the youngest age component in a Yigong flood deposit sample (S032508-13). A second event at ~4 ka is constrained by data from three samples (13SI20, S032508-17, 13SI22). Age components in three samples are consistent with a flood around 8-7 ka (S032508-19, 13SI13, S032508-21); this timing is within error of 8-6 ka OSL dates from megaflood deposits in the valley (Srivastava et al., 2017), but the coincidence in dates may be fortuitous since our single-grain feldspar IRSL data suggest such multi-aliquot OSL samples may average multiple bleached age components in a deposit. Two samples constrain a broad period when a flood may have occurred from 14 to 10 ka (S032508-13, S032308-6). Five samples have data consistent with a flood around 21-19 ka (13SI20, S032508-19, 13SI13, 13SI29, 13SI03) and two samples show a flood at 24 ka (S032508-17, S032508-21). A single-age sample (13SI33) indicates a flood occurred around 29 ka. Two samples suggest a flood around 37-34 ka (S032308-6, 13SI13), and four samples show a flood occurred at around 42 ka (S032508-13, 13S12, 13SI29, 13SI03).

Table 3.6. FMM age components

Samples	Component	Age (ka)	Error (ka)	Event
S032508-13	1	0.7	3.8	1
13SI20	1	3.6	0.6	2
S032508-17	1	3.6	0.7	
13SI22	1	4.4	2.4	
S032508-19	1	7.3	2.1	3
13SI13	1	8.8	1.6	
S032508-21	1	7	1	
S032508-13	2	10.3	0.8	4
S032308-6	1	11.9	1.7	
13SI12	1	14.4	3.5	
13SI20	2	21.6	1.7	5
S032508-19	2	20.7	1.6	
13SI13	2	21.7	1.2	
13SI29	1	19.3	2	
13SI03	1	19.9	2.9	
S032508-17	2	24.4	1.5	6
S032508-21	2	24.3	1.8	
13SI33	1*	29.3	1.3	7
13SI27	1*	34.6	2.6	8
13SI39	1*	34.3	2.5	
13SI41	1*	34.8	3.9	
S032308-6	2	34.5	1.6	
13SI22	2	37.7	3.5	
S032508-13	3	42.6	2.2	9
13SI12	2	42.5	2.8	
13SI03	2	40.9	9.1	

Some of the nine time periods defined by luminescence age components overlap with ages of glacial lake impoundments in Tibet that are thought to have sourced outburst megafloods (**Figure 3.6**). The ~0.7 ka age luminescence age component is similar to the youngest terraces dated at ~1.2 ka near Namche Barwa, while the 14-10 ka luminescence age overlaps with the older terrace sediments dated near Namche Barwa (Montgomery et al., 2004). Luminescence components in the 21-19 ka and 24 ka age ranges overlap the ages of many paleolake sediments dated to the west (Hu et al., 2018; Liu et al., 2015) and on the Parlung River in the east

(Guangxiang and Qingli, 2012). Older luminescence age components at 37-34 ka and 42 ka in flood deposits both overlap lake sediments dated on the Nyingoh River (Liu et al., 2015).

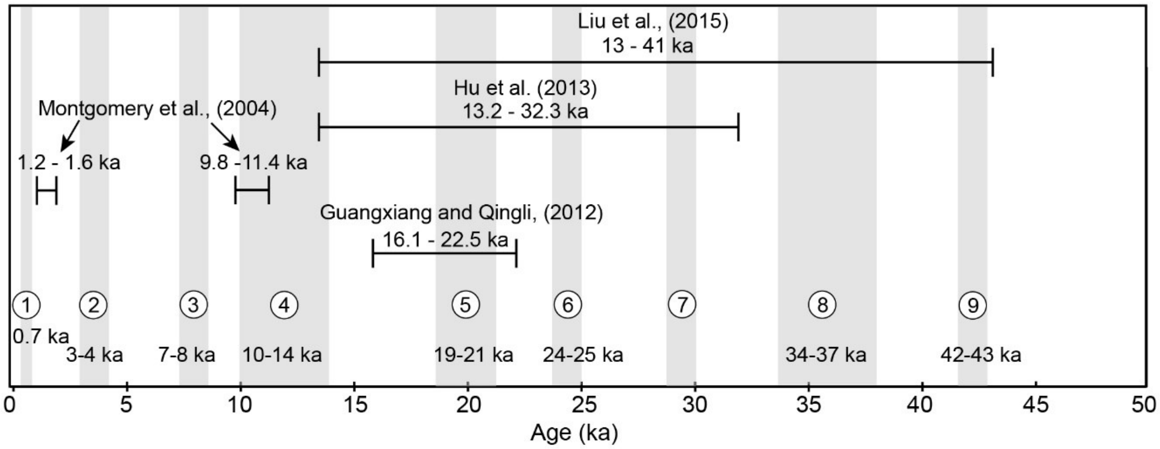

Figure 3.6. Megaflood events and the timing of ancient lakes

Potential megaflood events 1-9 (gray bars) dated from slackwater deposits plotted alongside dated terraces that constrain the age of ancient glacial lakes in Tibet.

3.5 DISCUSSION

Radiocarbon and luminescence age data presented here constrain the timing of several megaflood events on the Siang River, and provide evidence that megafloods rework and mix sediment from previous megaflood events. Radiocarbon ages from a megaflood deposit are consistent with an event sourced from dated lake terraces in Tibet near Namche Barwa (Montgomery et al., 2004), providing the first chronological link between a megaflood source observed near Namche Barwa and deposit. The luminescence data from 15 slackwater deposits include some single-age samples that likely represent the timing of megafloods, but also show that deposits inherit various bleached age components that we interpret to be from previous megaflood events. Slackwater outburst flood deposits are dominated by grains reset during megafloods that occurred >19 ka, indicating that there is stored sediment from these megaflood events in deposits along the flood pathway in the Siang River that are being reworked, and shedding light on the interpretation if detrital zircon U-Pb data from slackwater flood deposits.

3.5.1 *Constraining megafloods from radiocarbon and single-age luminescence samples*

Some of the radiocarbon and luminescence ages provide constraints on the timing of megaflood events in the Siang River valley. We report the first radiocarbon ages obtained from a megaflood deposit, which provide maximum constraints on the timing of a Holocene megaflood event sometime ~1 ka (**Figure 3.4**). The timing of a megaflood at ~1 ka could indicate it was sourced from the ancient lake constrained by dated terraces near Namche Barwa from 1.6 to 1.2 ka (Montgomery et al., 2004). Although we lack any zircon U-Pb analyses from these megaflood deposits, we might expect zircons from this sample to be dominated by a signature of Namche Barwa rock if these deposits were sourced from a megaflood near this impoundment location, such as sample 13SI21 that is dominated by anatectic zircons and zircons from 350 to 550 Ma (**Figure 3.5**). However, sample 13SI21 is from a deposit dated with luminescence that has a prominent age component at ~37 ka, so it is possible that a luminescence sample taken from the deposit sampled with radiocarbon has a similar inherited age component, despite being constrained with a maximum depositional age of ~1 ka. The three radiocarbon ages that are >1 ka from the megaflood deposit (**Figure 3.4**) could also be inherited from sediment leftover from older megaflood events, which would be consistent with the patterns of recycling observed in the luminescence data.

Single-age luminescence samples likely correspond to the timing of two older megaflood events at ~29 and 34 ka, but the reason why these four samples are well-bleached while the other nine samples are poorly bleached is unclear. It is possible the CAM result of ~29 ka gives a poor characterization of the age of the sample and application of the MAM is more suitable to determine a minimum age of the deposit at ~20 ka (**Table 3.5**), which is more in-line with components observed in other samples. Alternatively, there are no prominent age components near ~29 ka in any of the other slackwater deposits, which might indicate that there was a small amount of sediment transported and deposited during the megaflood event at ~29 ka. A smaller concentration of sediment in the water column during a megaflood could be the reason why these sediments are more well-bleached compared to other megaflood deposit samples transported in a megaflood with a high sediment concentration. This is not the case with the single-age samples at ~34 ka because we observe components making up >90% of other megaflood samples near 34 ka in at least three megaflood deposits, showing there is a large amount of sediment stored in the valley from a megaflood event or events at ~34 ka that have since been entrained and re-deposited by more recent floods.

3.5.2 *Interpreting mixed luminescence age components in slackwater deposits*

The mismatch between single-grain IRSL ages in deposits above and below the landslide dated with radiocarbon (**Figure 3.3a**) provides additional evidence that luminescence ages in some deposits are most likely inherited from previously bleached sediment. We suspect that all prominent luminescence components >19 ka that are observed in poorly bleached samples, represent sediment inherited from bleaching during past megaflood events. These >19 ka components characterize most of the grains observed in slackwater deposits, indicating there could be a substantial amount of stored sediment from megaflood events >19 ka that is sourced either from the lacustrine sediments near source locations in Tibet or in fluvial/terrace deposits along the flood pathway downstream in the Tsangpo Gorge or the Siang River. The Yigong River outburst flood deposits share the ~20 and 42 ka age components with several megaflood deposits that have U-Pb age signatures showing they are likely sourced from impoundments west of Namche Bawra (**Figure 3.5**). The Yigong River outburst flood traveled along the Po River into the Tsangpo Gorge (**Figure 3.1**) before sharing the same pathway with megaflood events sourced from the west. Therefore, these components are most likely integrated along the pathway of the Tsangpo Gorge and Siang River that is shared by both the 2000 Yigong flood and megafloods sourced from west.

Much of the Siang River pathway from upstream of Tuting village to the Tsangpo Gorge (**Figure 3.1**) has not been explored for megaflood deposits, but deposits along this segment of the river could be sources of these sediments from megaflood events >19 ka. Simulations of the Yigong flood show that it likely produced km-scale boulder bars (Chapter 1), so it is possible that sediment entrained in boulder bars left behind during megaflood events in the gorge or the Siang River is the source of the >19 ka material observed downstream. Simulations from the Yigong flood also indicate that backflow into various tributaries that feed into the Siang River was likely during past megafloods. Such backflow may have led to the deposition of thick sediments near these confluences, which could also be the source of ancient sediments from these floods. Contribution of sediment from these sources might have resulted in less bleaching during megafloods over time, which could be the reason why we see such relatively small age components from younger megafloods (**Figure 3.5**).

Some luminescence samples also have corresponding zircon U-Pb samples that provide additional evidence that there is mixing of stored sediment in megaflood deposits from previous events in the Siang River valley, which could have important implications for how we interpret detrital zircon U-Pb data. Two of the megaflood deposits have a relatively even amount of grains distributed around age components at ~19 and 42 ka, and also have zircon U-Pb signatures that could be influenced by mixing of reworked megaflood sediment (**Figure 3.5**). For example, the presence of many zircon age components in a sample (e.g. 13SI28; **Figure 3.5**) might not be indicative of provenance, but rather a mixture of zircons from more than one megaflood, integrating zircons from more than one source region. In fact, the observed zircon U-Pb distribution in sample 13SI28 could be a mixture of the zircon-age signature observed from single-age samples (**Figure 3.4**) that have several similar age peaks. These patterns indicate the difficulties in assessing provenance using zircon U-Pb data alone without also constraining the depositional age of the deposit.

Despite these complicated processes of sediment reworking, the radiocarbon and luminescence data presented here indicate that there were at last 9 megafloods since 42 ka that deposited sediment in the Siang River (**Table 3.6; Figure 3.6**). Seven of these events identified overlap periods during which ancient glacial lakes are known to have existed in Tibet (**Figure 3.6**; Montgomery et al., 2004; Guangxiang and Qingli, 2012; Liu et al., 2015; Hu et al., 2018). The overlap in timing constraints for some possible outburst flood sources and luminescence age components that we interpret to represent bleaching during megafloods does not indicate a one-to-one correspondence between sources and flood deposits. Nevertheless, our data contribute substantially to the available geochronology of outburst floods in the region, showing the potential for such lakes to fill and empty repeatedly to produce megafloods.

3.6 CONCLUSIONS

Radiocarbon and luminescence data presented here constrain the timing of at least 9 megaflood events from 42 to 1 ka that were previously undocumented in the Siang River valley. The luminescence data indicate that substantial amounts of sediment from megaflood events older than 19 ka were stored on the flood pathway, possibly entrained fluvial or fill terraces or within thick sequences of megaflood sediment observed near tributaries. The luminescence data provide insight into zircon U-Pb distributions observed in megaflood deposit samples that contain several source age populations and show that these data might not represent a signal of provenance, but rather recycled zircons from stored megaflood sediment somewhere along the flood pathway. In the future, numerical megaflood simulations can be applied to predict hydraulic conditions along megaflood pathways where sediment is likely deposited or reworked and eroded, to further constrain patterns observed in zircon and luminescence data. Regardless, our new data from a combination of radiocarbon and luminescence dating applied to slackwater deposits in the Siang valleys shows a history of repeated megaflood events sourced from glacial-lake sources in Tibet that have made a profound geomorphic impact in the eastern Himalaya.

CONCLUSION: THE HISTORY, HYDRAULICS, AND GEOMORPHIC IMPACT OF OUTBURST FLOODS IN THE EASTERN HIMALAYA

The three papers presented here advance our knowledge about the geomorphic impact of extreme outburst floods in the eastern Himalaya by applying new tools to like numerical flood modeling, Bayesian statistics, and single-grain luminescence dating. Flood stimulations have characterized hydraulics through rugged topography to show the extreme potential for erosion in steep segments of the flood pathway and reveal new relationships between flood hydraulics and boulder bar deposition that were previously unknown. Bayesian analyses of the large (n>1400) zircon dataset provides improved resolution of the distribution of zircon ages in slackwater megaflood deposits, providing support to the hypothesis that megafloods preferentially erode rock from the Tsangpo Gorge compared to the historical Yigong outburst flood and modern river flows. This analysis also provides new evidence to suggest that most megafloods were sourced on the Yarlung River to the west of the Tsangpo Gorge, and that megaflood deposit sediment contains reworked sediment from previous floods. Patterns of megaflood sediment recycling are supported by the first radiocarbon and single-grain luminescence ages obtained from slackwater deposits, which also constrain the age of flood sediments from at least 9 megaflood events.

New insight gained from these three chapters sets up future work to continue the study of outburst floods in the region. For example, the modeling approach used to simulate outburst floods is a promising technique that can be used to simulate ancient megaflood events to constrain patterns of erosion and deposition. This is the next step to understanding the distribution of erosion and deposition along megaflood pathways and to further investigate sediment recycling processes that impact slackwater sediments on the Siang River. The methods applied in these chapters can also be applied in other mountainous regions or in other landscapes that experience outburst floods to improve our overall understanding of the impact of these events on Earth or even other planetary bodies including Mars.

REFERENCES

Ahlers, R., Budds, J., Joshi, D., Merme, V., & Zwarteveen, M. (2014). Framing hydropower as green energy: Assessing drivers, risks and tensions in the Eastern Himalayas. Earth Syst. Dyn. Discuss, 5, 1521-1541.

Alho, P., & Aaltonen, J. (2008). Comparing a 1D hydraulic model with a 2D hydraulic model for the simulation of extreme glacial outburst floods. Hydrological Processes: An International Journal, 22(10), 1537-1547.

Alho, P., Baker, V. R., & Smith, L. N. (2010). Paleohydraulic reconstruction of the largest Glacial Lake Missoula draining (s). Quaternary Science Reviews, 29(23-24), 3067-3078.

Allen, S. K., Linsbauer, A., Huggel, C., Randhawa, S. S., Schaub, Y., & Stoffel, M. (2016). Current and Future Glacial Lake Outburst Flood Hazard: Application of GIS-Based Modeling in Himachal Pradesh, India. In Climate Change, Glacier Response, and Vegetation Dynamics in the Himalaya (pp. 181-203). Springer, Cham.

Arboit, F., Collins, A.S., Morley, C.K., King, R., and Amrouch, K. (2016). Detrital zircon analysis of the southwest Indochina terrane, central Thailand: Unravelling the Indosinian orogeny: Geological Society of America Bulletin, p. 1024–1043.

Arcos, M.E.M., & LeVeque, R.J. (2015). Validating Velocities in the GeoClaw Tsunami Model Using Observations near Hawaii from the 2011 Tohoku Tsunami. Pure Applied Geophysics. 172: 849.

Arnold, L.J., Roberts, R.G., Galbraith, R.F., DeLong, S.B. (2009). A revised burial dose estimation procedure for optical dating of young and modern-age sediments. Quat. Geochronol. 4 (4), 306–325.

Auclair, M., Lamothe, M., & Huot, S. (2003). Measurement of anomalous fading for feldspar IRSL using SAR. Radiation measurements, 37(4-5), 487-492.

Bagnold, R.A. (1966). An approach to the sediment transport problem from general physics. US Geol. Surv. Prof. Pap. 422-I, 1–37.

Bajracharya, B., Shrestha, A. B., & Rajbhandari, L. (2007). Glacial lake outburst floods in the Sagarmatha region: hazard assessment using GIS and hydrodynamic modeling. Mountain Research and Development, 27(4), 336-344.

Baker, V. & Milton, D. (1974). Erosion by catastrophic floods on Mars and Earth. Icarus, 23(1), 27-41.

Baker, V. (1973). Paleohydrology and sedimentology of the Lake Missoula flooding in eastern Washington. Geol. Soc. Am. Spec. Pap., 144, 1-79.

Baker, V. (2001). Water and the martian landscape. Nature, 412(6843), 228.

Barbour, J., Stark, C., Lin, C.-W., Chen, H., Horng, M.-J., Ko, C.- P., Yi, T.-C., Tsai, T.-T.,

Chang, W.-S., Lee, S.-P., and Huang, C. (2009). Magnitude-frequency distributions of boundary shear stress along a rapidly eroding bedrock river, Geophys. Res. Lett., 36, L04401.

Bates, P. & De Roo, A. (2000). A simple raster-based model for flood inundation simulation. Journal of Hydrology 236: 54–77.

Baynes, E. R. C., Attal, M., Dugmore, A. J., Kirstein, L. A., & Whaler, K. A. (2015). Geomorphology Catastrophic impact of extreme flood events on the morphology and evolution of the lower Jökulsá á Fjöllum (northeast Iceland) during the Holocene. Geomorphology, 250, 422–436.

Beer, A., Turowski, J. M., & Kirchner, J. W. (2017). Spatial patterns of erosion in a bedrock gorge. Journal of Geophysical Research: Earth Surface, 122(1), 191-214.

Berger, M.J., George, D.L., LeVeque, R.J., & Mandli, K.T. (2011). The GeoClaw software for depth-averaged flows with adaptive refinement. Advances in Water Resources, Vol. 34, pp. 1195-1206.

Bohorquez, P., Carling, P., & Herget, J. (2015). Dynamic simulation of catastrophic late Pleistocene glacial-lake drainage, Altai Mountains, central Asia. International Geology Review, 58(14), 1795-1817.

Booth, A.L., Chamberlain, C.P., Kidd, W.S.F., & Zeitler, P.K. (2009). Constraints on the metamorphic evolution of the eastern Himalayan syntaxis from geochronologic and petrologic studies of Namche Barwa: Geological Society of America Bulletin, v. 121, p. 385–407.

Booth, A.L., Zeitler, P.K., Kidd, W.S.F., Wooden, J., Liu, Y., Idleman, B., Hren, M., and Chamberlain, C.P. (2004). U-Pb zircon constraints on the tectonic evolution of southeastern Tibet, Namche Barwa Area: American Journal of Science, v. 304, p. 889–929.

Botev, Z.I., Grotowski, J.F., and Kroese, D.P. (2010). Kernel density estimation via diffusion. Annals of Statistics, Volume 38, Number 5, pages 2916-2957.

Bracciali, L., Parrish, R.R., Najman, Y., Smye, A. Carter, A., and Wijbrans, J.R. (2016). Plio-Pleistocene exhumation of the eastern Himalayan syntaxis and its domal “pop-up”. Earth-Sci. Rev., 160 (2016), pp. 350-385.

Bretz, J. (1923). The Channeled Scablands of the Columbia Plateau. The Journal of Geology, 31(8), 617-649.

Burg, J.P., Nievergelt, P., Oberli, F., Seward, D., Davy, P., Maurin, J.-C., Diao, Z., & Meier, M. (1998). The Namche Barwa syntaxis: Evidence for exhumation related to compressional crustal folding: Journal of Asian Earth Sciences, v. 16, p. 239–252.

Buylaert, J. P., Jain, M., Murray, A. S., Thomsen, K. J., Thiel, C., & Sohbati, R. (2012). A robust feldspar luminescence dating method for Middle and Late Pleistocene sediments. Boreas, 41(3), 435-451.

Canuti, P., Frassoni, A. and Natale, L. (1994). Failure of the Rio Paute landslide dam. Landslide News, 8, 6–7.

Carling, P., Villanueva, I., Herget, J., Wright, N., Borodavko, P., & Morvan, H. (2010). Unsteady 1D and 2D hydraulic models with ice-dam break for quaternary megaflood, Altai Mountains, southern Siberia: Global and Planetary Change, 70(1), p. 24–34.

Carling, P.A. (1996a). Morphology, sedimentology and palaeohydraulic significance of large gravel dunes, Altai Mountains, Siberia. Sedimentology, 43(4), 647-664.

Carling, P.A. (1996b). A preliminary palaeohydraulic model applied to late-quaternary gravel dunes: Altai mountains, Siberia, in Branson, J., Gregory, K.J., and Brown, A.D., eds., Global continental changes: The context of palaeohydrology, Journal of Geology, Volume 115: Geological Society of London Special Publication, p. 165–179.

Carling, P.A., Kirkbride, A.D., Parnachov, S., Borodavko, P.S., Berger, G.W. (2002). Late Quaternary catastrophic flooding in the Altai Mountains of south-central Siberia: a synoptic overview and an introduction to flood deposits sedimentology. Special Publ. Int. Assoc. Sedimentol. 32, 17-35.

Carrivick, J. L. (2006). Application of 2D hydrodynamic modelling to high-magnitude outburst floods: An example from Kverkfjöll, Iceland. Journal of Hydrology, 321(1–4), 187–199.

Carrivick, J. L., & Tweed, F. S. (2016). A global assessment of the societal impacts of glacier outburst floods. *Global and Planetary Change*, *144*, 1-16.

Carter, C.L. & Anderson, R.S. (2006). Fluvial erosion of physically modeled abrasion dominated slot canyons. Geomorphology 81 (1–2), 89–113.

Chapman, M.G., Gudmundsson, M.T. Russell, A.J., Hare, T.M. (2003). Possible Juventae Chasma sub ice volcanic eruptions and Maja Valles ice outburst floods on Mars: implications of Mars Global Surveyor crater densities, geomorphology, and topography. J. Geophys. Res.: Planets, 108 (2003).

Chatanantavet, P. & Parker, G. (2008). Experimental study of bedrock channel alluviation under varied sediment supply and hydraulic conditions. Water Resour. Res. 44 (12), W12446.

Chen, Y., Aitchison, J. C., Zong, Y., & Li, S. H. (2016). OSL dating of past lake levels for a large dammed lake in southern Tibet and determination of possible controls on lake evolution. Earth Surface Processes and Landforms, 41(11), 1467-1476.

Chen, Y., Huang, S., Lin, Y., Liu, J., Chung, L., Lai, K., Zhao, S., Yin, G., & Cao, Z. (2008). Holocene megafloods? Stories of the lacustrine strata along the Nyang River, Tibet: American Geophysical Union Fall Meeting 2008, abs. PP21A-1404.

Cina, S. E., Yin, A., Grove, M., Dubey, C. S., Shukla, D. P., Lovera, O. M., Foster, D. A. (2009). Gangdese arc detritus within the eastern Himalayan Neogene foreland basin: Implications for the Neogene evolution of the Yalu-Brahmaputra River system. *Earth and Planetary Science Letters*, *285*(1–2), 150–162.

Clarke, G. K., Leverington, D. W., Teller, J. T., & Dyke, A. S. (2004). Paleohydraulics of the last outburst flood from glacial Lake Agassiz and the 8200 BP cold event. Quaternary Science Reviews, 23(3-4), 389-407.

Clawpack Development Team. (2017). Clawpack Version 5.3.0, http://www.clawpack.org.

Cook, A. and Merwade, V. (2009). Effect of topographic data, geometric configuration and modeling approach on flood inundation mapping. J. Hydrol., Vol.377, Nos.1–2, pp. 131–142.

Cook, K. L., Andermann, C., Gimbert, F., Adhikari, B. R., & Hovius, N. (2018). Glacial lake outburst floods as drivers of fluvial erosion in the Himalaya. Science, 362(6410), 53-57.

Costa, J. E. and Schuster, R. L. (1991). Documented Historical Landslide Dams from Around the World. U.S. Geological Survey Open-File Report 91–239.

Costa, J.E., & Schuster, R.L., (1988). The formation and failure of natural dams. Geological Society of America Bulletin, Vol. 100, 1054– 1068.

Datta, B., & Singh, V.P. (2004). Hydrology in The Brahmaputra Basin Water Resources, ed. Singh, V.P., et al., pp. 139-195, Dordrecht, Boston.

de Ferranti, J. (2014). 3-arc second digital elevation data. http://viewfinderpanoramas.org/dem3.html

DeCelles, P. G., Castañeda, I. S., Carrapa, B., Liu, J., Quade, J., Leary, R., & Zhang, L. (2018). Oligocene-Miocene Great Lakes in the India-Asia Collision Zone. *Basin Research*, *30*, 228–247.

Delaney, K. B. & Evans, S.G. (2011). Rockslide dams in the northwestern Himalayas (Pakistan, India) and adjacent Pamir Mountains (Afghanistan, Tajikistan), Central Asia in Natural and Artificial Rockslide Dams. Lecture notes in the Earth Sciences vol. 133. Springer, Heidelburg, pp. 205-242.

Delaney, K. B. & Evans, S.G. (2015). The 2000 Yigong landslide (Tibetan Plateau), rockslide-dammed lake and outburst flood: Review, remote sensing analysis, and process modelling. Geomorphology, 246, 377-393.

Denlinger, R. P., & O'Connell, D. R. H. (2009). Simulations of cataclysmic outburst floods from Pleistocene Glacial Lake Missoula. Geological Society of America Bulletin, 122(5–6), 678–689.

Denlinger, R.P., George, D.L., Cannon, C.M., Waitt, R.B., O'Connor, J.E. (2017). Modeling cataclysmic outburst floods from Pleistocene glacial lake Missoula. Geological Society of America Abstracts with Programs. Vol. 49, No. 6.

Denlinger, R.P., O'Connell, D.R.H., & House, P.K. (2002). Robust determination of stage and discharge: An example from an extreme flood on the Verde River, Arizona, in Ancient floods and modern hazards: principles and application of paleoflood hydrology, Vol. 5, edited by Webb, R.H., et al., pp. 127-146, AGU, Washington D.C.

Ding, L., Zhong, D., Yin, A., Kapp, P., & Harrison, T.M. (2001). Cenozoic structural and metamorphic evolution of the eastern Himalayan syntaxis (Namche Barwa): Earth and Planetary Science Letters, v. 192, p.

Duller, G. T. (2008). Single‐grain optical dating of Quaternary sediments: why aliquot size matters in luminescence dating. Boreas, 37(4), 589–612.

Dussaillant, A., Benito, G., Buytaert, W., Carling, P., Meier, C., & Espinoza, F. (2010). Repeated glacial-lake outburst floods in Patagonia: an increasing hazard?. *Natural hazards*, *54*(2), 469-481.

Enkelmann, E., Ehlers, T. A., Zeitler, P. K., & Hallet, B. (2011). Denudation of the Namche Barwa antiform, eastern Himalaya. *Earth and Planetary Science Letters*, *307*(3–4), 323–333.

Evans, S.G. (1986). The maximum discharge of outburst floods caused by the breaching of man-made and natural dams. Can. Geotech. J. 23, 385–387.

Evans, S.G., & Delaney, K.B. (2011). Characterization of the 2000 Yigong Zangbo River (Tibet) Landslide Dam and Impoundment by Remote Sensing, in Natural and Artificial Rockslide Dams, Vol. 133, edited by Evans, S., et al., pp. 543–559, Berlin.

Feathers, J. K., & Nami, H. G. (2018). Luminescence Dating of Late Pleistocene and Holocene Sediments in Uruguay. Latin American Antiquity, 29(3), 495-513.

Ferguson, R. I., & Church, M. (2004). A simple universal equation for grain settling velocity. Journal of sedimentary Research, 74(6), 933-937.

Fiebig, M., & Preusser, F. (2007). Investigating the amount of zeroing in modern sediments of River Danube, Austria. Quaternary Geochronology, 2(1-4), 143-149.

Filleaudeau, P. Y., Mouthereau, F., & Pik, R. (2012). Thermo-tectonic evolution of the south-central Pyrenees from rifting to orogeny: Insights from detrital zircon U/Pb and (U-Th)/He thermochronometry. Basin Research, 24(4), 401–417.

Finnegan, N. J., Hallet, B., Montgomery, D. R., Zeitler, P. K., Stone, J. O., Anders, a. M., & Yuping, L. (2008). Coupling of rock uplift and river incision in the Namche Barwa-Gyala Peri massif, Tibet. Geological Society of America Bulletin, 120(1–2), 142–155.

Frey, H., Huggel, C., Baer, P., Chisolm, R. E., McArdell, B., Cochachin, A., & Portocarrero, C. (2018). Multi-source glacial lake outburst flood hazard assessment and mapping for Huaraz, Cordillera Blanca, Peru. Frontiers in Earth Science, 6, 210.

Froehlich, D. C. (2016). Predicting peak discharge from gradually breached embankment dam. Journal of Hydrologic Engineering, 21(11), 04016041.

Fuller, T.K. (2014). Field, Experimental and Numerical Investigations into the Mechanisms and Drivers of Lateral Erosion in Bedrock Channels. (PhD). University of Minnesota, Minneapolis, MN.

Galbraith, R. F., & Roberts, R. G. (2012). Statistical aspects of equivalent dose and error calculation and display in OSL dating: an overview and some recommendations. Quaternary Geochronology, 11, 1-27.

Galbraith, R.F., Roberts, R.G., Laslett, G.M., Yoshida, H., Olley, J.M., (1999). Optical dating of single and multiple grains of quartz from Jinmium rock shelter, northern Australia: Part I, experimental design and statistical models. Archaeometry 41 (2), 339–364.

Gallagher, K., Charvin, K., Nielsen, S., Sambridge, M., and Stephenson, J., (2009). Markov chain Monte Carlo (MCMC) sampling methods to determine optimal models, model resolution and model choice for earth science problems: Marine and Petroleum Geology, v. 26, p. 525–535.

Galland, J.C., Goutal, N., Hervouet, J.-M. (1991). TELEMAC—a new numerical-model for solving shallow-water equations. Advances in Water Resources 14 (3), 138–148.

Galy, V., Peucker-Ehrenbrink, B., & Eglinton, T. (2015). Global carbon export from the terrestrial biosphere controlled by erosion. Nature, 521(7551), 204.

Garcia-Castellanos, D., & O'Connor, J. E. (2018). Outburst floods provide erodability estimates consistent with long-term landscape evolution. Scientific reports, 8(1), 10573.

Gehrels, G. E., Yin, A., & Wang, X. F. (2003). Detrital-zircon geochronology of the northeastern Tibetan plateau. Geological Society of America Bulletin, 115(7), 881-896.

Gehrels, G., Kapp, P., Decelles, P., Pullen, A., Blakey, R., Weislogel, A., & Yin, A. (2011). Detrital zircon geochronology of pre-Tertiary strata in the Tibetan-Himalayan orogen. *Tectonics*, *30*(5), 5016.

George, D.L. (2011). Adaptive finite volume methods with well-balanced Riemann solvers for modeling floods in rugged terrain: Application to the Malpasset dam-break flood (France, 1959). International Journal for Numerical Methods in Fluids, 66(8), 1000-1018.

Goswami, D. C. (1985). Brahmaputra River, Assam, India: Physiography, Basin Denudation, and Channel Aggradation. Water Resources Research, 21(7), 959–978.

Goswami, K., Rawat, M., Jaiswal, M. K., & Kale, V. S. (2019). Luminescence chronology of late-Holocene palaeofloods in the upper Kaveri basin, India: An insight into the climate–flood relationship. The Holocene, 0959683619831436.

Goudge, T. A., & Fassett, C. I. (2018). Incision of Licus Vallis, Mars, from multiple lake overflow floods. Journal of Geophysical Research: Planets, 123, 405–420.

Guangxiang, Y., & Qingli, Z. (2012). Glacier-dammed lake in southeastern Tibetan Plateau during the Last Glacial Maximum. Journal of the Geological Society of India, 79(3), 295-301.

Guangxiang, Z. Q. Y. Z. Y., & Xitao, S. Y. Z. L. Z. (2007). Songzong lake: an ice-dammed lake of last glacial maximum in Purlung Tsangpo River, Southeast Tibet. Quaternary Sciences, 1, 9.

Han, Z.S. (2003). Large-scale landslide-debris avalanche in Tibet, China (1) April–June 2000 Yigong Landslide, Tibet China. Landslide News 14–15, 22–23.

Hartshorn, K, Hovius, N, Dade, W.B., and Slingerland, R.L. (2002). Climate-driven bedrock incision in an active mountain belt. Science 297, 2036-2038.

He, Z., Long, H., Yang, L., & Zhou, J. (2019). Luminescence dating of a fluvial sequence using different grain size fractions and implications on Holocene flooding activities in Weihe Basin, central China. Quaternary Geochronology, 49, 123-130.

Henderson, F.M. (1966). Flow resistance in Open Channel Flow, edited by MacMillan Publishing CO., pp. 96-101, New York.

Herget, J., & Agatz, H. (2003). Modelling ice-dammed lake outburst floods in the Altai Mountains (Siberia) with HEC-RAS. In Thorndycraft, VR, Benito, G., Barriendos, M. and Llasat, MC, Applications in flood risk assessment: PHEFRA Workshop, Barcelona, Prodeedings (pp. 177-181).Hewitt, K. (1968). Record of natural damming and related floods in the Upper Indus Basin. Indus, 10 (3), 11–19.

Horritt, & Bates. (2002). Evaluation of 1D and 2D numerical models for predicting river flood inundation. Journal of Hydrology, 268(1), 87-99.

Hu, G., Yi, C. L., Zhang, J. F., Liu, J. H., & Jiang, T. (2015). Luminescence dating of glacial deposits near the eastern Himalayan syntaxis using different grain-size fractions. Quaternary Science Reviews, 124, 124–144.

Hu, H. P., Feng, J. L., & Chen, F. (2017). δ18O and δ13C in fossil shells of Radix sp. from the sediment succession of a dammed palaeo-lake in the Yarlung Tsangpo valley, Tibet, China. Boreas, 46(3), 412–427.

Hu, H. P., Feng, J. L., & Chen, F. (2018). Sedimentary records of a palaeo-lake in the middle Yarlung Tsangpo: Implications for terrace genesis and outburst flooding. Quaternary Science Reviews, 192, 135-148.

Huang, S. Y., Chen, Y. G., Burr, G. S., Jaiswal, M. K., Lin, Y. N., Yin, G., and Cao, Z. (2014). Late Pleistocene sedimentary history of multiple glacially dammed lake episodes along the Yarlung-Tsangpo river, southeast Tibet. Quaternary research, 82(2), 430-440.

Huang, W., Cao, Z., Pender, G., Liu, Q., & Carling, P. (2015). Coupled flood and sediment transport modelling with adaptive mesh refinement. Science China Technological Sciences, 58(8), 1425-1438.

Huntley, D.J., Lamothe, M. (2001). Ubiquity of anomalous fading in K-feldspars and the measurement and correction for it in optical dating. Canadian Journal of Earth Sciences 38, 1093-1106.

Jasra, A., Stephens, D., Gallagher, K., and Holmes, C., (2006). Bayesian mixture modelling in geochronology via Markov chain Monte Carlo: Mathematical Geology, v. 38, p. 269–300.

Kaiser, K., Lai, Z., Schneider, B., & Junge, F. W. (2010). Late Pleistocene genesis of the middle Yarlung Zhangbo Valley, southern Tibet (China), as deduced by sedimentological and luminescence data. Quaternary Geochronology, 5(2-3), 200-204.

Kale, V., Achyuthan, H., Jaiswal, M., & Sengupta, S. (2010). Palaeoflood records from upper Kaveri River, southern India: evidence for discrete floods during Holocene. Geochronometria, 37(1), 49-55.

King, J., Loveday, I. and Schuster, R. L. (1989). The 1985 Bairaman landslide dam and resulting debris flow, Papua New Guinea. Quarterly Journal ofEngineering Geology, London, 22, 257–270.

Kirkbride, M. P., Dugmore, A. J., & Brazier, V. (2006). Radiocarbon dating of mid-Holocene megaflood deposits in the Jokulsa a Fjollum, north Iceland. The Holocene, 16(4), 605-609.

Komatsu, G., Arzhannikov, S.G., Gillespie, A.R., Burke, R.M., Miyamoto, H., & Baker, V.R. (2009). Quaternary paleolake formation and cataclysmic flooding along the upper Yenisei River. Geomorphology 104, 143–164.

Korup, O. (2002). Recent research on landslide dams: a literature review with special attention to New Zealand. Progress in Physical Geography 26: 206–235.

Korup, O. (2005). Geomorphic hazard assessment of landslide dams in South Westland, New Zealand: fundamental problems and approaches. Geomorphology 66: 167–188.

Korup, O., & Montgomery, D. R. (2008). Tibetan plateau river incision inhibited by glacial stabilization of the Tsangpo gorge. Nature, 455(7214), 786–789.

Korup, O., Montgomery, D. R., & Hewitt, K. (2010). Glacier and landslide feedbacks to topographic relief in the Himalayan syntaxes. *Proceedings of the National Academy of Sciences of the United States of America*, *107*(12), 5317–5322.

Kougkoulos, I., Cook, S. J., Edwards, L. A., Clarke, L. J., Symeonakis, E., Dortch, J. M., & Nesbitt, K. (2018). Modelling glacial lake outburst flood impacts in the Bolivian Andes. Natural Hazards, 1-24.

Kunz, A., Pflanz, D., Weniger, T., Urban, B., Krüger, F., & Chen, Y. G. (2014). Optically stimulated luminescence dating of young fluvial deposits of the Middle Elbe River Flood Plains using different age models. Geochronometria, 41(1), 36-56.

Lamb, M. & Fonstad, M. (2010). Rapid formation of a modern bedrock canyon by a single flood event. Nature Geoscience, 3(7), 477-481.

Lamb, M. P., Dietrich, W. E., & Venditti, J. G. (2008a). Is the critical shields stress for incipient sediment motion dependent on channel-bed slope? Journal of Geophysical Research: Earth Surface, 113(2), 1–20.

Lamb, M. P., Finnegan, N. J., Scheingross, J. S., & Sklar, L. S. (2015). New insights into the mechanics of fluvial bedrock erosion through flume experiments and theory. Geomorphology, 244, 33–55.

Lamb, M., & Fonstad, M. (2010). Rapid formation of a modern bedrock canyon by a single flood event. Nature Geoscience, 3(7), 477– 481.

Lamb, M., Dietrich, W., Aciego, S., Depaolo, D., & Manga, M. (2008b). Formation of Box Canyon, Idaho, by megaflood: Implications for seepage erosion on Earth and Mars. Science, 320(5879), 1067-70.

Lamb, M.P., Dietrich, W.E., Sklar, L.S. (2008c). A model for fluvial bedrock incision by impacting suspended and bed load sediment. J. Geophys. Res. Earth Surf. 113 (F3).

Lang, K. A., & Huntington, K. W. (2014). Antecedence of the Yarlung–Siang–Brahmaputra River, eastern Himalaya. *Earth and Planetary Science Letters*, *397*, 145–158.

Lang, K. A., Huntington, K. W., & Montgomery, D. R. (2013). Erosion of the Tsangpo Gorge by megafloods, Eastern Himalaya. Geology, 41(9), 1003–1006.

Lang, K.A., Huntington, K.W., Burmester, R., and Housen, B. (2016). Rapid exhumation of the eastern Himalayan syntaxis since the Late Miocene: Geological Society of America Bulletin, v. 128, p. 1403–1422.

Langston, A. L., & Tucker, G. E. (2018). Developing and exploring a theory for the lateral erosion of bedrock channels for use in landscape evolution models. Earth Surface Dynamics, 6(1), 1–27.

Larsen, I. J., & Montgomery, D. R. (2012). Landslide erosion coupled to tectonics and river incision. Nature Geoscience, 5(7), 468– 473.

Larsen, I.J., & Lamb, M. (2016). Progressive incision of the Channeled Scablands by outburst floods. Nature, 538(7624), 229–232. LeVeque, R.J., George, D.L. & Berger, M.J. (2011). Tsunami modeling with adaptively refined finite volume methods. Acta Numerica, pp. 211-289.

Liang, Y.H., Chung, S.L., Liu, D., Xu, Y., Wu, F.Y., Yang, J.H., Wang, Y., Lo, C.H. (2008). Detrital zircon evidence from Burma for reorganization of the eastern Himalayan river system. Am. J. Sci. 308, 618–638.

Licht, A., Pullen, A., Kapp, P., Abell, J., & Giesler, N. (2016). Eolian cannibalism: Reworked loess and fluvial sediment as the main sources of the Chinese Loess Plateau. *Geological Society of America Bulletin*, *128*(5–6), 944–956.

Liu, W., Lai, Z., Hu, K., Ge, Y., Cui, P., Zhang, X., & Liu, F. (2015). Age and extent of a giant glacial-dammed lake at Yarlung Tsangpo gorge in the Tibetan Plateau. Geomorphology, 246, 370-376.

Liu, W., Zhou, G. G., Ge, Y., & Huang, R. (2018). Gradual late stage deepening of Gega ice-dammed lake, Tsangpo gorge, southeastern Tibet, indicated by preliminary sedimentary rock magnetic properties. Acta Geophysica, 66(5), 907-914.

Liu, Y., Montgomery, D. R., Hallet, B., Tang, W., Zhang, J. L., & Zhang, X. Y. (2006). Quaternary glacier blocking events at the entrance of Yarlung Zangbo Great Canyon, Southeast Tibet. Quaternary Sciences, 26(1), 52-62.

Lopes, C., & Mix, A. C. (2009). Pleistocene megafloods in the northeast Pacific. Geology, 37(1), 79-82.

Macinnes, B.T., Gusman, A.R., Leveque, R.J., & Tanioka, Y. (2013). Comparison of Earthquake Source Models for the 2011 Tohoku Event Using Tsunami Simulations and Near-Field Observations, 103(2), 1256–1274.

Makuluni, P., & Barham, M. (2018). Zircon grain shape holds provenance information: A case study from southwestern Australia. Geological Journal, (March), 1–15.

Malde, H., & Geological Survey issuing body. (1968). The catastrophic late Pleistocene Bonneville flood in the Snake River Plain, Idaho. USGS Professional Paper, 596, pp. 1-52.

Malloy, M. (2004). Rapid erosion at the Tsangpo knickpoint and exhumation of southeastern Tibet [M.S. thesis]: Lehigh University, 82 p.

Mandli, K.T., Ahmadia, A.J., Berger, M., Calhoun, D., George, L., Hadjimichael, Y., Ketcheson, D.I., Lemoine, G.I., & Leveque, R. J. (2016). Clawpack: building on an open source ecosystem for solving hyperbolic PDEs. PeerJ Computer Science, 1-27.

Manning, R. (1891). On the flow of water in open channels and pipes. Transactions, Institution of Civil Engineers of Ireland 20: 161–207.

Margold, M., Jansen, J. D., Codilean, A. T., Preusser, F., Gurinov, A. L., Fujioka, T., & Fink, D. (2018). Repeated megafloods from glacial Lake Vitim, Siberia, to the Arctic Ocean over the past 60,000 years. Quaternary Science Reviews, 187, 41–61.

Margold, M., Jansson, K. N., Stroeven, A. P., & Jansen, J. D. (2011). Glacial Lake Vitim, a 3000-km 3 outburst flood from Siberia to the Arctic Ocean. Quaternary Research, 76(3), 393-396.

McLaren, S. J., Al-Juaidi, F., Bateman, M. D., & Millington, A. C. (2009). First evidence for episodic flooding events in the arid interior of central Saudi Arabia over the last 60 ka. Journal of Quaternary Science: Published for the Quaternary Research Association, 24(2), 198-207.

Medialdea, A., Porat, N., & Benito, G. (2011). Optically stimulated luminescence characteristics of modern flash-flood deposits in small mountain catchments. Spectroscopy Letters, 44(7-8), 530-534.

Miyamoto, H., Itoh, K., Komatsu, G., Baker, V., Dohm, J., Tosaka, H. & Sasaki, S. (2006). Numerical simulations of large-scale cataclysmic floodwater: A simple depth-averaged model and an illustrative application. Geomorphology, 76(1), 179-192.

Montgomery, D.R., Hallet, B., Yuping, L., Finnegan, N., Anders, A., Gillespie, A., & Greenberg, H.M. (2004). Evidence for holocene megafloods down the Tsangpo River gorge, southeastern Tibet. Quaternary Research, 62(2), 201–207.

Murton, J. B., Bateman, M. D., Dallimore, S. R., Teller, J. T., & Yang, Z. (2010). Identification of Younger Dryas outburst flood path from Lake Agassiz to the Arctic Ocean. Nature, 464(7289), 740.

O'Connor, J.E., & Beebee, R.A. (2009). Floods from natural rock-material dams. In: Burr, DM,

Carling, PA, Baker, VR (eds) Megaflooding on Earth and Mars. Cambridge University Press, 128–171.

O'Connor, J.E., Clague, J.J., Walder, J.S., Manville, V., & Beebee, R.A. (2013). Outburst Floods in Treatise on Geomorphology, Vol. 9, edited by Shroder, J.F., pp. 475-510.

O'Connor, J. E., & Baker, V. R. (1992). Magnitudes and implications of peak discharges from glacial Lake Missoula. Geological Society of America Bulletin, 104(3), 267-279.

O'Connor, J. E., & Beebee, R. A. (2009). Floods from natural rock-material dams. In P. A. Carling, & V. R. Baker (Eds.), Burr, DM (pp. 128– 171). Megaflooding on Earth and Mars, Cambridge: Cambridge University Press.

O'Connor, J., 1993, Hydrology, hydraulics, and geomorphology of the Bonneville flood. Geological Society of America Special Paper 274, p. 1-83.

Ouimet, W. B., Whipple, K. X., Royden, L. H., Sun, Z., & Chen, Z. (2007). The influence of large landslides on river incision in a transient landscape: Eastern margin of the Tibetan Plateau (Sichuan, China). Geological Society of America Bulletin, 119(11-12), 1462-1476.

Owen, L. A. & Benn, D. I. (2005). Equilibrium-line altitudes of the Last Glacial Maximum for the Himalaya and Tibet: An assessment and evaluation of results. Quat. Int. 138–139, 55–78.

Owen, L. A., Finkel, R. C., & Caffee, M. W. (2002). A note on the extent of glaciation throughout the Himalaya during the global Last Glacial Maximum. Quaternary Science Reviews, 21(1-3), 147-157.

Parrish, R. R., & Hodges, K. V. (1996). Isotopic constraints on the age and provenance of the Lesser and Greater Himalayan sequences, Nepalese Himalaya. *Bulletin of the Geological Society of America*, *108*(7), 904–911.

Pelletier, J. D., Sweeney, K. E., Roering, J. J., & Finnegan, N. J. (2015). Controls on the geometry of potholes in bedrock channels. Geophysical Research Letters, 42(3), 797-803.

Perron, J. Taylor, & Venditti, Jeremy G. (2016). Earth science: Megafloods downsized. Nature, 538(7624), 174-175.

Perrot, M., Tremblay, A., & David, J. (2017). Detrital zircon U-Pb geochronology of the Magog Group, southern Quebec - Stratigraphic and tectonic implications for the Quebec Appalachians. American Journal of Science, 317(10), 1049–1094.

Ping, Z. P. L. X. K. (2008). Evidence for glacial movement since last glacial period in the Great Canyon, Yarlung Zangbo, SE Tibet and its tectono—environmental implications [J]. Chinese Journal of Geology (Scientia Geologica Sinica), 3, 014.

Plaza-Nieto, G., Yepes, H. and Schuster, R. L. (1990). Landslide dam on the Pisque River, northern Ecuador. Landslide News, 4, 2–4.

Pullen, A., Ibáñez-Mejía, M., Gehrels, G. E., Ibáñez-Mejía, J. C., & Pecha, M. (2014). What happens when n= 1000? Creating large-n geochronological datasets with LA-ICP-MS for geologic investigations. *J. Anal. At. Spectrom.*, *29*(6), 971–980.

Reid, H. E., Williams, R. D., Brierley, G. J., Coleman, S. E., Lamb, R., Rennie, C. D., & Tancock, M. J. (2019). Geomorphological effectiveness of floods to rework gravel bars: Insight from hyperscale topography and hydraulic modelling. Earth Surface Processes and Landforms, 44(2), 595-613.

Reimer, P. J., Bard, E., Bayliss, A., Beck, J. W., Blackwell, P. G., Ramsey, C. B., & Grootes, P. M. (2013). IntCal13 and Marine13 radiocarbon age calibration curves 0–50,000 years cal BP. Radiocarbon, 55(4), 1869-1887.

Rhodes, E. J. (2011). Optically stimulated luminescence dating of sediments over the past 200,000 years. Annual Review of Earth and Planetary Sciences, 39, 461-488.

Rhodes, E. J. (2015). Dating sediments using potassium feldspar single-grain IRSL: initial methodological considerations. Quaternary International, 362, 14-22.

Richardson, K., Carling, P.A., (2006). The hydraulics of a straight bedrock channel: insights from solute dispersion studies. Geomorphology 82 (1), 98–125.

Richardson, S.D., & Reynolds, J.M. (2000a). An overview of glacial hazards in the Himalayas. Quat. Int. 65 (66), 31–47.

Risley, J. C., Walder, J. S., & Denlinger, R. P. (2006). Usoi dam wave overtopping and flood routing in the Bartang and Panj Rivers, Tajikistan. Natural Hazards, 38(3), 375-390.

Roberts, S., Nielsen, O., Gray, D., Sexton, J. & Davies, G. (2015). ANUGA User Manual. Release 2.0. https://github.com/GeoscienceAustralia/anuga_core/raw/master/ doc/anuga_user_manual.pdf

Ruiz-Villanueva, V., Allen, S., Arora, M., Goel, N. K., & Stoffel, M. (2017). Recent catastrophic landslide lake outburst floods in the Himalayan mountain range. Progress in Physical Geography, 41(1), 3–28.

Salvatore, G., Andrea, P., Ettore, A., and Nardi, F. (2013). Flood mapping in ungagged basins using fully continuous hydrologic-hydraulic modeling, J. Hydrol., Vol.487, pp. 39-47.

Sattar, A., Goswami, A., & Kulkarni, A. V. (2018). Hydrodynamic modeling of glacial lake outburst flood (GLOF) and its impact on a Hydropower Station-A case study at the upper Alaknanda Basin, Central Himalaya. In EGU General Assembly Conference Abstracts (Vol. 20, p. 1575).

Saylor, J. E., & Sundell, K. E. (2016). Quantifying comparison of large detrital geochronology data sets. Geosphere, 12, (203-220). *Geosphere*, *12*(6), 1881–1881.

Schneider, D., Huggel, C., Cochachin, A., Guillén, S., & García, J. (2014). Mapping hazards from glacier lake outburst floods based on modelling of process cascades at Lake 513, Carhuaz, Peru. Advances in Geosciences, 35, 145-155.

Schwanghart, W., Ryan, M., & Korup, O. (2018). Topographic and seismic constraints on the vulnerability of Himalayan hydropower. Geophysical Research Letters, 45(17), 8985-8992.

Schwanghart, W., Worni, R., Huggel, C., Stoffel, M., & Korup, O. (2016). Uncertainty in the Himalayan energy–water nexus: Estimating regional exposure to glacial lake outburst floods. Environmental Research Letters, 11(7), 074005.

Seward, D., & Burg, J. (2008). Growth of the Namche Barwa Syntaxis and associated evolution of the Tsangpo Gorge: Constraints from structural and thermochronological data: Tectonophysics, v. 451, p. 282–289.

Shang, Y., Yang, Z., Li, L., Liu, D., Liao, Q., & Wang, Y. (2003). A super-large landslide in Tibet in 2000: background, occurrence, disaster, and origin. Geomorphology, 54(3-4), pp. 225–243.

Shang, Y., Yang, Z., Li, L., Liu, D., Liao, Q., & Wang, Y. (2003). A super-large landslide in Tibet in 2000: background, occurrence, disaster, and origin. Geomorphology, 54(3-4), pp. 225–243.

Shean, D. (2017). High Mountain Asia 8-meter DEM Mosaics Derived from Optical Imagery, Version 1. Boulder, Colorado USA. NASA National Snow and Ice Data Center Distributed Active Archive Center.

Shrestha, A. B., Eriksson, M., Mool, P., Ghimire, P., Mishra, B., & Khanal, N. R. (2010). Glacial lake outburst flood risk assessment of Sun Koshi basin, Nepal. Geomatics, Natural Hazards and Risk, 1(2), 157-169.

Singh, A. K., & Jaiswal, M. K. (2019). Application of luminescence age models to heterogeneously bleached quartz grains from flood deposits in Tamilnadu, southern India: Reconstruction of past flooding. Quaternary International, 513, 95-106.

Sklar, L.S., Dietrich, W.E., (2004). A mechanistic model for river incision into bedrock by saltating bed load. Water Resour. Res. 40 (6).

Song, Z., Zhen-han, W., Xi-tao, Z., & Ke-yan, X. (2013). Glacial dammed lakes in the Tsangpo River during late Pleistocene, southeastern Tibet. Quaternary international, 298, 114-122.

Spencer, C. J., & Kirkland, C. L. (2016). Visualizing the sedimentary response through the orogenic cycle: A multidimensional scaling approach. Lithosphere, 8(1), 29–37.

Srivastava, P., Bhakuni, S.S., Luirei, K., Misra, D.K. (2009). Fluvial records from the Brahmaputra River exit, NE Himalaya: climate-tectonic interplay during Late Pleistocene-Holocene. Journal of Quaternary Science 24, 175-188.

Srivastava, P., Kumar, A., Chaudhary, S., Meena, N., Sundriyal, Y. P., Rawat, S., Ziegler, A. D. (2017). Paleofloods records in Himalaya. Geomorphology, 284, 17–30.

Stewart, R. J., Hallet, B., Zeitler, P. K., Malloy, M. A., Allen, C. M., & Trippett, D. (2008). Brahmaputra sediment flux dominated by highly localized rapid erosion from the easternmost Himalaya. *Geology*, *36*(9), 711–714.

Tewari, P. (2004). A study of soil erosion in Pasighat town (Arunachal Pradesh) India, Natural Hazards, 32, 257-275.

Tinkler, K.J., Wohl, E. (1998). A primer on bedrock channels. In: Tinkler, K.J., Wohl, E.E. (Eds.), Rivers Over Rock: Fluvial Processes in Bedrock Channels. Geophysical Monograph Series 107. American Geophysical Union, Washington DC, pp. 1–18.

Tsukamoto, S., Kataoka, K., & Miyabuchi, Y. (2013). Luminescence dating of volcanogenic outburst flood sediments from Aso volcano and tephric loess deposits, southwest Japan. Geochronometria, 40(4), 294-303.

Turowski, J. M., Hovius, N., Meng-Long, H., Lague, D., & Men-Chiang, C. (2008). Distribution of erosion across bedrock channels. Earth Surface Processes and Landforms, 33, 353–363.

Turowski, J. M., Lague, D., & Hovius, N. (2007). Cover effect in bedrock abrasion: A new derivation and its implications for the modeling of bedrock channel morphology. Journal of Geophysical Research: Earth Surface, 112(F4).

Turzewski, M. D., Huntington, K. W., & LeVeque, R. J. (2019). The geomorphic impact of outburst floods: Integrating observations and numerical simulations of the 2000 Yigong flood, eastern Himalaya. Journal of Geophysical Research: Earth Surface. (2019), (May), 1056–1079.

Vermeesch, P. (2013). Multi-sample comparison of detrital age distributions. *Chemical Geology*, *341*, 140–146.

Vermeesch, P. (2018). Dissimilarity measures in detrital geochronology. Earth-Science Reviews, 178, 310-321.

Vermeesch, P., and Garzanti, E., (2015). Making geological sense of “Big Data” in sedimentary provenance analysis: Chemical Geology, v. 409, p. 20–27.

Waitt, R. B. (2016). Megafloods and Clovis cache at Wenatchee, Washington. Quaternary Research, 85(3), 430-444.

Walder, J. S., & O'Connor, J. E. (1997). Methods for predicting peak discharge of floods caused by failure of natural and constructed earthen dams. Water Resources Research, 33(10), 2337-2348.

Wang, J. P., & Liang, Q. (2011). Testing a new adaptive grid-based shallow flow model for different types of flood simulations. Journal of Flood Risk Management, 4(2), 96-103.

Wang, P., Scherler, D., Avouac, J., Zhang, Y., & Shi, D. (2014). Tectonic control of Yarlung Tsangpo Gorge revealed by a buried canyon in Southern Tibet, *263901*(2013).

Wang, W., Gao, Y., Anacona, P. I., Lei, Y., Xiang, Y., Zhang, G., & Lu, A. (2018). Integrated hazard assessment of Cirenmaco glacial lake in Zhangzangbo valley, Central Himalayas. Geomorphology, 306, 292-305.

Weidinger, JT. (2006). Landslide dams in the high mountains of India, Nepal and China: stability and life span of their dammed lakes. Italian Journal of Engineering Geology and Environment 1: 67–80.

Westoby, M. J., Brasington, J., Glasser, N. F., Hambrey, M. J., Reynolds, J. M., Hassan, M. A. A. M., & Lowe, A. (2015). Numerical modelling of glacial lake outburst floods using physically based dam-breach models. Earth Surface Dynamics, 3(1), 171–199.

Westoby, M. J., Glasser, N. F., Brasington, J., Hambrey, M. J., Quincey, D. J., & Reynolds, J. M. (2014). Modelling outburst floods from moraine-dammed glacial lakes. Earth-Science Reviews, 134, 137–159.

Whipple, K. X., DiBiase, R. A., & Crosby, B. T. (2013). Bedrock rivers. In *Treatise on geomorphology* (pp. 550-573). Elsevier Inc.

Whipple, K. X., Hancock, G. S., & Anderson, R. S. (2000). River incision into bedrock: Mechanics and relative efficacy of plucking, abrasion, and cavitation. Geological Society of America Bulletin, 112(3), 490–503.

Wiedmer, M., Montgomery, D. R., Gillespie, A. R., & Greenberg, H. (2010). Late Quaternary megafloods from Glacial Lake Atna, Southcentral Alaska, USA. Quaternary Research, 73(3), 413-424.

Wilkinson, C., Harbor, D. J., Helgans, E., & Kuehner, J. P. (2018). Plucking phenomena in nonuniform flow. Geosphere, 14(5), 2157-2170.

Wissink, G. K., Wilkinson, B. H., & Hoke, G. D. (2018). Pairwise sample comparisons and multidimensional scaling of detrital zircon ages with examples from the North American platform, basin, and passive margin settings. Lithosphere, 10(3), 478–491.

Worni, R., Huggel, C., & Stoffel, M. (2013). Glacial lakes in the Indian Himalayas: from an area-wide glacial lake inventory to on-site and modeling based risk assessment of critical glacial lakes. Science of the Total Environment 468: S71–S84.

Xu, J., Snedden, J.W., Stockli, D.F., Fulthorpe, C.S., and Galloway, W.E. (2017). Early Miocene continental-scale sediment supply to the Gulf of Mexico Basin based on detrital zircon analysis: Geological Society of America Bulletin, v. 129, p. 3–22.

Xu, Q., Fan, X. M., Huang, R. Q., & Westen, C. Van. (2009). Landslide dams triggered by the Wenchuan Earthquake, Sichuan Province, south west China. Bulletin of Engineering Geology and the Environment, 68(3), 373–386.

Yang, X., Yang, Z., Cao, S., Gao, X., & Li, S. (2010). Key techniques for the emergency disposal of Quake Lakes. Nat. Hazards 52, 43–56.

Yin, A., Dubey, C.S., Kelty, T.K., Webb, A.A.G., Harrison, T.M., Chou, C.Y., and Célérier, J., (2010b). Geological correlation of the Himalayan orogen and Indian craton: Part 2. Structural geology, geochronology, and tectonic evolution of the eastern Himalaya: Geological Society of America Bulletin, v. 122, p. 360–395.

Yin, A., Dubey, C.S., Webb, A.A.G., Kelty, T.K., Grove, M., Gehrels, G.E., and Burgess, W.P., (2010a). Geological correlation of the Himalayan orogen and Indian craton: Part 1. Structural geology, U-Pb zircon geochronology, and tectonic evolution of the Shillong Plateau and its neighboring regions in NE India: Geological Society of America Bulletin, v. 122, p. 336–359.

Zeitler, P., Meltzer, A., Brown, L., Kidd, W., Lim, C., Enkelmann, E., Hoke, Gregory D. (2014). Tectonics and topographic evolution of Namche Barwa and the easternmost Lhasa Block, Tibet. Special Paper - Geological Society of America, 507, 23-58.

Zhang, J. Y., Yin, A., Liu, W. C., Ding, L., & Xu, X. M. (2016). First geomorphological and sedimentological evidence for the combined tectonic and climate control on Quaternary Yarlung river diversion in the eastern Himalaya. Lithosphere, 8(3), 293-316.

Zhang, J. Y., Yin, A., Liu, W. C., Wu, F. Y., Lin, D., & Grove, M. (2012). Coupled U-Pb dating and Hf isotopic analysis of detrital zircon of modern river sand from the yalu river (Yarlung Tsangpo) drainage system in southern tibet: Constraints on the transport processes and evolution of himalayan rivers. *Bulletin of the Geological Society of America*, *124*(9–10), 1449–1473.

Zhu, P.Y., & Li, T. (2000/2001). Flash flooding caused by landslide dam failure. Newsletter of ICIMOD, Vol. 38, pp. 4–5.

Zhu, P.Y., Wang, C.H., & Wang, Y.C. (2003). Large-scale landslide-debris avalanche in Tibet, China; 2, Formation of an exceptionally serious outburst flood from a landslide dam in Tibet. Landslide News, Vol. 14–15, pp. 23–25.

Zhu, S., Wu, Z. H., Zhao, X. T., Wang, C. M., & Xiao, K. Y. (2013). The age of glacial dammed lakes in the Yarlung Zangbo River Grand Bend during late Quaternary by OSL. Diqiu Xuebao(Acta Geoscientica Sinica), 34(2), 246-250.

Zhu, S., Wu, Z., Zhao, X., Li, J., & Xiao, K. (2014). Ages and genesis of terrace flights in the middle reaches of the Yarlung Zangbo River, Tibetan Plateau, China. Boreas, 43(2), 485-504.

Zin, W. W., Kawasaki, A., Takeuchi, W., San, Z. M. L. T., Htun, K. Z., Aye, T. H., & Win, S. (2018). Flood Hazard Assessment of Bago River Basin, Myanmar. Journal of Disaster Research Vol, 13(1), 15.

APPENDIX A

This appendix contains supporting information for chapter 1: “The geomorphic impact of outburst floods: integrating observations and numerical simulations of the 2000 Yigong flood, eastern Himalaya”. Additional supporting information files (videos, boulderbar.KMZ, output.zip) can be found online: https://agupubs.onlinelibrary.wiley.com/doi/full/10.1029/2018JF004778

Text A1. Field surveys of high-water marks and slackwater deposits

Slackwater deposits identified on the Siang River are typically observed as tabular, well-sorted sandy bodies up to several meters thick draped over preexisting topography along the riverbank between 0 to 35 m above the monsoon flow high-water mark. These deposits are mostly found in hydraulically sheltered areas that are not inundated during annual monsoon flow; for example, we locate deposits on pre-existing river terraces that are above the high-water mark of the annual monsoon such as in Figure C2, which displays slackwater deposit #10 located on a terrace near the Siyom River tributary of the Siang River. The grain size composition (Table C2), sedimentology, and position of the deposits indicate deposition from suspended transport during waning stages of the flood.

The 2000-flood deposits are distinguished from alluvial deposits and the deposits of previous floods by several features. The 2000 flood deposits are composed primarily of horizontally laminated, very fine to medium grained mica-rich sand (Table C2). Several deposits contain laminations or lenses made up of coarser grained sand and pebbles, and deposits often contain occasional scour features and wavy laminations; however, the 2000 flood deposits lack the well-defined cross-bedding or larger sedimentary structures typical of modern fluvial deposits that are observed closer in elevation to the channel.

The 2000 flood deposits are often capped by fresh vegetation growth or recent landslide deposits, but have very little to no soil development, making them easily distinguishable from ancient flood deposits that generally are higher in elevation above the channel and display incipient to well-developed pedogenesis and/or oxidation. At one location visited in 2013 we observed two deposits that we interpret to be from the 2000 (Deposit #8) and the 1900 historical floods respectively; the two tabular deposits are similar in composition, grain size and sedimentary structure, but were observed at distinct elevations and positions on the landscape, with the 1900 flood deposit (~1-2 m lower) being distinguished from 2000 flood sands because of mature tree growth on the deposit including a large jackfruit tree ~40 cm in diameter, which locals suggested represents on the order of 50-70 years of growth in this region (T. Tayeng, personal communication, 2013). Soil development did not appear significantly different for the deposits we interpret as deriving from the 1900 and 2000 flood atthis location. In a handful of other locations, we observed slackwater deposits lacking soil development but having tree and vegetation growth present was not limited to small shrubs and grasses (including banana trees); we interpret those deposits to represent sedimentation from the 1900 flood, and do not include them in our analysis.

Text A2. Shallow-water equations in GeoClaw

GeoClaw is designed to simulate shallow flow over topography using the depth-averaged 2D shallow-water equations:

$$h_t + (hu)_x + (hv)_y = 0, \tag{1}$$
$$(hu)_t + (hu^2 + \frac{1}{2}gh^2)_x + (huv)_y = -ghB_x - Du,$$
$$(hv)_t + (huv)_x + (hv^2 + \frac{1}{2}gh^2)_y = -ghB_y - Dv,$$

Where u(x, y, t) and v(x, y, t) are the depth-averaged velocities in the two horizontal directions, B(x, y, t) is the topography, and $D = D$(h,u,v) is the drag coefficient. The drag term can take on different forms, but for this study we use:

$$D = \frac{gn^2\sqrt{u^2+v^2}}{h^{\frac{5}{3}}}, \tag{2}$$

where n is the Manning coefficient. Wall friction is not accounted for in this formulation of D. Not accounting for wall friction may be expected to overestimate flow velocities along the flood pathway.

Text A3. Calculation of Manning’s roughness coefficient, n, from bed roughness length-scale

We solved for *n* following the method in Larsen and Lamb (2016) by equating the Manning-Strickler relation and Manning equation, and using a bed roughness length-scale of *ks* = 1 m:

$$n = \left(\frac{1}{8.1}\right)\frac{{k_s}^{\frac{1}{6}}}{g^{\frac{1}{2}}} \tag{3}$$

Text A4. Calculations of bed shear stress from GeoClaw

We calculate bed shear stress, τ_b, from flow depth and speed simulated using GeoClaw at locations in the channel over the entire duration of the flow. Bed shear stress is calculated following Larsen and Lamb (2016) as:

$$\tau_b = \rho C_f s^2 \tag{4}$$

where *s* is the average speed calculated with:

$$s = \sqrt{u^2 + v^2} \tag{5}$$

and the friction coefficient, C_f is related to Manning's *n* by:

$$C_f = \frac{gn^2}{h^{1/3}} \tag{6}$$

Text A5. Calculations of estimated peak discharge.

We calculated the predictive peak discharge using (O'Connor and Beebee, 2009):

$$Q = g^{1/2}h^{5/2} \tag{7}$$

where *g* is the acceleration due to gravity and *h* is the dam breach height. The time to peak discharge was calculated using (O'Connor and Beebee, 2009):

$$t_p = \frac{d}{k} \tag{8}$$

where *d* is the dam height and *k* is the dam erosion rate (O'Connor and Beebee, 2009; Walder and O'Connor, 1997).

Text A6. Estimated monsoon discharge at survey A

Monsoon flow velocity at location A was calculated from Manning's equation using the measured cross-sectional area of the flow *A* (1890 m^2), the wetted perimeter *P* (223 m), and *S* approximated from the DEM (0.002). The product of the calculated velocity (4.6 m/s) and cross-sectional area results in an estimated discharge of $Q = 8.7x10^3$ m^3/s. This discharge is ~19% of the simulated peak flood discharge ($4.6x10^3$ m^3/s) at this location. We judge the uncertainty in *S* to be on the order of 0.001 and propagating this error through the calculation produces an uncertainty in *Q* of $4.3x10^3$ m^3/s or 50% of the estimated monsoon discharge. If we consider uncertainty in *S* and in *n* from our range of n=0.02-0.06, the uncertainty in Q increases to $6.2x10^3$ m^3/s, which is 71% of the estimated monsoon discharge.

Text A7. Calculations of incipient motion

The dimensionless critical shear stress for incipient motion was calculated using:

$$\tau_c^* = 0.15S^{0.25} \tag{9}$$

(Lamb et al., 2008a), where *S* is the channel gradient (0.02). The calculated value of τ^*_c (0.056) was used along with the calculated bed shear stress (τ_b) from simulations to solve for the median block size (*D*) that can move:

$$D = \frac{\tau_b}{\tau_c^* g(\rho_s - \rho)} \tag{10}$$

where ρ_s is the density of granite (2700 kg/m^3).

Text A8. Calculations of block plucking by sliding

The dimensionless critical shear stress for block sliding was calculated using:

$$\tau^*{}_{pc} = \frac{\cos\theta[\tan\varphi - \tan\theta] + 2\tau^*{}_w}{\left[1 + \frac{1}{2}C_d\left(\frac{u}{u^*}\right)^2 \frac{P}{L}\right][1 + F_L^* \tan\varphi]} \tag{11}$$

(Lamb et al., 2015), where θ is the bed angle approximated from the DEM (1.1° at location 1 and 2; 0.57° at location 3) at the three sites examined, φ is the bed friction angle (35°), $\tau^*{}_w$ is the dimensionless block sidewall stress (we use 0), C_d is the local drag coefficient (set to 1), P is the block protrusion height, L is the block length, $F^*{}_L$ is the dimensionless hydraulic lift force (we use 0.85), and u/u^* is set to 8.3, using values suggested in Lamb et al. (2015).

The value of $\tau^*{}_{pc}$ was then used to calculate the critical shear stress for block sliding with:

$$\tau_{pc} = \tau^*{}_{pc}(\rho_s - \rho)gD \tag{12}$$

Text A9. Calculations of threshold for suspension of sand

The bed shear stress required to suspend sand grains at the location of deposit #4 was calculated using (Bagnold et al., 1966):

$$\tau_b = \rho(0.8w_s)^2 \tag{13}$$

where w_s is the settling velocity determined using (Ferguson and Church, 2004):

$$w_s = \frac{RgD^2}{C_1 v + (0.75 C_2 RgD^3)^{0.5}} \tag{14}$$

using empirical constants $C_1 = 20$ and $C_2 = 1.1$ for grain shape and roughness, a kinematic viscosity $v = 10^{-6}$ m^2/s (20° C), and R determined from:

$$R = \frac{\rho_s - \rho}{\rho} \tag{15}$$

Text A10. Detailed description of flow direction patterns in the Po River

This supporting text provides a supplemental description of complex flow directions in the location shown in Figure 6(e, f). We observe different patterns of bed shear stress and flow direction at location 2 versus location 3 (Figure 6e, f). At location 2, slope failures are observed on both the southwest and northeast sides of the channel, whereas a km-scale landslide is at location 3 on the northeast bank of the channel (Figure 6a). The simulated flow direction at location 2 is sub-parallel to the channel walls, oscillating toward the northeast and southwest banks within just 15° of the downstream direction measured from the trend of the channel walls (Figure 6e). The simulated flow direciton at location 3 is toward the east into the landslide during the first 4 hours of the flow and the transitions toward the south at about 5 hours after the breach (Figure 6f).

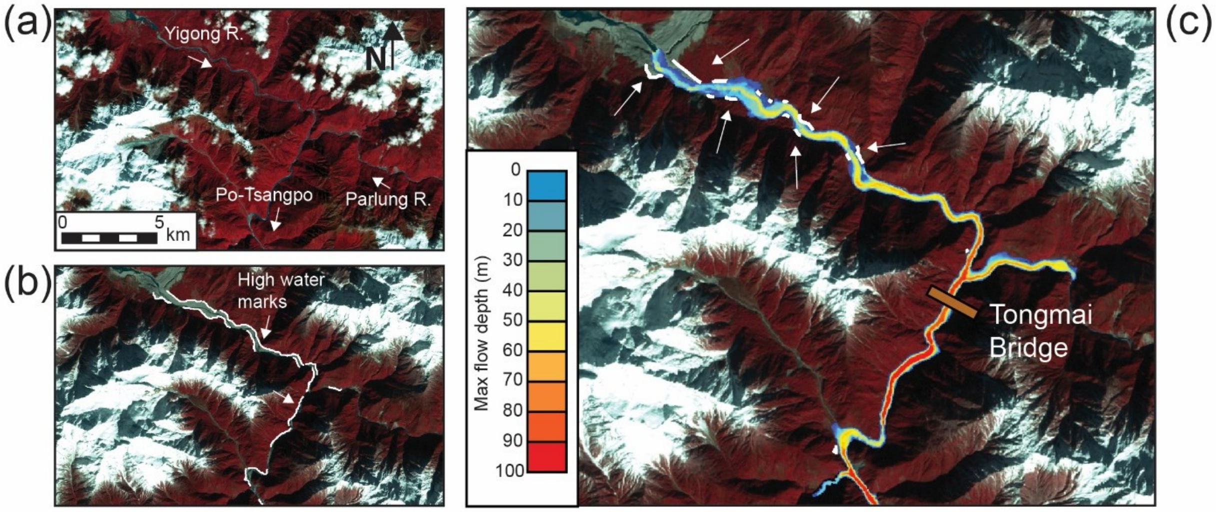

Figure A1. Landsat-7 image from October 1999 in (a) shows the Yigong River prior to landslide impoundment and (b) shows a landsat-7 image from December 2001 with flood trim-lines mapped in white; vegetation appears red in the false color imagery, distinguishing it from bare rock and fresh rock surfaces that have been eroded. The maximum flow depths simulated in GeoClaw (n=0.04, 30 m maximum grid-resolution) are overlain on the December Landsat-7 scene in (c) and white arrows show areas of mismatch; some of the largest depths simulated in the model (~100 m) occur just downstream of Tongmai Bridge above a narrow constriction in the channel before the Tsangpo gorge. Flow depths through time at this location can be seen video 1.

Figure A2. Photo taken in January 2013 showing bedded slackwater flood sand (deposit #10) that is over 2 m in thickness on a terrace of the Siang River near the Siyom tributary. Post-flood landslides had buried several deposits at this location during the years since the event, preserving them from erosion within the valley. This particular deposit had been mined and the sand used for road construction.

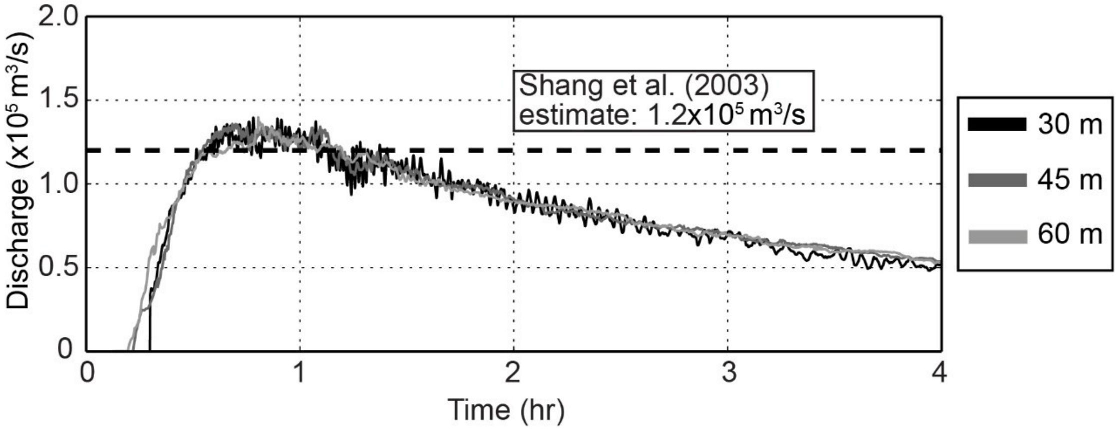

Figure A3. Hydrographs recorded from the first 4 hours of our simulations at Tongmai Bridge varying the maximum grid resolution between 30 and 60 m—the dotted line represents the discharge estimated at this location by Shang et al. (2003), since no hydrograph data are available.

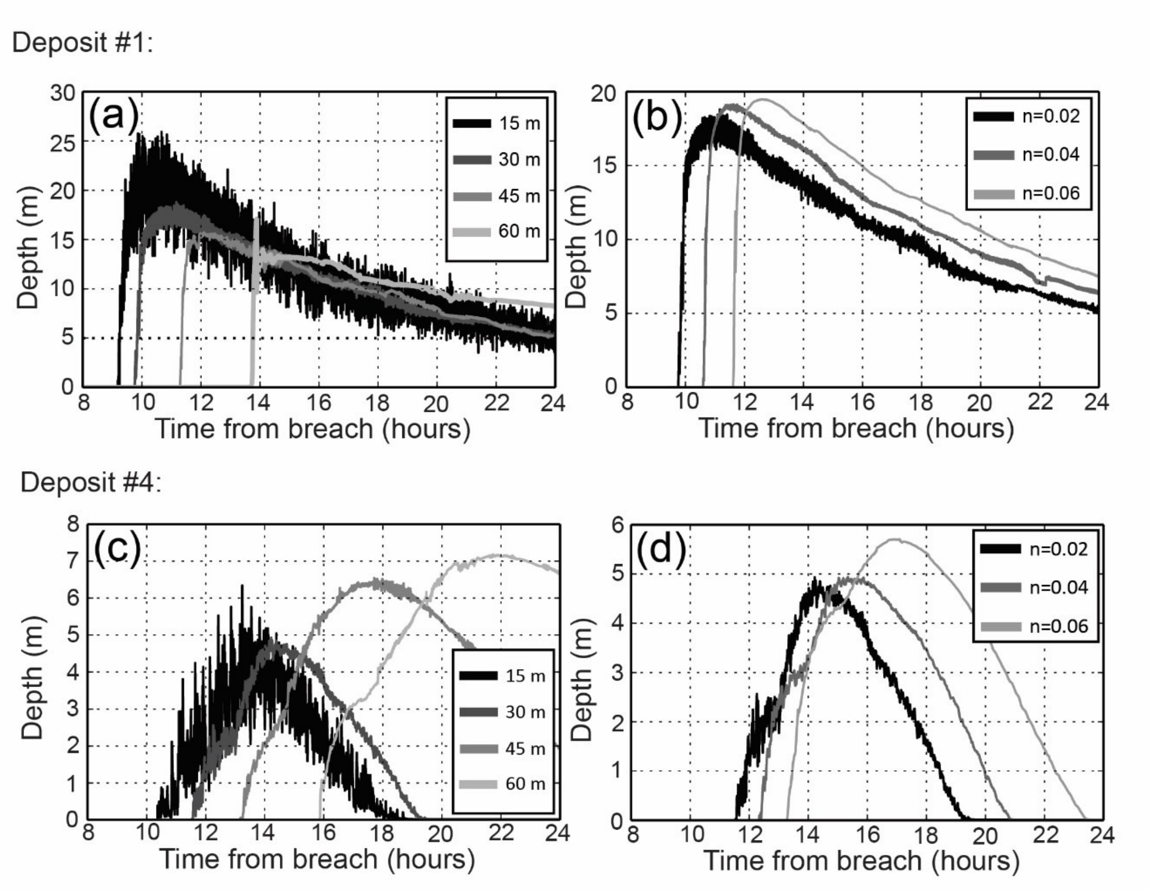

Figure A4. Plot (a) shows simulated depth at the location of deposit #1 from tests of maximum grid resolutions between 15 and 60 m using n=0.02, and plot (b) shows depth at the same location from 30 m simulations in which Manning's *n* is varied from n=0.02 to 0.06. Plot (c) shows the n=0.02 simulation at various grid resolutions further downstream at Deposit #4, and (d) shows depth from 30 m simulations at Deposit #4. The data from n=0.04 simulations at these two locations are located in the output files.

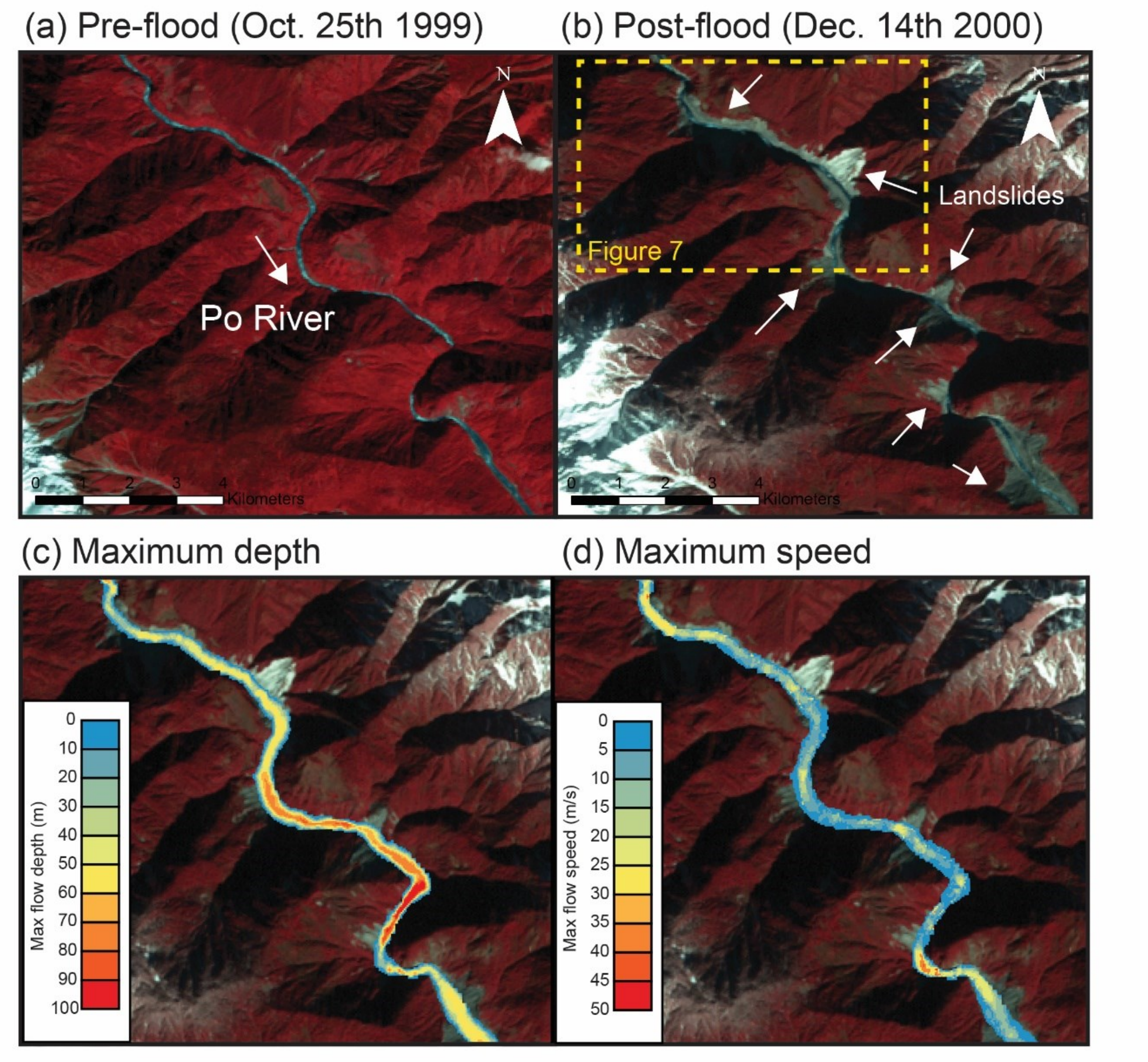

Figure A5. False color landsat-7 scenes from (a) and (b) show the highest gradient segment of the flood pathway (>0.02) where large post-flood landslides occurred. Dotted yellow line in (b) shows the boundaries of Figure 7. Shown in (c) is the maximum flow depth recorded from n=0.04 simulations, which is >100 m in some locations, and (d) shows the maximum flow speeds from n=0.04 simulations that reach up to 56 m/s—the largest flow speeds recorded on the entire flood pathway for this roughness value.

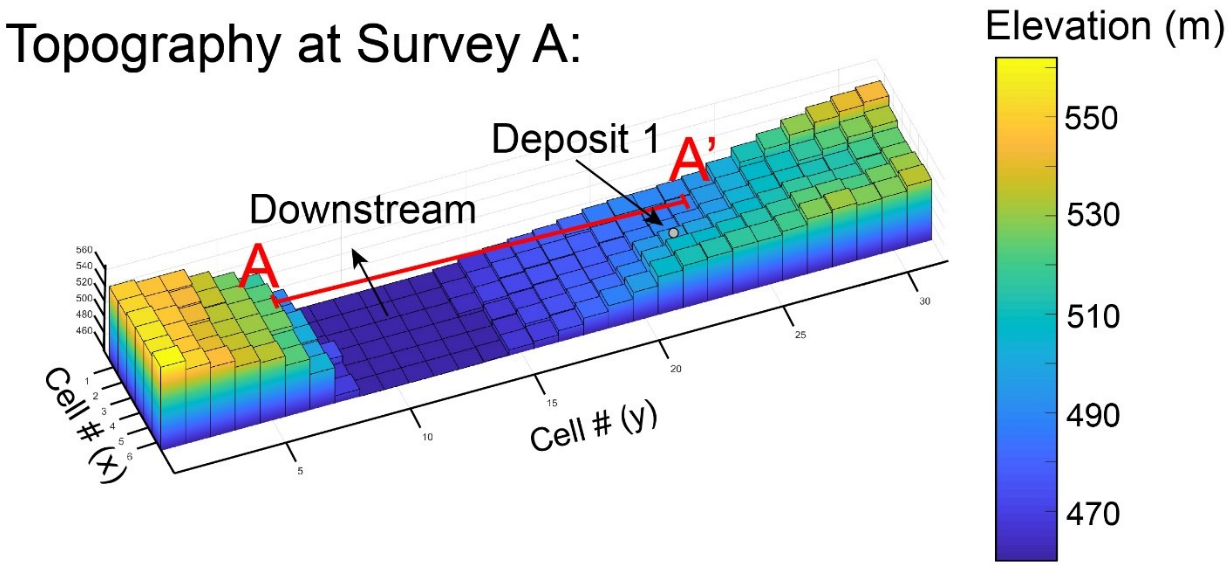

Figure A6. Shown here is a 3D representation of a 6X30 cell area of the SRTM1 DEM at the location of deposit 1 and survey 1 on the Siang River. Each cell in the map is 27 m x 30 m (x and y). The 2D bar graphs shown in Figure 5 were extracted from cells along cross-sections like A-A' along the flood pathway. To make adjustments on GeoClaw stage we summed the cross-sectional area of the channel calculated from the monsoon high-water mark and the cross-sectional area of the simulated maximum depth, and then filled the valley cross-sections with this total area.

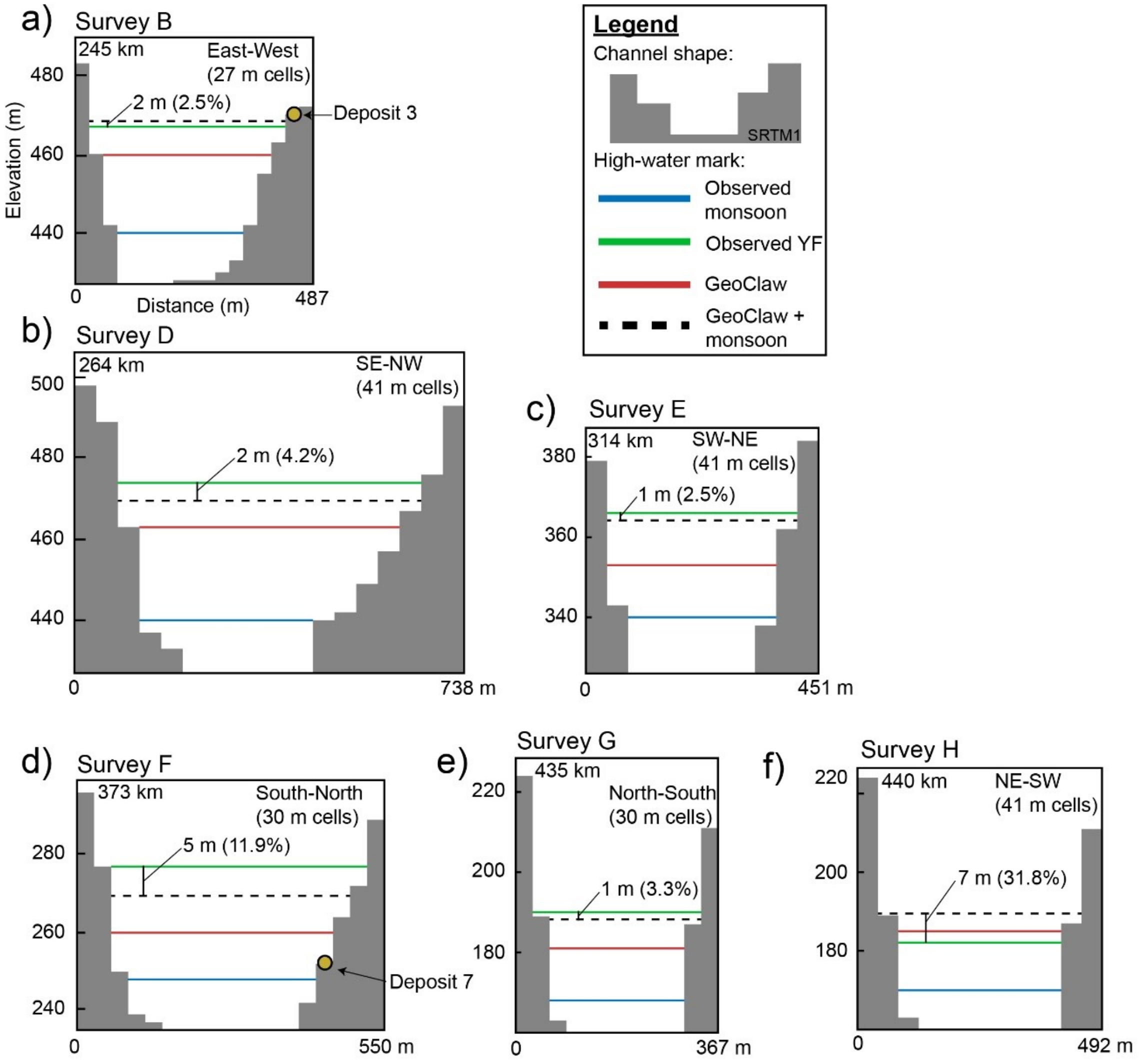

Figure A7. Diagrams (a-f) show simulated stage mapped onto valley topography represented by the SRTM3 DEM in gray at survey locations not shown in Figure 5. Dotted lines represent the adjusted stage, which is the sum of the cross-sectional area of the monsoon plus the cross-sectional area of the simulated flood. All diagrams are oriented downstream and distance plotted below each diagram is measured from left bank to right bank.

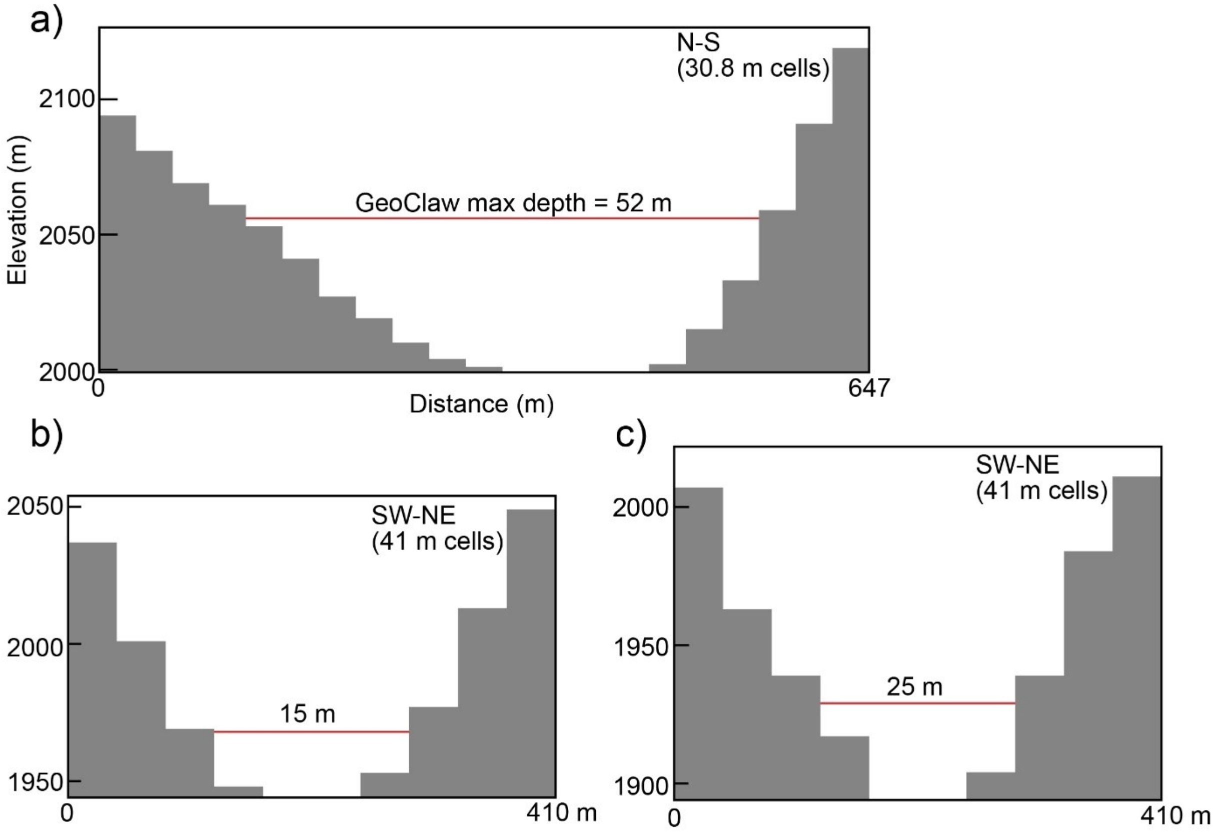

Figure A8. These diagrams show simulated stage mapped onto valley topography represented by the SRTM1 DEM in gray. The diagram in (a) was extracted at the location of the Po River boulder bar in Figure 7 a-d, diagram (b) shows locations 1 analyzed in Figure 6, and (c) shows location 3 from Figure 6.

Figure A9. Meter-scale boulders on the edge of the channel outside of Tuting Village that are sub-rounded and imbricated, indicating they have been transported or reworked in an outburst flood. Similar boulder fields can be seen in Google Earth imagery adjacent to the channel at 28.961°N, 94.865°E.

Survey Location	Nearby Deposit	Distance	Monsoon stage	Flood stage	GeoClaw max depth	Difference in stage	Lon	Lat
		[km]	[m]	[m]	[m]	[m; %]	[DD]	
A	1	238	10.4	40.1	32	8.1 (-22%)	94.91080	29.04867
B	3	245	13.3	39.1	32.2	6.9 (-18%)	94.90578	29.05047
C	4	247	12	48	41.5	6.5 (-14%)	94.90158	28.99481
D	6	264	13.5	47.6	36.1	11.5 (-24%)	94.89917	28.98445
E	-	314	14.1	40.3	27.2	13.1 (-33%)	94.86564	28.96191
F	9	373	13.9	42.1	25.4	16.7 (-40%)	95.06935	28.57659
G	-	435	7.9	30.6	21.1	9.5 (-31%)	95.05757	28.35416
H	-	440	9.5	22.3	24.6	-2.3 (10%)	95.03097	28.17346

Table A1. Survey locations and stage measurements. Corresponding deposits are in Table S2. Distance is measured along the river channel downstream from the dam breach. Monsoon and flood stage are the maximum observed stage heights measured above the river level at the time of the survey. GeoClaw max depth is the maximum simulated depth at the location. Difference in stage is shown as the difference between observed flood stage and the simulated stage in both meters and as a percentage.

						Location		Grain size		
Deposit #	Nearby Survey	Distance	Elevation	Observed height	GeoClaw max depth	Lon	Lat	D10	D50	D90
		[km]	[m]	[m]	[m]	[DD]		[mm]		
1	A	238	465	-	17.7	94.91080	29.04867	0.076	0.167	0.36
2	-	239	492	31	-	94.90578	29.05047	0.09	0.199	0.38
3	B	246	471	41	0.1	94.90158	28.99481	0.069	0.135	0.305
4	C	247	464	48	3.8	94.89917	28.98445	0.118	0.304	0.604
5	-	252	456	-	12	94.86564	28.96191	0.151	0.355	0.724
6	D	264	427	-	37.1	94.77323	28.90819	0.095	0.211	0.376
7	-	344	290	21.5	0.3	95.06935	28.57659	-	-	-
8	-	367	308	-	-	95.07956	28.40177	-	-	-
9	F	373	255	30.7	3	95.05757	28.35416	-	-	-
10	-	401	241	21.4	-	94.99652	28.23502	-	-	-
11	-	410	211	30	4.7	95.03097	28.17346	0.067	0.115	0.187
12	-	422	203	-	3.7	95.14255	28.13363	0.068	0.126	0.249

Table A2. Flood slackwater sand deposit locations and grain size data. Deposit numbers are the same as the numbering in figure 2. Distance is measured along the river channel downstream from the dam breach. Elevation from DEM is measured above sea level on WGS 1984 datum. Observed height is the surveyed height of the deposit above the river measured at low flow in the field. GeoClaw max depth is the maximum simulated depth at the location.

Time steps:	Solver:	Boundary conditions:
clawdata.dt_variable = True	clawdata.order = 2	clawdata.num_ghost = 2
clawdata.dt_initial = 0.016	clawdata.dimensional_split = 'unsplit'	clawdata.bc_lower[0] = 'extrap'
clawdata.dt_max = 1e+99	clawdata.transverse_waves = 2	clawdata.bc_upper[0] = 'extrap'
clawdata.cfl_desired = 0.7	clawdata.num_waves = 3	clawdata.bc_lower[1] = 'extrap'
clawdata.cfl_max = 1.0	clawdata.limiter = ['mc', 'mc', 'mc']	clawdata.bc_upper[1] = 'extrap'
clawdata.steps_max = 5e+7	clawdata.use_fwaves = True	
	clawdata.source_split = 'godunov'	

AMR Parameters:	Other Parameters:
amrdata = rundata.amrdata	geo_data.gravity = 9.81
amrdata.amr_levels_max = 5	geo_data.coordinate_system = 2
amrdata.refinement_ratios_x = [4,2,2,2]	geo_data.earth_radius = 6367.5e3
amrdata.refinement_ratios_y = [4,2,2,2]	geo_data.coriolis_forcing = False
amrdata.refinement_ratios_t = [4,2,2,2]	geo_data.sea_level = 0.0
amrdata.aux_type = ['center','capacity','yleft','center']	geo_data.dry_tolerance = 1.e-3
amrdata.flag_richardson = False	geo_data.friction_forcing = True
amrdata.flag2refine = True	geo_data.manning_coefficient = 0.04
amrdata.regrid_interval = 3	geo_data.friction_depth = 1000.0
amrdata.regrid_buffer_width = 3	refinement_data = rundata.refinement_data
amrdata.clustering_cutoff = 0.700000	refinement_data.wave_tolerance = 1.e-2
amrdata.verbosity_regrid = 0	refinement_data.deep_depth = 1e2
	refinement_data.max_level_deep = 4
	refinement_data.variable_dt_refinement_ratios = True

Table A3. User input parameters from Setrun.py file

Po River bar (Figure 6a-d)				Siang River bar near Survey A (Figure 6e-f)			
Boulder	Lon	Lat	Length	Boulder	Lon	Lat	Length
	[DD]		[m]		[DD]		[m]
1	95.01936	30.03998	9	1	94.91298	29.04816	4.3
2	95.01896	30.04059	3.4	2	94.91255	29.04810	3.7
3	95.01893	30.04011	5.4	3	94.91269	29.04812	2.3
4	95.01824	30.04064	6.1	4	94.91207	29.04795	3.8
5	95.01826	30.04057	5	5	94.91155	29.04779	3.3
6	95.01806	30.04037	10	6	94.91134	29.04768	3.7
7	95.01828	30.04009	7	7	94.91144	29.04765	2.7
8	95.01796	30.04109	5.3	8	94.91123	29.04757	3.3
9	95.01782	30.04039	5	9	94.91102	29.04758	2.5
10	95.01797	30.04065	5	10	94.91083	29.04754	3.5
11	95.01723	30.04058	6	11	94.91028	29.04755	3.4
12	95.01704	30.04077	6.3	12	94.91029	29.04758	4
13	95.01729	30.04095	5.1	13	94.90958	29.04781	3.3
14	95.01721	30.04041	4.1	14	94.90959	29.04770	3
15	95.01847	30.04033	6	15	94.90951	29.04770	2.5

Table A4. Boulder location and size data. Length is measured as the intermediate axis length of the boulder from Google Earth imagery from October 2000 and December 2014 for the Po River and Survey A respectively

Survey Location	Nearby Deposit	Distance	Max depth n=0.02	Max depth n=0.04	Max depth n=0.06
		[km]	[m]	[m]	[m]
A	1	238	31.2	32.0	32.4
B	3	245	31.5	32.2	32.8
C	4	247	41.2	41.5	42.1
D	6	264	36.5	36.1	36.1
E	-	314	28.0	27.2	26.7
F	9	373	24.5	25.4	26.2
G	-	435	12.6	21.1	28.9
H	-	440	10.7	24.6	33.3

Table A5. Maximum simulated flood depth from *n*=0.02, 0.04 and 0.06 simulations

Location	Distance [km]	Arrival time of flood [hr]			Max depth [m]	Time of max depth [hr]		
		n=0.02	n=0.04	n=0.06	n=0.04	n=0.02	n=0.04	n=0.06
Tongmai Bridge	17	0.2	0.3	0.4	77.5	0.26	0.33	0.4
Po River (Figure 7)	26	0.5	0.6	0.6	52.8	1.3	1.7	2
Po River (Figure 6; location 1)	31	0.7	0.8	0.9	14.8	1.8	1.3	1.9
Po River (Figure 6; location 3)	34	0.8	0.9	1	25.6	1.8	1.9	1.9
Survey A	238	9.9	10.7	11.75	32	11.4	11.6	12.9
Deposit 1	238	9.9	10.5	11.6	17.7	11.5	11.9	12.9
Deposit 2	239	-	-	-	-	-	-	-
Survey B	245	10.2	11.1	12.1	32.2	11.5	11.8	12.9
Deposit 3	246	10.2	11.1	12.1	0.15	15.8	16.1	17.9
Survey C	247	10.3	11.2	12.2	41.5	11.6	16.1	17.6
Deposit 4	247	10.3	11.2	12.2	3.8	14.8	16.7	17.9
Deposit 5	252	10.5	11.6	12.7	12	15	16.3	17.9
Survey D	264	11.1	12.2	13.5	36.1	15.7	16.8	18.5
Deposit 6	264	11.1	12.2	13.5	37.1	15.6	16.7	18.5
Survey E	314	16.1	17.5	19.4	27.2	18.5	20.2	22.1
Deposit 7	344	18	19.8	21.9	0.3	20.8	23.4	25.7
Deposit 8	367	-	-	-	-	-	-	-
Survey F	373	20	22.9	24.5	25.4	23.9	25.6	28.8
Deposit 9	373	20	22.9	24.5	3	24.1	25.6	28.6
Deposit 10	401	-	-	-	-	-	-	-
Deposit 11	410	23.1	25.5	28.5	4.7	27.1	29.8	33.5
Deposit 12	422	23.9	26.5	29.7	3.7	27.6	30.4	34.3
Survey G	435	24.9	27.6	31.1	21.1	27.8	32.9	47.8
Survey H	440	25.3	28.1	31.7	24.6	28.1	33.1	47.9

Table A6. Time of simulated flood wave arrival at all locations. Simulated arrival time and time of max depth for n=0.02-0.06 simulations at all locations analyzed along the flood pathway. Simulated maximum depth for n=0.04 simulations is also shown. The positions of deposits #2, 8, and 10 were not inundated by the simulations. No data was recorded on the Po River for n=0.02 and n=0.06 simulations.

Max Grid-resolution [m]	Manning's n	Number of CPU cores	Total wall time [hours]
30	0.02	48	102.2
30	0.06	48	80.9
45	0.02	48	36.5
60	0.02	48	17.3

Table A7. Runtime for simulations varying grid-resolution and Manning's roughness parameter, *n*.

Landslide	Location Lon [DD]	Lat	Distance from breach [km]	Azimuth of bank [°]	Average deviation of flow direction from bank [°]	Peak bed shear stress [kPa]	Time of peak stress [hr]
1	94.9571	30.1663	2	97	10	4.6	0.03
2	95.0346	30.1296	11	109	31.8	2.3	0.4
3	95.0512	30.1254	12	90	4.6	2.7	0.5
4	95.0137	30.0354	27	169	8.6	2.3	0.7
5	95.0171	30.0283	28	145	17.4	3.8	0.9
6	95.0313	30.0071	31	144	8.2	4.6	1.1
7	95.0371	30.0046	31	102	26.7	1.2	15.1
8	95.0437	30.0037	32	116	12.1	1.0	1.3
9	95.0521	29.9988	33	125	23.2	2.2	1.1
10	95.0579	29.9946	34	136	14.5	0.3	1.0
11	95.0604	29.9904	34	144	18.3	1.5	1.0
12	95.0587	29.9788	36	173	6.2	0.9	1.0
13	95.0687	29.9729	37	96	3.1	3.8	1.1
14	95.0775	29.9717	38	116	8.1	0.6	21.8
15	95.0796	29.9696	38	131	14.2	3.9	1.3
16	95.0825	29.9566	40	227	20.4	0.3	1.2
17	95.0804	29.9529	41	185	29.8	0.2	2.2
18	95.0871	29.9487	42	96	69.3	0.6	4.0
19	95.0892	29.9483	42	116	46.4	4.8	1.4
20	95.0938	29.9429	42	154	7	1.3	1.7
21	95.0971	29.9379	43	146	6.1	1.4	1.4
22	95.1021	29.9312	44	131	9.4	0.8	1.3
23	95.1062	29.9179	46	149	23.7	1.1	1.4
24	95.1325	29.9108	49	173	13.2	1.9	1.6
25	95.1296	29.8921	52	126	37.7	1.9	1.6
26	95.1454	29.8754	57	159	4.6	1.2	1.9
27	95.1471	29.8888	58	354	16.7	2.3	1.9
28	95.1787	29.9013	63	98	5.4	3.8	2.3
29	95.1829	29.8988	64	134	18.9	1.1	2.1
30	95.1921	29.8904	64	121	20	0.5	2.3
31	95.1888	29.8937	65	133	6.3	1.6	2.2
32	95.2179	29.8796	70	108	35.4	3.2	4.1
33	95.2087	29.8596	73	174	18.6	2.7	2.5
34	95.2829	29.8312	85	155	3.3	0.5	2.9
35	95.2887	29.8152	87	166	1.9	1.7	2.9
36	95.3596	29.7087	104	99	6.7	1.5	3.6
37	95.3754	29.5804	124	173	5.8	0.6	4.6

Table A8. Simulated flow direction and shear stress at the locations of mapped landslides. The azimuth of the bank of the river nearest to each location was measured and the average deviation away from this value was calculated over the course of the flood

AMR Level	Total wall time (hours) [hours]	Average no. grids	No. regridding steps	No. cells advanced [x 10^6]
1	0.006	16	1	77.2
2	0.93	64.6	1139	3492.8
3	3.5	143.7	13536	15739.6
4	12.4	311.7	40464	64236.4
5	55.6	705.8	73727	139920.2

Table A9. Total runtime and grid information for *n*=0.04 simulations

Video A1. Simulated depth on the Yigong and Po Rivers during the first ~8 hours of the flood after the breach.

Video A2. Simulated bed shear stress on the Yigong and Po Rivers during the first ~8 hours of the flood after the breach (same location as Video A1).

Video A3. Simulated depth on the Siang River near Tuting Village (~230 km downstream of breach) from 8 to 30 hours after the breach (same location as Figure 4)

Video A4. Simulated bed shear stress on the Siang River near Tuting Village (~230 km downstream of breach) from 8 to 30 hours after the breach (same location as Video S3; Figure 4).

Video A5. Simulated depth at the Po River boulder bar (Figure 7a-d) from ~0.4 to 4 hours.

Video A6. Simulated bed shear stress at the Po River boulder bar (Figure 7a-d) from ~0.4 to 4 hours (same location as Video A5).

Video A7. Simulated bed shear stress near Survey A (Figure 7e-h) from 8 to 30 hours after the breach.

Video A8. Froude number calculated near Survey A (Figure 7e-h) from 8 to 30 hours after the breach (same location as Video A8).

BoulderBar.kmz. KMZ file with locations of boulder bars observed remotely from Google Earth.

Output.zip. This zipped directory contains various formats of model output from the n=0.04 simulations discussed in the paper including snapshots of GeoClaw output (depth, stress, Froude number) at 30 minute intervals, GeoClaw data recorded at location of deposit #1 and 4 (Figure S4) and locations 1-3 (Figure 6), georeferenced raster datasets showing maximum recorded depth and speed along the flood pathway, and plots of flow direction recorded at the location of mapped landslides.

APPENDIX B

This appendix contains supporting information for chapter 2: "Provenance and erosional impact of Quaternary megafloods through the Yarlung-Tsangpo Gorge from zircon U-Pb geochronology of flood deposits, Eastern Himalaya".

Data from all zircon U-Pb analyses are in Table B1 and online in the GitHub repository: **https://github.com/zewski14/TurzewskiThesisData**

Figure B1. Close up photograph showing fluvial deposit from the modern Siang River with cross-bedding.

Figure B2. Photographs of slackwater deposits from 1900 Yigong River outburst flood. Deposit is located underneath a vegetated surface with a jackfruit tree growing on it (Left), and is composed of laminated, fine to medium grained sand (Right).

Figure B3. Photograph showing location of sample 13SI02 in a slackwater deposit on the Siang River.

Figure B4. Photograph of deposit showing location of sample 13SI40

Figure B5. Deposit showing the location of sample 13SI21.

Figure B6. Photograph of deposits showing location of sample 13SI11.

Figure B7. Photograph taken from the eastern bank of the Siang River showing terraces containing slackwater megaflood deposits at Nubo Bridge.

Figure B8. Photograph showing location of sample 13SI34

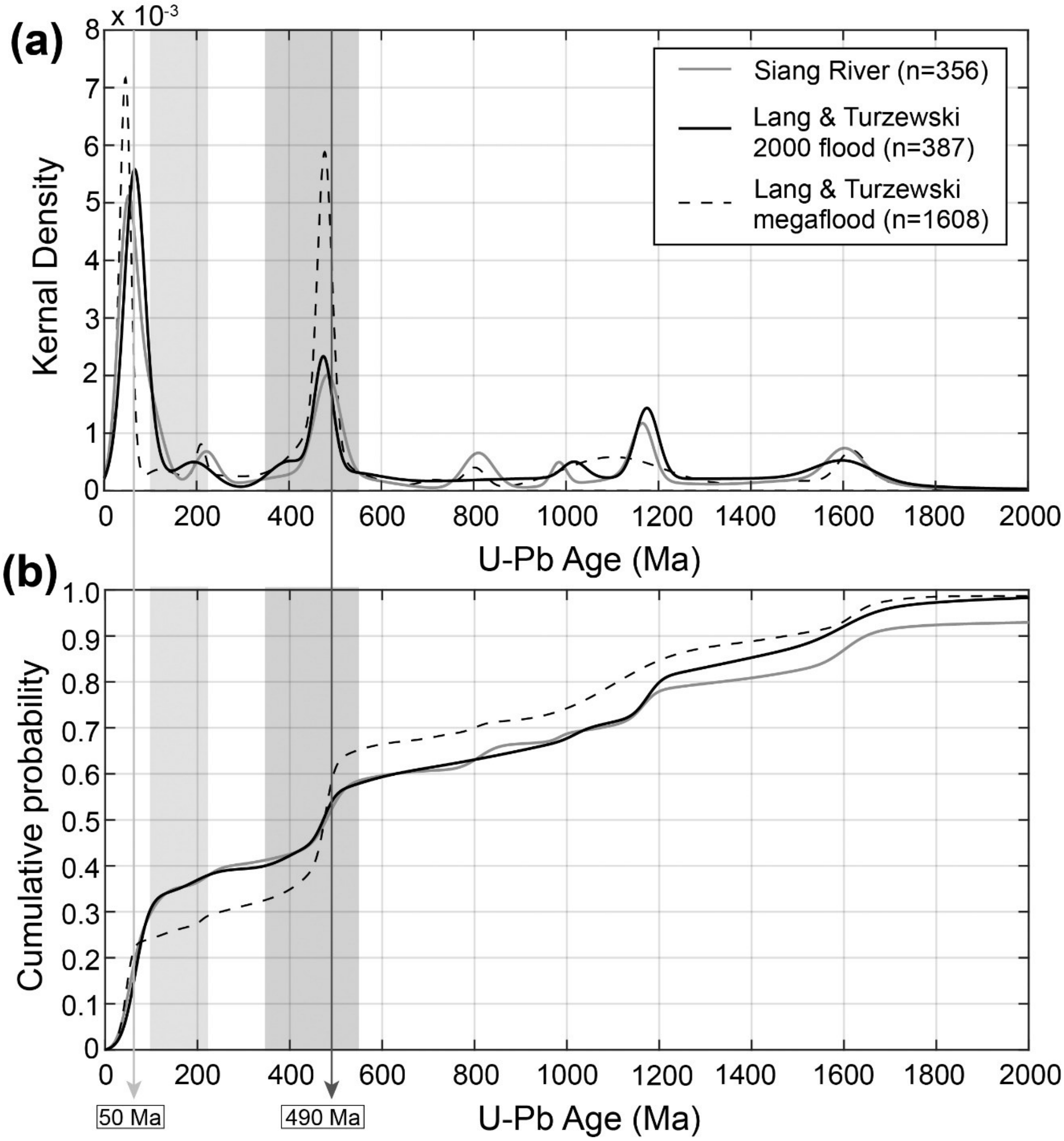

Figure B9. Plot of KDEs showing the previous modern river sample compilation (Stewart et al., 2008; Lang et al., 2013, the updated 2000 Yigong outburst flood compilation (Lang et al., 2013; this study), and the updated megaflood compilation (Lang et al., 2013; this study).

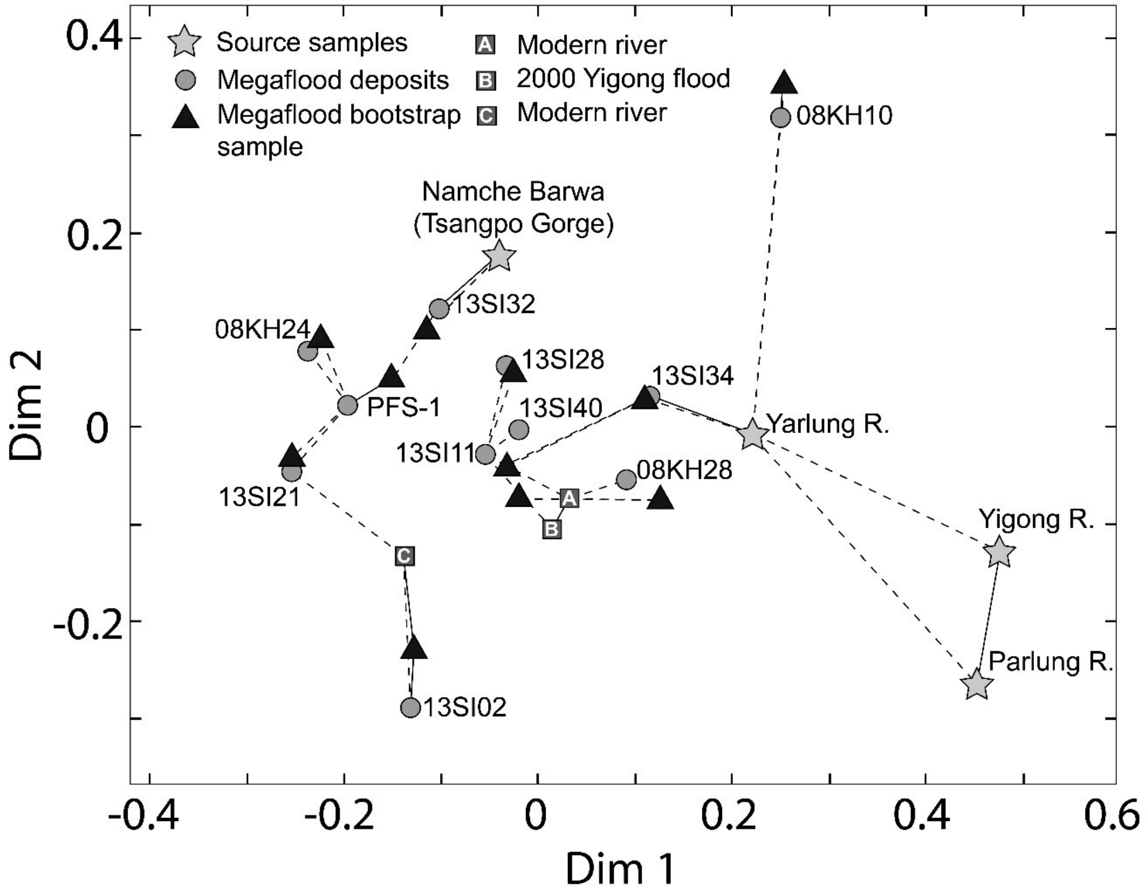

Figure B10. MDS map with source samples, modern river (A) and 2000 Yigong flood compilations (B), the 1900 Yigong flood sample (C), all individual megaflood deposits, and synthetic megaflood deposit samples from bootstrap procedure to remove 20% of grains from the compilation randomly (black triangles). A connection between the bootstrapped PFS-1 sample and the bootstrapped 13SI32 sample can be seen that is not present in the original MDS map.

APPENDIX C

This appendix contains supporting information for chapter 3: “Radiocarbon and single-grain luminescence dating of megaflood slackwater deposits in the Siang River valley, Eastern Himalaya”.

Data from all single-grain IRSL analyses are in Table C1 and online in the GitHub repository: **https://github.com/zewski14/TurzewskiThesisData**

Text C1. Determination of dose rate (D_e) and equivalent dose (D_r),

Dose rate was determined by alpha and beta counting, and by atomic emission for K. Dose rate samples from the deposit were crushed in a mill into a fine powder. For alpha counting, the material was sealed into plexiglass containers with ZnS:Ag scintillation screens. Separation of alpha counts from the U and Th decay series used the pairs technique (Aitken 1985). For beta counting, about 0.5 g of the crushed sample was placed into plastic sample holders and counted for 24 hours by a Risø low level beta GM multicounter system. The average of these four measurements was converted to dose rate (Bøtter-Jensen and Mejdahl, 1988). The beta dose rate measured directly from beta counting is compared to the beta dose rate calculated from alpha counting and atomic emission. This provides a check against measurement error and also possible disequilibrium in the decay chains. Atomic emission measurements were analyzed with a Jenway flame photometer after dissolving samples in acids including HF. Concentrations of K were determined by bracketing the measurements with known standards, and then converted to ^{40}K by natural atomic abundance. Cosmic radiation was calculated following Prescott and Hutton (1994). Radioactivity concentrations were converted to dose rates following Guérin et al. (2011).

Under dim orange/red lights, the IRSL sample tube caps were removed and about 2” of sediment was removed from each tube-end and either discarded as potentially light contaminated or used for dose rate measurements. The sediment in the center of the tube was used for luminescence measurements. Part of the sample was also weighed, dried, and weighed again to calculate moisture content. The bulk sediment was treated with HCl and H_2O_2, dried, and then sieved to 180-212 µm. Heavy liquids were used to separate potassium feldspar from other minerals in the sample. Single grains of potassium feldspar were loaded into specially designed disks and measured using Risø TL/OSL DA-20 reader, with an IR single-grain attachment. The grains were stimulated with a 150 mW 830 nm IR laser at 30% power passed through an RG 780 filter. Emissions were collected by the photomultiplier through a blue-filter pack, allowing transmission in the 350-450nm range. IRSL measurements were made at 50°C, and a preheat of 250°C for 1 minute at 5°C/s proceeded each measurement. Exposure for single-grains was for 0.8 s, using the first 0.06 s for analysis and the last 0.15 s for background.

Text C2. Description of the single-aliquot regenerative dose (SAR) protocol

The single-aliquot regenerative dose (SAR) protocol used to determine equivalent dose (Murray and Wintle, 2000; Auclair et al., 2003). This method uses a test dose to monitor and correct sensitivity changes in the individual feldspar grains when they are preheated, irradiated, or stimulated with light. There are several steps followed for each grain using this procedure: 1) Preheating, 2) measurement of natural IRSL signal, *L(1)*, 3) test dose, 4) preheating, 5) measurement of test dose signal *T(1)*, 6) regeneration dose, 7) preheat, 8) measurement of signal from regeneration, *L(i)*, (9), test dose, (10) preheat, 11) measurement of test dose signal, *T(i)*, 12) repeat steps 6-11 for *i* regeneration does. Ratios of the measured L(i)/T(i) are used to construct a growth curve and the equivalent dose is determined using interpolation of L(1)/T(1). A zero regeneration dose and a repeated regeneration does are employed to insure the procedure is working properly. Test doses for the SAR procedure described above were about 5-6 Gy and delivered by a 90Sr beta source providing 0.11 Gy/s, calibrated with quartz irradiated by a gamma source at Battelle Laboratory in Hanford, Washington. The dose delivered to different grains in single-grain disks varied by an order of magnitude from one end of the disk to the other, and this variation was taken into account when determining doses to individual grains. Grains with unsuitable characteristics were removed from the analysis if they (1) produced poor luminescence signals with net natural signals not at least three times above the background standard deviation, (2), didn't produce a signal ratio (recycle ratio) within 20% of identical regeneration doses administered at the beginning and end of the SAR sequence, (3) yielded natural luminescence signals that did not intersect saturating growth curves, or (4) had a signal more than 10% of the natural signal after the grain was zeroed.

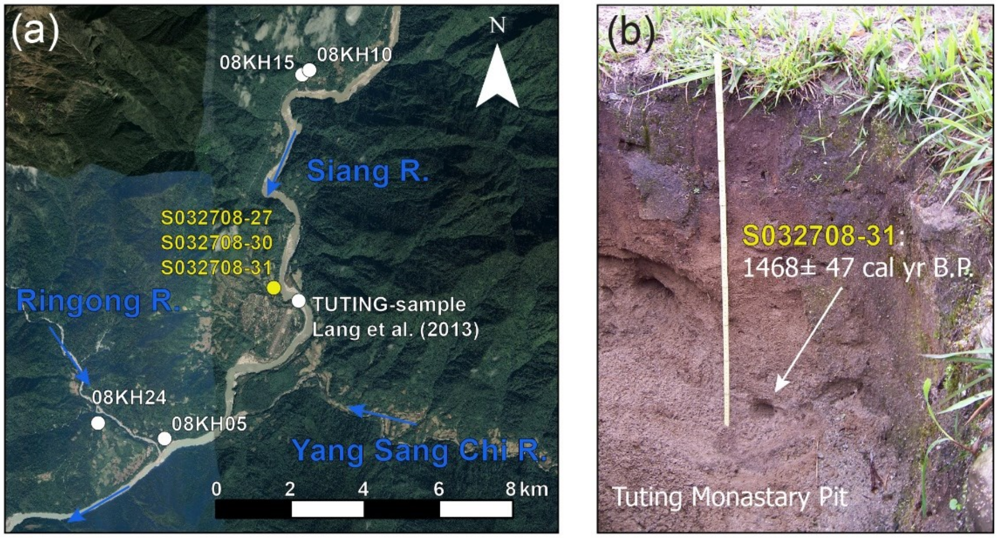

Figure C1. Google Earth image in (a) shows the Siang River at Tuting village with locations of detrital zircon samples from previous studies. Photo in (b) shows the location of the pit where charcoal was obtained from a slackwater megaflood deposit.

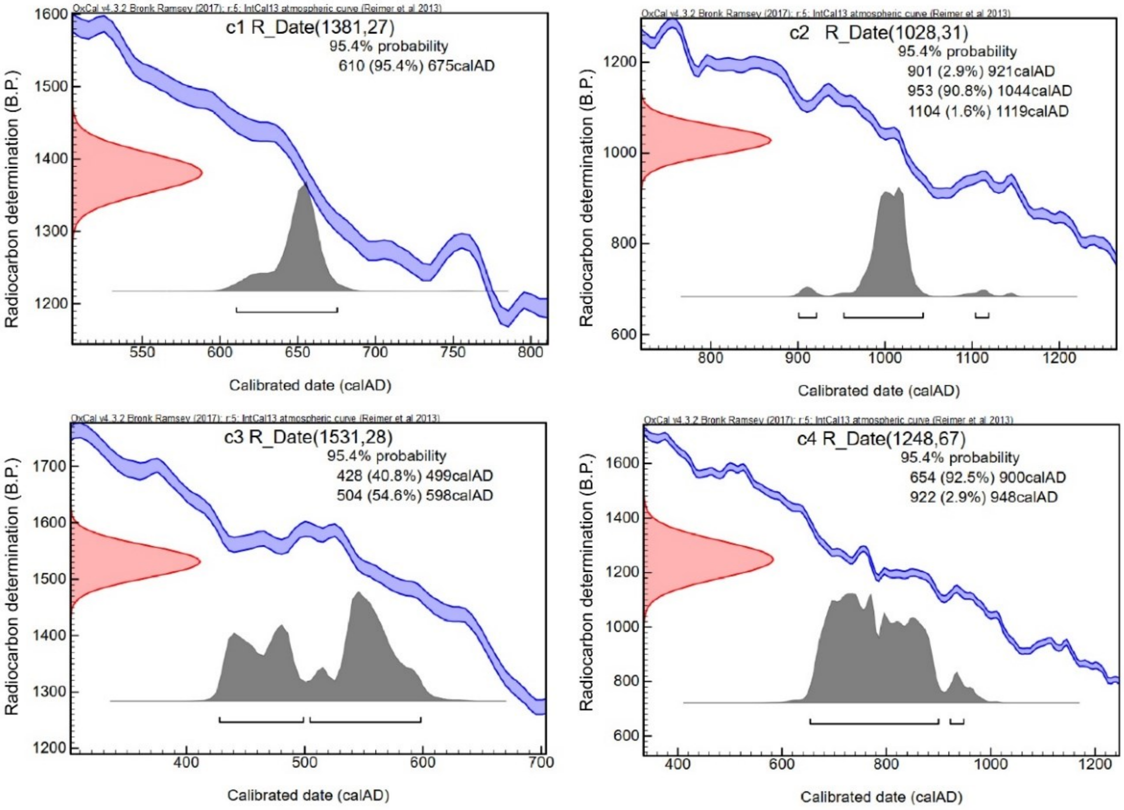

Figure C2. Calibration plots for radiocarbon samples C1 to C4 produced from OxCal 4.3 (Bronk and Ramsey, 2009a) using calibration curves from Reimer et al. (2013).

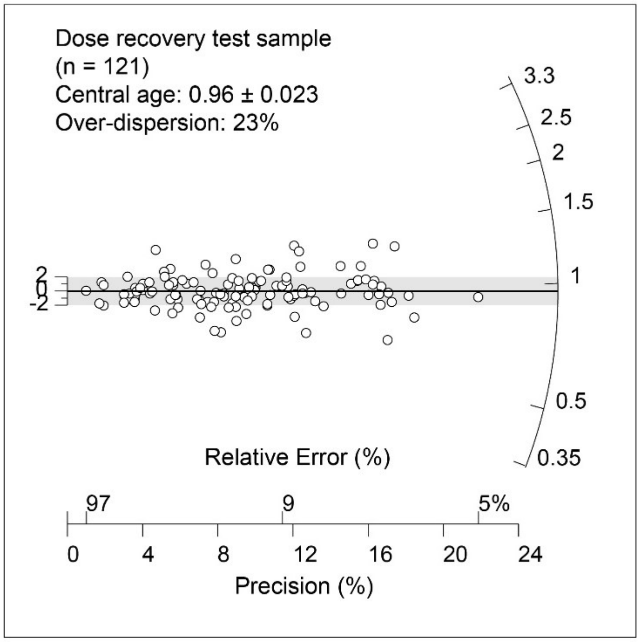

Figure C3. Radial error plot showing results from the dose recovery test on a sub-sample from our dataset (n=121; UW2951, 2962, 2942). The dose recovery was close to 1 indicating a good fit (0.961 +/- 0.023) and dispersion was 23%.

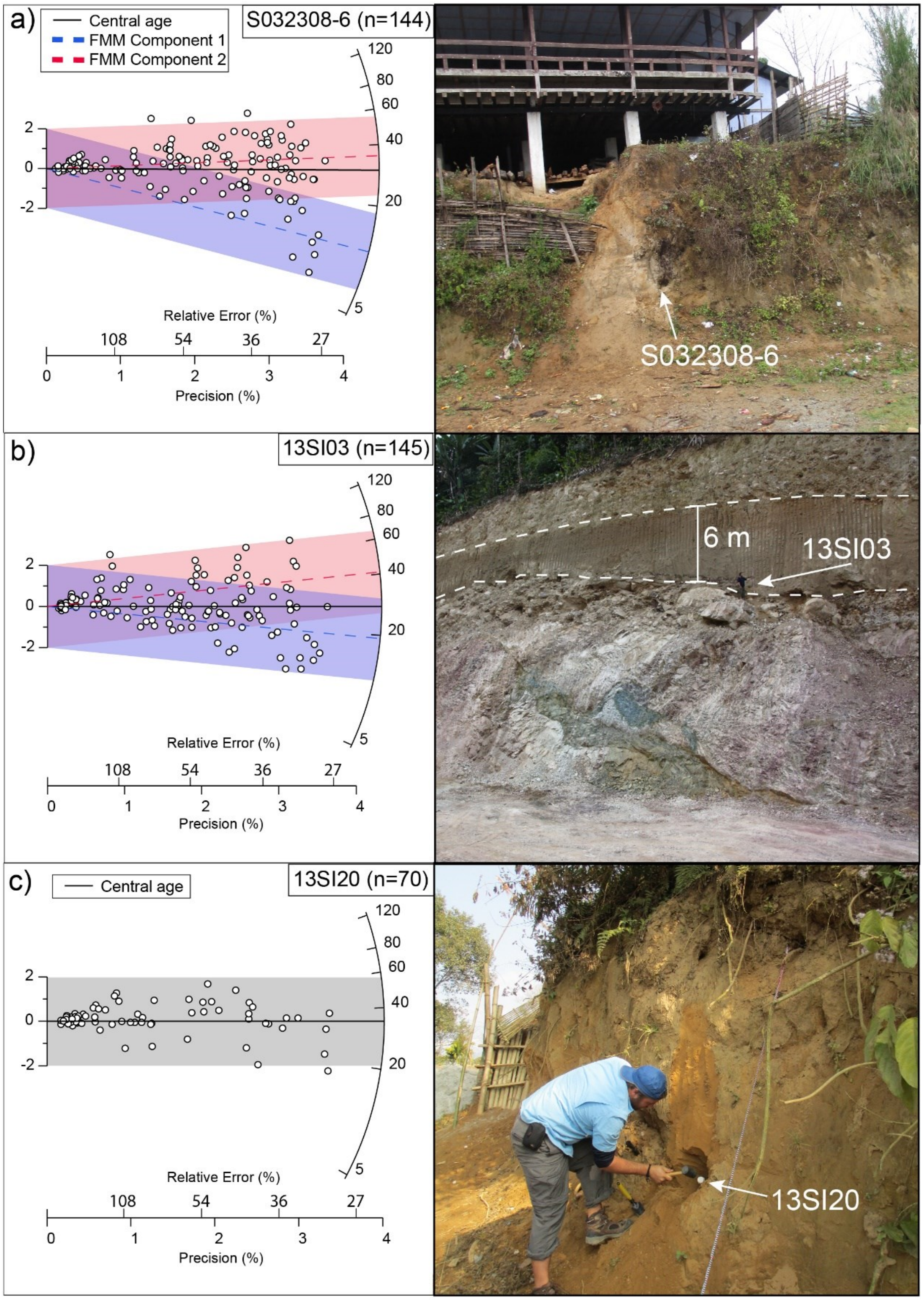

Figure C4. Radial error plots from megaflood deposit samples S032308-6, 13SI03, and 13SI39, that are not nearby other megaflood deposits in vertical sequences.

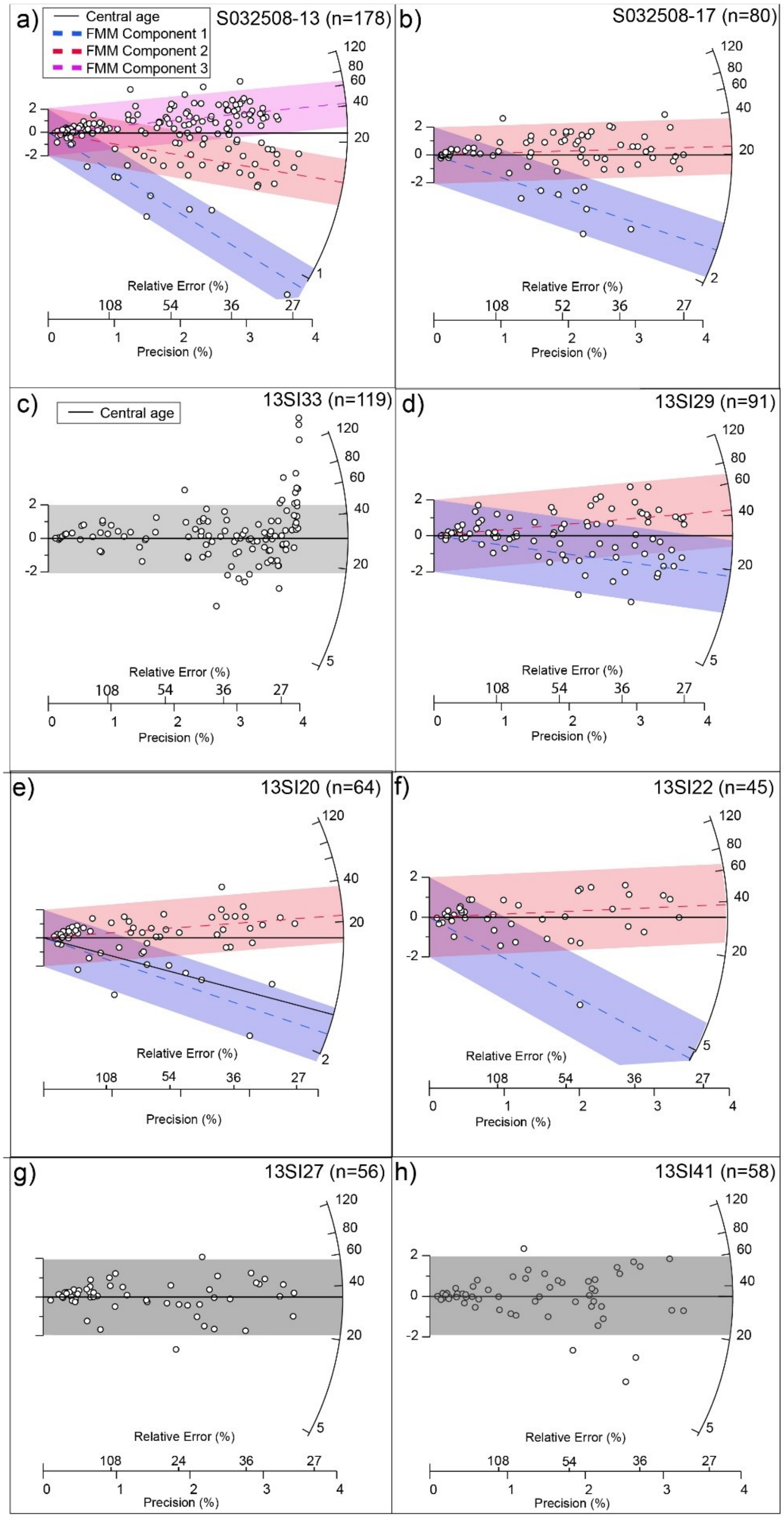

Figure C5. Radial error plots from luminescence dating of various slackwater deposits.

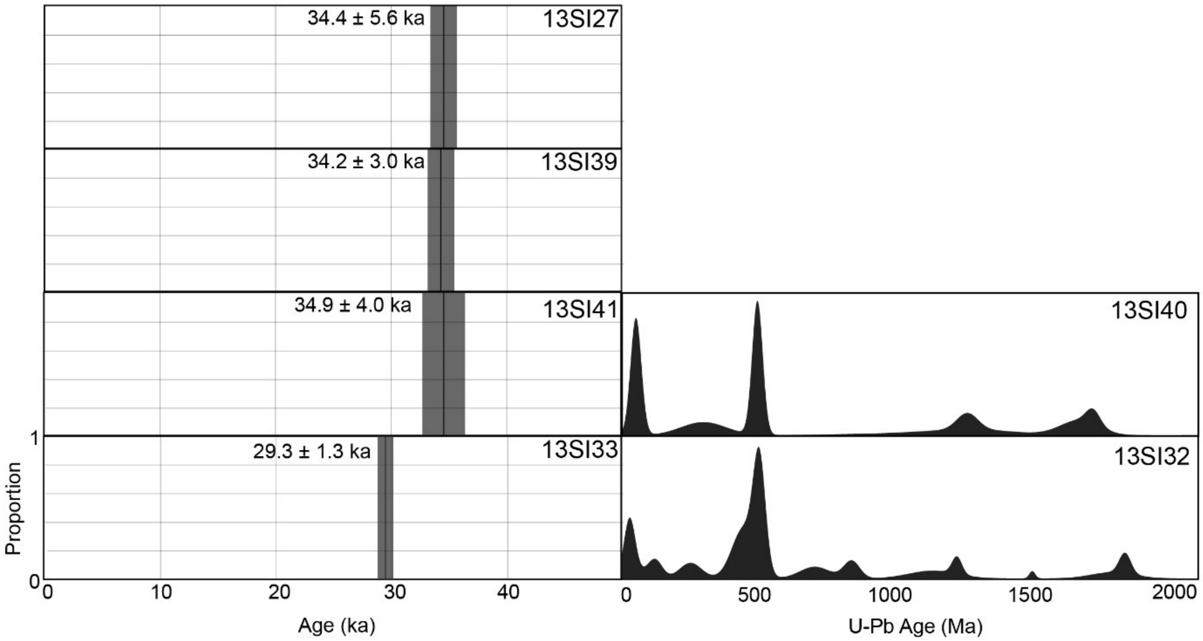

Figure C6. Single-age luminescence samples shown (left) along with samples that have corresponding zircon U-Pb sample.